SCHOOL OF ELECTRICAL AND ELECTRONIC ENGINEERING

Biometric Iris Image Segmentation and Feature Extraction for Iris Recognition

By

Charles Onyebuchi Ukpai

A THESIS

SUBMITTED TO THE FACULTY OF SCIENCE, AGRICULTURE AND ENGINEERING

IN PARTITAL FULFILMENT OF THE REQUIREMENT FOR THE DEGREE

DOCTOR OF PHILOSOPHY

SCHOOL OF ELECTRICAL, ELECTRONIC AND COMPUTER ENGINEERING

NEWCASTLE UNIVERSITY

UNITED KINGDOM

March 2015

NEWCASTLE UNIVERSITY

SCHOOL OF ELECTRICAL, ELECTRONIC AND COMPUTER ENGINEERING

I, *Charles Onyebuchi Ukpai*, confirm that this thesis and the work presented in it are my own achievements.

I have read and understand the penalties associated with plagiarism.

Signature:

Date: March 2015

SUPERVISOR'S CERTIFICATE

This is to certify that the entitled thesis “Biometric Iris Segmentation and Feature Extraction for Iris Recognition" has been prepared under my supervision at the school of Electrical and Electronic Engineering in Newcastle University for the degree of PhD in Computer Engineering – Image Processing/Computer Vision.

Signature:

Supervisor: Professor Satnam Dlay

Date: March 2015

Signature:

Student: Charles Onyebuchi Ukpai

Date: March 2015

ABSTRACT

The continued threat to security in our interconnected world today begs for urgent solution. Iris biometric like many other biometric systems provides an alternative solution to this lingering problem. Although, iris recognition have been extensively studied, it is nevertheless, not a fully solved problem which is the factor inhibiting its implementation in real world situations today. There exists three main problems facing the existing iris recognition systems: 1) lack of robustness of the algorithm to handle non-ideal iris images, 2) slow speed of the algorithm and 3) the applicability to the existing systems in real world situation. In this thesis, six novel approaches were derived and implemented to address these current limitation of existing iris recognition systems.

A novel fast and accurate segmentation approach based on the combination of graph-cut optimization and active contour model is proposed to define the irregular boundaries of the iris in a hierarchical 2-level approach. In the first hierarchy, the approximate boundary of the pupil/iris is estimated using a method based on Hough's transform for the pupil and adapted starburst algorithm for the iris. Subsequently, in the second hierarchy, the final irregular boundary of the pupil/iris is refined and segmented using graph-cut based active contour (GCBAC) model proposed in this work. The segmentation is performed in two levels, whereby the pupil is segmented first before the iris. In order to detect and eliminate noise and reflection artefacts which might introduce errors to the algorithm, a pre-processing technique based on adaptive weighted edge detection and high-pass filtering is used to detect reflections on the high intensity areas of the image while exemplar based image inpainting is used to eliminate the reflections. After the segmentation of the iris boundaries, a post-processing operation based on combination of block classification method and statistical prediction approach is used to detect any super-imposed occluding eyelashes/eyeshadows. The normalization of the iris image is achieved though the rubber sheet model.

In the second stage, an approach based on construction of complex wavelet filters and rotation of the filters to the direction of the principal texture direction is used for the extraction of important iris information while a modified particle swam optimization (PSO) is used to select the most prominent iris features for iris encoding. Classification of the iriscode is performed using adaptive support vector machines (ASVM). Experimental results demonstrate that the proposed approach achieves accuracy of 98.99% and is computationally about 2 times faster than the best existing approach.

DEDICATION

To God Almighty

&

To my wife ***Ngozi*** *and my son Victor Chibuikem*

ACKNOWLEDGEMENTS

I would like to express my profound gratitude and immense thanks to my supervisor Professor Satnam S. Dlay for all his fatherly advice, guidance, support and encouragement throughout the period of this work. I have been highly privileged to know him and work under his supervision and mentorship. I am also deeply grateful to Dr. Wai L. Woo for his guidance and excellent discussions, and positive criticisms of my work which has helped make this research a success. My special thanks goes to Mrs. Gillian Webber for her kindness and administrative support throughout the period of this research.

Above all, I would like to thank my wife Ngozi Charles Ukpai and the entire members of my family and my in-laws for their incredible love, prayers, support and encouragement which have been very instrumental to this academic achievement. I dedicate this thesis to them. I would not conclude without showing my gratitude to the pastors and member of MFM, Newcastle Branch for all their prayers and support and my thanks also goes to Pastor Prof. Patrick Opara and all the members of his family for all their encouragements, prayers and support. Finally, I like to thank Ebonyi State University and Education Task Fund, Nigeria for sponsoring this work.

TABLE OF CONTENTS

LIST OF FIGURES

LIST OF TABLES

ABBREVIATIONS

GCBAC	Graph-Cut Based Active Contour
AC	Active Contour
PCA	Principal Component Analysis
EM	Expectation Maximization
GMM	Gaussian Mixture Model
PR-CWF	Principally Rotated Complex Wavelet Filters
OOI	Object of Interest
DT-CWT	Dual-Tree Complex Wavelet Transform
PSO	Particle Swam Optimization
ROI	Region of Interest
GA	Genetic Algorithm
LS	level Set

LIST OF AWARD AND PUBLICATIONS

Award

Awarded international scholarship from HIPACT, United Kingdom and Nigeria.

Awarded the international research scholarship from Education Task Fund, Nigeria.

Publications

1. C. O. Ukpai, Dlay S.S., Woo W.L.,, "Pupil segmentation using active contour with shape prior," *Proc. SPIE Sixth International Conference on Graphics and Image Processing (ICGIP),* vol. 9443, pp. 2685-2699, 2015.

2. C. O. Ukpai, S. S. Dlay, and W. L. Woo, "Iris feature extraction using principally rotated complex wavelet filters," in *Computer Vision and Image Understanding (ICCVIA), 2015 IEEE International Conference on*, Sousse, Tunisia, (Accepted, in Press).

3. C. O. Ukpai, S. S. Dlay, and W. L. Woo, "Automatic Segmentation of the Iris Boundaries Using Graph Cut Based Active Contour," in *IEEE International Journal on* Systems, Man and Cybernetics, Part B, (submitted).

Chapter 1

1. INTRODUCTION

This chapter presents a brief introduction to iris recognition, the motivation behind this research, the aims and objectives of this research and the contributions made by this research work. Also discussed in this chapter are the structure, strengths and weaknesses, and evaluation methodology of a typical iris recognition system.

1.1 Biometrics

With the ever increasing need for security and personal authentication, and the new dimensions in security challenges facing the world today, the need for a reliable and secure authentication system is highly imperative. Biometric authentication systems have become quite popular due to their ability to authenticate individuals by their unique personal measureable characteristics which is more difficult to manipulate or forge [1-14]. The incessant hacking into organizational and personal systems and the rampant identity theft experienced in the world today is an evidence that the traditional authentication systems based on key codes, passwords and tokens are obsolete and cannot be relied upon in today's technologically advanced world. Iris biometrics which is relatively a new biometric technology compared to other biometric technologies has become quite popular to researchers and scientist in the field of computer vision and pattern recognition due to some major factors: 1) The iris is an internal organ of the body which can be captured noninvasively using a cheap CCD camera [1-24], 2) The iris is adjudged to be one of the most reliable biometric trait in existence today and it is highly unique to the individual that even the iris patterns of both irises of same individual and that of identical twins are completely different [12-19]. These interesting characteristics of the iris have inspired research into the use of iris patterns for person authentication. However, iris recognition involves complex mathematical processes, which sometimes are too slow to be implemented in today's highly demanding and advanced systems. Also, the capture process of most implemented iris recognition systems involves a stop and stare process or head positioning process which is not quite convenient and may amount

to waste of time. Moreover, the environmental setup for the capture of iris images involve the use of near-infrared lightening to illuminate the iris before capture which is also a source of error and demands subject's full co-operation. These are limiting factors for the iris biometric technology. Today, new researches have started to push the boundaries of iris biometrics technology and iris capture on the move and at a distance is becoming prevalent. These new mechanisms of iris capture are now yielding non-ideal iris images which are more challenging to process using the standard iris biometric algorithm. Figure 1.1 shows examples of iris images captured in a non-ideal situation with different types of challenges. The most common challenges of non-ideal iris images include camera noise, reflections and occlusions.

Extracting the iris portion from the captured eye image, or more generally segmentation of iris portion in an eye image is a very important task for any iris recognition system because it defines the portion of the iris image which would be used for the iris recognition. As can be seen from the example iris images in Figure 1.1, this process can be a very challenging task given the heterogeneous nature of the iris images. Also, extraction of the important iris features used for representing the iris sample is also highly challenging due to the richness and complexity of the iris texture. A novel methods for iris achieving these tasks are presented in this work and are evaluated to establish their efficacies.

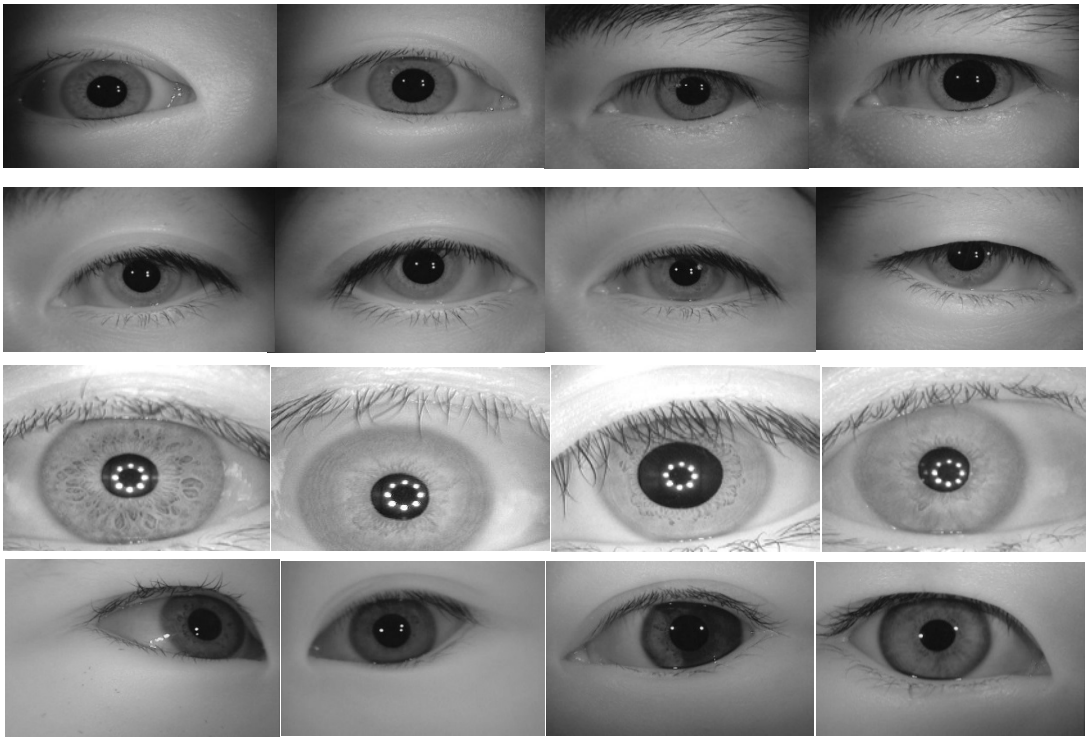

Figure 1.1: Samples of iris images captured under varying environmental conditions and with less subject's co-operation taken from both CASIA and UBIRIS databases.

1.2 Motivation and Challenges

The remarkable uniqueness of iris patterns as well as the ability to capture iris image non-invasively have inspired researchers in biometrics, pattern recognition and computer vision to develop automated system for iris recognition based on 2-D iris images. Although existing iris recognition systems have recorded good performances, the problem of achieving high recognition accuracy in non-ideal iris images at an efficient speed still remains a challenge with no efficient solution yet [44, 45], [47, 48]. The effectiveness and efficiency of iris recognition systems is highly dependent on the accuracy and speed of the iris segmentation module [17]. Therefore, improving the speed and accuracy of the segmentation module will greatly enhance the effectiveness and efficiency of the iris recognition system. In typical non-ideal iris image segmentation, the iris boundaries are either segmented through a costly curve evolution technique based on level-set method [51-56], or using a supervised learning method [44-47]. These two methods are computationally expensive and impacts negatively on the overall speed of the system.

Also, the extraction of important features from the non-ideal iris sample is still a problem that begs for solution. Current methods of iris feature extraction represent the iris sample with high dimensional iris code which impacts negatively on the classification efficiency. Moreover, with lower quality iris images captured under lower of no subject's co-operation being the order of the day, the existing iris feature extraction algorithms mostly leads to many false rejection errors. Hence, representing the iris with smaller iris codes is a problem that have been studied with no efficient solution yet. Most current methods for iris feature extraction and representation have tried to use discrete wavelets to extract iris features [13, 16-18]. This approach is normally affected by shift variance and phase problems which is inherent in discrete wavelet transforms (DWT). A new system needs to be developed to overcome these challenges and create an iris segmentation and feature representation technique that is more efficient and accurate, which is our major motivation in this research. Moreover, our greatest motivation lies in the successes which iris recognition have achieved in various critical application areas including: homeland security, border surveillance and security, web security, national identity management, rapid passenger's information management, controlled access to privileged information, forensic investigation and welfare management to mention but a few. Therefore, the wide area of applicability of iris biometrics implies that this research work will be highly beneficial to many organisation, government and individuals alike.

The main challenges of iris recognition systems are:

I. **Lack of robustness:** The high recognition accuracy recorded by most current iris recognition algorithm in highly constrained imaging condition can be easily depleted when the same algorithm is applied in an unconstrained situation. In strictly constrained imaging situation, where high quality iris image is acquired using a sophisticated imagery setup, it is very easy to achieve an impressive performance with low error rate [19], [20-32]. However, most of the current state-of-the-art iris recognition algorithms fail when implemented in less co-operative iris capture environment, where the probability of capturing low quality iris image is very high. In an uncontrolled imaging environment, iris images are captured using a flexible imagery setup and as such, the images are normally affected by noises like: motion blur, camera diffusion, head rotation, gaze direction, camera angles, reflections, poor contrast, luminosity, occlusions, and pupil dilation [33-58]. These non-idealities drastically reduce the performances of both the iris segmentation and feature representation algorithms considerably, and as such the overall performance of the iris recognition algorithm is degraded.

II. **Non-Circularity of the iris boundaries:** Researchers have found that, the iris and pupil boundaries are of arbitrary shapes [43-45], [47-48]. Therefore, this can lead to segmentation errors, if fitted with some presumed simple shapes like: circles or ellipses. The accurate determination of the boundaries of the iris remains an issue until date.

III. **Speed:** Currently, the time efficiency of available iris recognition systems limits the application of iris biometric in today's highly demanding and fast systems. Iris segmentation is considered the bottle-neck in the iris recognition systems for being the most time consuming module in the system [47], [48].

IV. **Dimensionality:** Also, the millions of interclass and intraclass comparisons that take place during iris recognition is another contributor to time inefficiency in iris biometric systems. There is a clear indication that a system that will meet today's demands will require higher accuracy as well as faster speed. The high dimensionality of IrisCode increases the interclass and intraclass comparison that take place at the classification level thereby impacting negatively on the overall recognition speed. Therefore, there is need to reduce the dimensionality of the IrisCode while maintaining high accuracy at the same time.

In light of these challenges, it is pertinent that a new iris segmentation algorithm with enhanced performance and efficiency is developed to meet today's needs. Also, this research work also looks at reducing the dimensionality of the iris feature vector through a feature selection/optimisation technique. The first phase of this research work focused on developing a robust iris preprocessing (segmentation) algorithm aimed at handling the different challenges of non-ideal iris images captured in less-constrained environment. A model is developed to effectively define the accurate boundaries of the iris with significantly improved speed by combining a local and global boundary optimisation technique. Subsequently, attention is drawn to improving the iris recognition performance by the extraction of the most important iris textural information using a multi-scale, multi-dimensional approach based on complex wavelet filters (CWF) and principal component analysis (PSO). In order to improve on the speed of the recognition system, a method is developed for selecting the most prominent features of the iris for iris representation which reduces the dimensionality of the iris feature vector and improve speed. The accurate classification of iris patterns using adaptive support vector machines (ASVMs) is also able to overcome the problems encountered with fixed thresholding of the iris matching systems.

1.3 Iris Biometrics: An Overview

Iris recognition is, perhaps, the most reliable biometric technique for person authentication which has been successfully deployed in many large-scale biometric based identity management systems where accurate authentication of a person's identity is a critical issue [44], [46-47], [51]. Such large-scale authentication systems include: border control systems, authentication of users wanting access to resources in networked computer environment, boarding of commercial flight, accessing home appliances remotely, gaining access to nuclear facilities, performing bank transactions, etc. [51-52], [53-55]. There are several crucial features of the iris which has made it outstanding as a biometric trait and they include: the uniqueness of iris textures, its non-invasiveness, the stability of iris patterns, public acceptance of iris biometric, and availability of user friendly capturing devices to mention but a few. These promising features have attracted researchers and scientists to this evolving field over the past decade.

The iris is the annular part of the human eye which is located between the dark pupil and the whitish sclera (see Figure 1.3) [59-62]. The iris is made up of many extraordinary

structures that provides many interlacing minutiae characteristics such as freckles, coronas, stripes, crypts, ciliary, collarette, radial and concentric furrows and the pupillary area, which are unique to each individual and to each eye [59]. The iris is an internal organ which is visible externally. The iris uses the constriction and dilation of the sphincter muscles to controls the amount of light that enters the eye through the pupil [44]. The elastic fibrous tissues that makes up the iris structure is very complex and very unique to each eye and individual [44], [47]. The iris pattern is generated by a chaotic process which is highly independent of the individual's genetic structure [47]. The formation of the human iris begins at the early stage of gestation, around the first three months, and the iris structures are completely formed by the eighth month of gestation [47], [48]. Although, the colour and pigmentation of the iris may continue to build throughout the first year of a child's birth [48], the structure of the iris remains stable throughout a person's life time, except for direct physical damage or changes caused through eye surgery. In recent research works, the stability of the human iris for life time have been questioned, but no credible experimental proof have been provided yet to refute the claim that iris structures remains stable for life time [18]. The uniqueness of iris patterns as well as the further advantage that the iris is an internal organ yet visible externally makes it less susceptible to damages over a person's life time. The necessity of the eye as a visual organ will deter many criminals from taking drastic measures to try to change their iris identity through other means. Figures 1.2 and 1.3 shows the eye and iris anatomies, respectively. The iris anatomy is more relevant to the proposed iris recognition methodologies. Thus, we briefly discuss the key visible features, as annotated in Figure 1.3. Therefore, the viability of the iris as a biometric security trait is unquestionable and this research and study of iris biometric is both timely and pertinent for meeting the security challenges facing the digital world today.

1.3.1 Features of the Iris

The iris is made up complex features which is the reason for its uniqueness and reliability. Some of these features are discussed below:

Medial canthus: The angle between the upper and lower eyelids near the centre of the face.

Sclera: The white region of an eye image normally enclosing the iris.

Pupil: The darkest central part of an eye image normally enclosed by the iris.

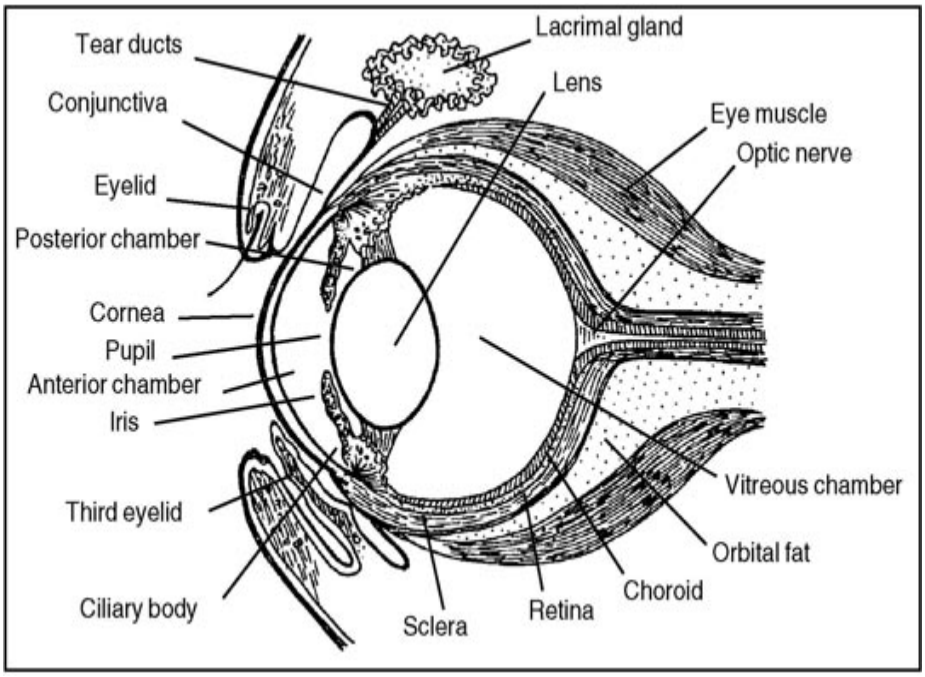

Figure 1.2: The anatomy of the human eye [53].

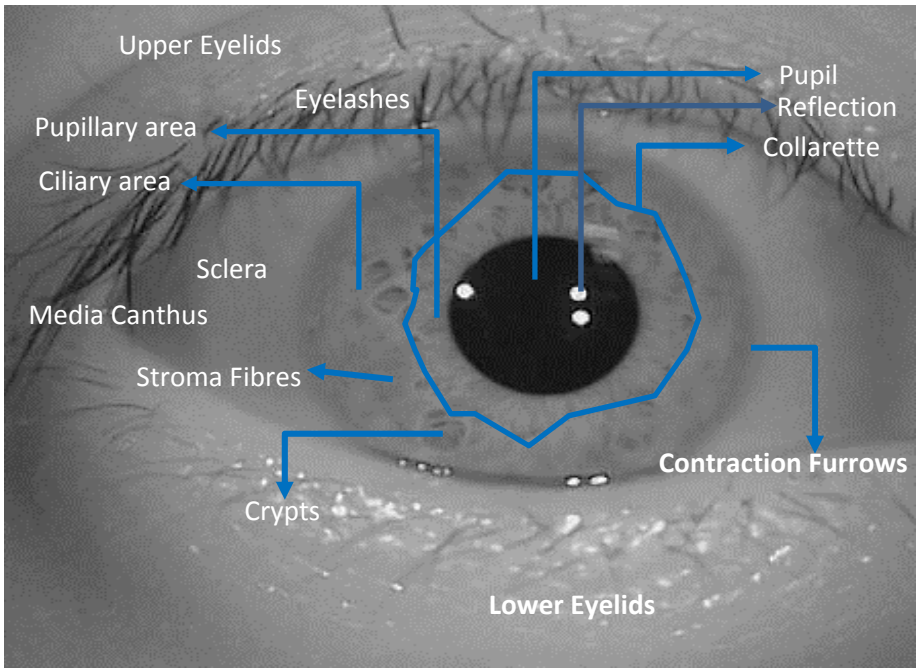

Figure 1.3: The anatomy of the human iris

Pupillary Area: The inner part of the iris whose edges form the contour of the pupil. This is the region of sphincter muscles that enclose the pupil residing in this area.

Ciliary Area: This is the iris region from the pupillary area to the ciliary body. It is the region of dilator muscles that controls the dilation and constriction of the pupil.

Stroma Fibres: The pigmented fibro vascular tissue that constructs most of the visible iris patterns.

Crypts and Furrows: The two types of inconsistencies that are usually found in the distribution of stroma fibres.

Collarette: The region that divides the pupillary area from the ciliary area.

1.3.2 A Typical Iris Recognition System

Figure 1.4a shows the block diagram of a typical iris recognition system which is made up of two building blocks: the iris acquisition block and iris recognition block. The iris recognition block is made up of four different phases including: segmentation, normalization/unwrapping, feature extraction, matching/ classification.

- Iris Image Acquisition Block: Iris image acquisition is the preliminary step of any iris recognition system. It is considered a critical step of the iris recognition system since all the subsequent stages depend highly on the image quality acquired in this step. Most traditional iris recognition systems do not include this step but it is important to have this in mind when designing an iris recognition system. A specially designed camera is used to capture a sequence of iris images. An iris image capturing device considers the following three key factors [19]:

    1) The lighting of the system,

    2) The positioning of the system, and

    3) The physical capture system.

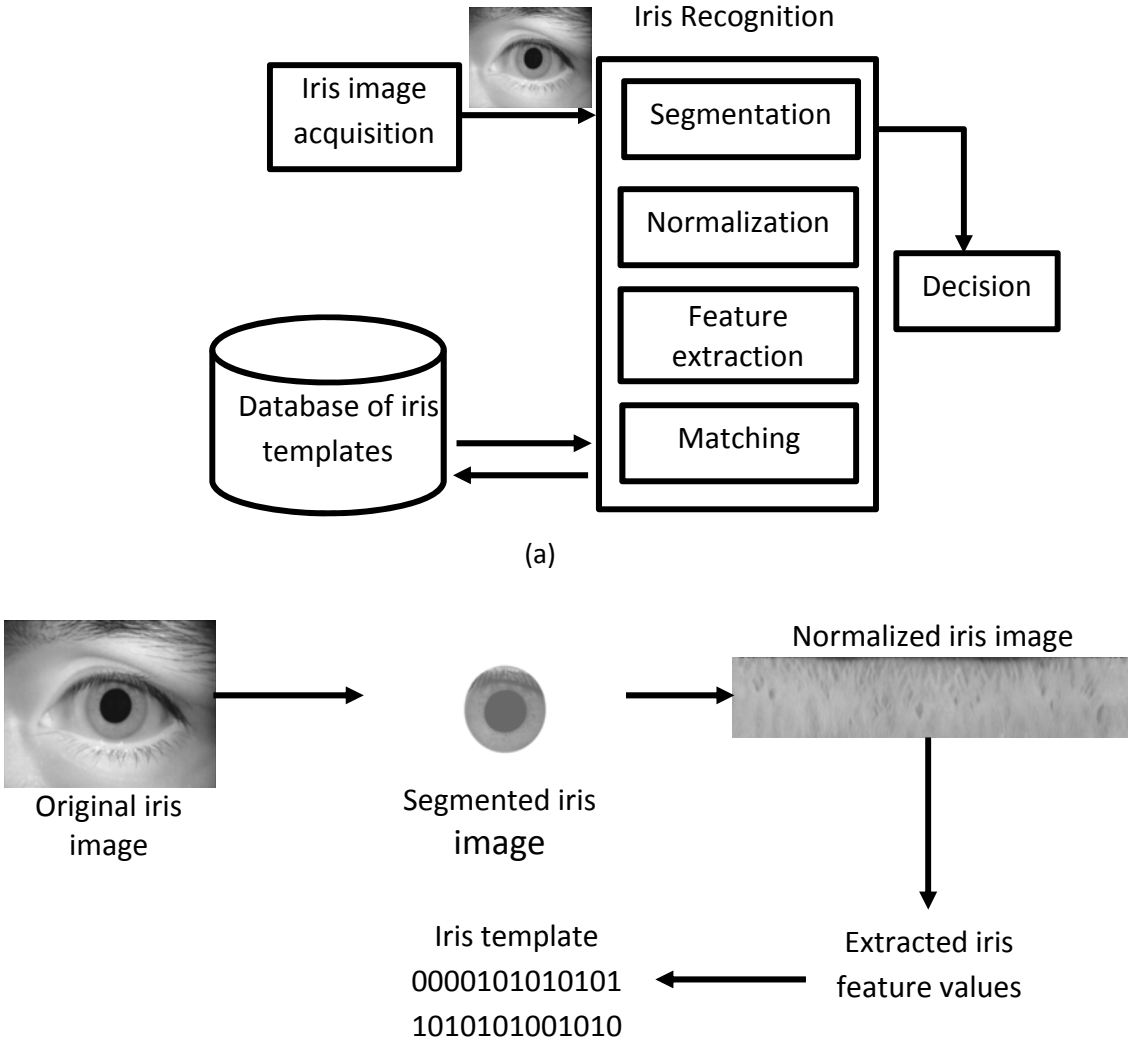

Figure 1.4: An iris recognition system; (a) Steps of a typical iris recognition system, (b) A typical iris recognition system steps in greater details.

- Iris Recognition Block: The effectiveness of the entire iris recognition system is highly dependent on this module. This module is made up of four different phases: segmentation, normalization/unwrapping, feature extraction, and matching/classification. In the first step, the portion of the eye image that belongs to the iris is segmented from the rest of the image. The segmented iris region is unwrapped into a set rectangular block size in order to avoid the size inconsistencies. This is followed by the extraction of the most discriminating features from the unwrapped image and finally, the extracted features are used for matching and classification with stored iris templates in the iris database for individual's authentication.

1.3.3 Strengths and Weaknesses of the Biometric Iris Recognition systems

Among all of the biometric traits, the iris has been considered as the most accurate and reliable biometric trait [42], [44], [51]. However, it has some intrinsic pitfalls that cannot be ignored. The major strengths and weaknesses of the iris as a biometric technique are discussed respectively in the Sections 1.3.3.1 and 1.3.3.2.

1.3.3.1 Strengths of Iris Biometrics

- The iris patterns have small intra-class variability [11], [14].
- The iris is a well-protected internal organ of the eye which contains a high degree of randomness [14], [17].
- The iris is externally visible which makes iris image acquisition possible from a distance [22], [29], [32].
- The iris pattern remains stable throughout the lifetime of a person and it is assumed that each individual has a unique iris pattern [11], [41].
- It is possible to encode the iris pattern and the recognition system's decidability is tractable [42], [44].
- No evidence of genetic influence has been found in the structure of the iris [21]. Therefore, the iris structures in both eyes of the same person are different and those of identical twins are also different [40], [41].
- Iris recognition systems require very low maintenance costs with high interoperability between different hardware vendors. Also, iris recognition technology has the ability to work well with applications from other vendors [1], [18], [32].

1.3.3.2 Weaknesses of Iris Biometrics

- It is difficult to capture the iris image since the size of the iris is very small (its approximate diameter is 1 cm). A specialized camera with an extensive apparatus setup is needed to acquire iris images [9], [14].
- The iris could be partially occluded by lower and upper eyelids, and obscured by eyelashes, reflections, and lenses [19 – 25].
- The size of the pupil changes, non-elastic deformation is a major drawback [8-11], [22].

1.3.4 Iris Recognition System Performance Estimation

The following terminologies are widely used to estimate the performance of an iris recognition system [20-21], [53-56]:

- False Accept (FA): Accepting an imposter as an authorized subject. The probability at which the false accept errors occur is called the False Accept Rate (FAR).

- False Reject (FR): Rejecting an authorized subject incorrectly. The probability at which the false reject errors occur is denoted as the False Reject Rate (FRR).

- True Accept (TA): Accepting a true subject correctly. The probability at which the true accept occur is denoted as the True Accept Rate (TAR).

- True Reject (TR): Rejecting an untrue subject correctly, the probability at which the true reject occurs is called True Reject Rate (TRR).

- Equal Error (EE): When the FA and FR are equal, the error is referred to as Equal Error (ER) and the probability at which FAR=FRR, is called the Equal Error Rate (EER).

Generally, the performance verification of an iris recognition system can be demonstrated by using the Receiver Operator Characteristics (ROC) curve. If the functions *FAR (t)* and *FRR (t)* provide the error rates when the recognition decision is made at a threshold *t*, then the ROC curve is used to plot the error rates against each other [20], where:

$$TAR = \frac{TA}{(TA + FR)} \qquad (1.1)$$

The false accept rate is the number of false accepts divided by the total number of false claims:

$$FAR = \frac{FA}{(FA + TR)} \qquad (1.2)$$

Therefore the false reject rate is

$$FRR = 1 - TAR = \frac{FR}{(TA + FR)} \qquad (1.3)$$

The ROC curve is plotted as:

$$ROC(\tau) = \big(FAR(\tau), FRR(\tau)\big) \qquad (1.4)$$

The FAR and FRR are mapped as a function of τ:

$$ROC(\tau) = \big(FAR(\tau), FRR(\tau)\big) \rightarrow \begin{cases} (1,0) & when\ \tau \rightarrow -\infty \\ (0,1) & when\ \tau \rightarrow \infty \end{cases} \qquad (1.5)$$

which implies that if τ is high, then the FRR is high and the FAR is low and conversely when τ is low, the FAR is high and the FRR is low.

1.4 Non-Ideal Iris Recognition: A New Challenge

Most current iris recognition algorithms that have recorded high recognition accuracy are based on iris images captured with subject's cooperation, within a constrained image capturing build. The performances of those systems greatly diminish in unconstrained capture situation with less or no subject's co-operation where low quality images are captured. Non-ideal iris image refer to iris images captured with less subject's co-operation and varying environmental conditions. Non-ideal iris images captured in unconstrained imaging setup environment mostly suffer from issues like partial occlusion from eyelids, eyelashes, and shadows, reflections from infra-red lightning used in the acquisition process, off angle gaze, motion blur and poor illuminations to mention but a few. Moreover, the inner and outer boundaries of the iris may not maintain any particular shape or size. These challenges mentioned above makes non-ideal iris recognition extremely difficult and tasking.

Other challenges that may face non-ideal iris images include: defocusing, poor contrast, oversaturation, camera diffusion, head rotation, gaze direction, camera angle, pupil dilation, etc. Therefore, the non-ideal conditions contained in iris images can affect iris segmentation and feature extraction performances considerably, and may consequently influence the overall recognition accuracy. Therefore, it is imperative to

design an accurate and robust iris recognition method that can cope with such diverse noise factors and thereby increase the iris recognition accuracy for non-ideal irises.

1.5 Aim and Objectives of the Thesis

The thesis aims to study iris recognition techniques, including the technical background, ideas, concepts and some of the practical issues presently involved in them. The emphasis will be to develop new methods of improving the accuracy as well as time efficiency of existing iris recognition systems. The initial investigation involves several stages relating to the study of segmentation, feature extraction and classification, which focus on improving accuracy and speed. The possible variations in iris recognition techniques are discussed and in accordance, a novel approach utilizing graph cut based active contour model (GCBAC), principally rotated complex wavelet filters (PR-CWF) and particle swam optimization (PSO), and adaptive support vector machine (ASVM) were introduced for iris segmentation, feature selection and classification of the iris, respectively. The thesis attempts to demonstrate that accurate, robust, fast and implementable iris recognition is a viable proposition.

More specifically, the thesis objectives includes the following:

1) To develop an effective reflection detection and removal method which is able to preserve the structure of the unaffected parts of the iris image as much as possible for further processing.
2) To develop a novel boundary segmentation methodology which is robust enough to handle noise and occlusions in non-ideal iris images and able to deal with the shape irregularities of the iris boundaries.
3) To improve the effectiveness and efficiency of the proposed iris segmentation algorithms, through post-processing of the segmented iris image for the detection of any occluding eyelashes and shadows which might still be present after segmentation of the iris.
4) To design and implement a novel iris features extraction and selection approach, which is able to extract and represent the iris sample with reduced dimensionality iris template while maintaining high accuracy and performance.

5) To analyse and evaluate a range of iris recognition systems applied to both ideal and non-ideal iris image, in order to identify the advantages and disadvantages offered by the various approaches.
6) To evaluate the proposed iris recognition system and present the result in a standard format.
7) To identify the limitations of the final proposed iris recognition system and propose a line of further research to investigate these limitations.

1.6 Contributions of the Thesis

Iris recognition has been continually designed and several methods of iris segmentation, feature extraction and matching have been proposed by researchers in recent years. Most iris recognition techniques focus on ideal iris images collected under a stable and constrained imaging conditions and on improving the accuracy of the recognition system only. However, this does not represent real-life implementable solution today. Some existing iris recognition systems have concentrated on improving the accuracy of the iris recognition system for non-ideal iris images, without paying adequate attention to the efficiency and speed of the system.

This thesis presents a novel methodology and pioneered a direction for new research that will enable new developments in the areas of iris segmentation, and feature extraction capable of yielding better performance in identification and verification process. The proposed method is able overcome the limitations associated with conventional (traditional) and current iris recognition approaches in both ideal and non-ideal iris images acquired under varying imaging conditions. The thesis presents six novel contributions in two different stages of iris recognition system representing improvements in iris segmentation, and feature extraction and selection. The contributions of the thesis can be outlined in these areas as follows:

I. Iris segmentation
    a. The methodology for reflections detection and removal developed in this thesis represents a new technique of identifying and locating reflection artefacts in iris images and removing them without altering the image structure in other unaffected parts of the iris. This preserves as much

structure of the image as possible for further processing and enhances segmentation accuracy.

b. A novel methodology for approximating the boundaries of the iris is developed which greatly improved the speed of the segmentation algorithm.
c. A new hierarchical method of localizing both boundaries of the iris based on combination of graph cut optimization (global information) and active contour model (local information) was introduced to overcome the common setbacks of active contour based on level-set method and significantly improve speed and accuracy.
d. The block-based technique for eyelash and shadows detection represents a new adaptive technique for correctly identifying or predicting the eyelash/shadow pixels based on local neighbour information using block classification approach and statistical prediction approach.

II. Iris feature extraction, selection and encoding

a. A new framework for feature extraction based on construction of complex wavelet filters rotated in the directions of the principal texture ensures that invariant features of the iris are extracted.
b. A new step is introduced to eliminate redundant information and for selecting the best features for iris representation. This methodology reduces the feature dimensionality while maintaining highest level of accuracy and performance for the iris recognition system.

1.7 Structure of the Thesis

The thesis presents the work carried out by the author in an effort to achieve the aim and objectives outline in section 1.5. The structure and contents of the thesis is described as follows in a chapter-by-chapter basis.

Chapter 2: Provides a background to the field of biometrics and iris recognition and a short insight into previous works in the field.

Chapter 3: Proposes a new segmentation approach using a combined effort of graph-cut energy optimization and active contour deformation model. The proposed

approach starts by employing an adaptive multiscale edge detection and weighted high-pass filter to identify and isolate reflections in the high intensity areas of the iris image. An adaptive exemplar based image inpainting method is then employed for filling the reflection points in the image. The segmentation of each boundary of the iris is then carried out using a two level hierarchical approach. The approximate boundaries of the iris is first determined using an adaptive starburst algorithm while the proposed graph-cut based active contour (GCBAC) model is used to finally defined the boundaries. Furthermore, a post-processing operation based on block classification and statistical predication method is used for efficient detection of occlusions which might be present in the segmentation iris portion. The outcome of the proposed techniques indicates a fast processing as well as accurate segmentation of iris images even in low quality and highly challenging iris images.

Chapter 4: The aim of this chapter is to extract and select the most important textural features of the iris for the representation of the iris sample. A complex wavelet filter is constructed and rotated in the principal texture direction in order to extract the best iris features. In order to maintain greater orientation selectivity, the filters is also rotated in an opposite direction of the principal texture direction to extract another set of iris features. PSO technique is then applied to select the most important features from the set of features for iris representation. Adaptive Support Vector Machine is used for matching and classification.

Chapter 5: Analyses of the performance of the proposed approaches were conducted using two main datasets that include more than 2000 iris images captured under varying environmental conditions, less subject's co-operation and heterogeneous subject's backgrounds. Also, it presents the performance of the proposed models in comparison with other existing state-of-the-art approaches in other to evaluate performance. To demonstrate the generalization abilities of the proposed approaches, we also tested the algorithm using a database of combined images with over 1000 iris images.

Chapter 7: Discusses and concludes the overall results and contributions of this work. The chapter ends with some pointers and comments to the future work derived from the thesis.

Chapter 2

2. BACKGROUND STUDY AND LITERATURE REVIEW

2.1 Introduction

This chapter presents a background study on some of the techniques employed in this research work as well as a review of some important literatures related to this study. In the background study, a number of key techniques used in this work such as active contour, graph-cut optimisation, discrete wavelet transform (DWT) and complex wavelet transform (CWT) are presented. Also, some benchmark techniques which have been widely implemented in real world situations such as: integro-differential operator and Hough transform techniques are presented and discussed. The literature review summarizes and compares some of the well-known methods used in iris recognition which are at the forefront of this exciting and challenging field. A review of a number of strong techniques used in iris segmentation and feature extraction of iris images are also presented and discussed.

2.2 Iris as a Biometric Trait

The iris is the annular shaped part of the eye between the pupil and the sclera which regulates the amount of light entering the eye through the pupil [1-5]. The iris is physically small in size (about 11mm) but a well-designed optical system is able to magnify the human iris into a high-resolution image that is approximately 200 to 300 pixels in diameter [2], [3], [6-7]. The iris contains many minutia features such as freckles, collarette, stroma, coronas, stripes, furrows and crypts, etc., which make up the iris patterns [4-5]. It should be noted that the visual pattern of the human iris include both colour and texture. However, iris colour have limited discriminating power for person

recognition. So, gray-level iris images captured under near infrared illuminations are often used to record iris patterns for person identification/verification.

The iris texture pattern is formed and becomes stable within the first eight months of the human gestation [6], [8]. It is commonly believed that the formation of iris patterns is determined by the gestation environment, i.e. iris is a phenotypic biometric trait. So even identical twins can be discriminated using suitable iris features; even the iris patterns of the left and right eyes of the same person are different. The first challenge that often faces the automatic recognition of persons by their iris patterns is the determination of the iris portion from the eye image which is called segmentation.

2.3 Iris Segmentation

Iris segmentation plays a pivotal role in the effective person recognition using iris pattern. The iris segmentation module defines the effective part of the eye image belonging to the iris. Some key techniques for defining the region of the eye belonging to the iris are presented and analysed in this section.

2.3.1 Daugman's Integro-Differential Operator

Iris is the annular part of the eye which lies between the pupil and the sclera. Daugman [8-11], in his early work proposed a method of approximating each boundary of the iris as circles. Thus, each boundary of the iris can be estimated based on three parameters which includes: the radius r, and the x_0 and y_0 centre coordinates of the circle. Therefore, Daugman [8] proposed an integro-differential operator which searches through an N parameter space for detection of edges corresponding to the iris boundaries. The integro-differential operator can be given as:

$$\max(r, x_0, y_0) \left| G_\sigma(r) * \frac{\partial}{\partial r} \oint_{r,x_0,y_0} \frac{I(x,y)}{2\pi r}\, ds \right| \qquad (2.1)$$

Where $G_\sigma(r)$ represents the smoothing function and $I\ (x, y)$ represents the image of the eye with (x, y) parameters corresponding to the current pixel location.

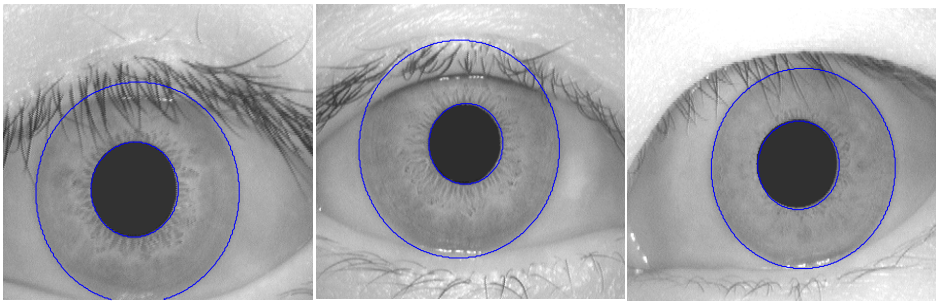

(a)

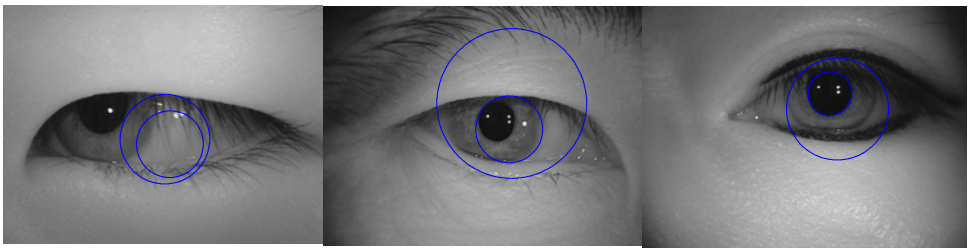

(b)

Figure 2.1: Results of iris boundaries segmentation using Daugman's integro-differential operator on both ideal and non-ideal iris images, (a) the segmentation results on ideal iris images from CASIA v1.0, (b) the segmentation results on non-ideal iris images taken from CASIA v4.0.

Daugman's approach [8-11], and most of the early researches into iris segmentation are based on the simple assumption that iris boundaries are circular. However, recent investigations have shown that the pupillary and limbic boundaries are not perfectly circular [39], [41], [42-57]. Figure 2.1a shows some iris segmentation results based on Daugman's approach on ideal iris image with near circular boundaries while, Figure 2.1b shows some of the segmentation results on non-ideal iris images taken from CASIA v4.0 dataset. It can be clearly seen from Figure 2.1b, that the assumption that iris boundaries are circular can leads to failure of the algorithm in some non-ideal iris images. Also, it can be noted that in some non-ideal iris images, the low contrast between the iris and sclera boundaries can pose a problem for Daugman's edge (intensity change between boundaries) dependent algorithm. Moreover, the possible occlusions from the upper and lower eyelids/eyelashes can lead to false recognition even when the inner and outer boundaries of the iris have been found.

2.3.2 Wildes' Hough Transform

In a similar approach, Wildes [12], proposed a different technical method for estimation of iris boundaries. Wildes proposed the computation of a binary edge maps followed by a Hough transform for the detection of circles in the iris image. It involves two steps. First, a binary edge map is generated by using a Gaussian filter. Then, a Hough transform technique is employed to consider the set of edge points and find the circle that best fits the most edge points. Subsequently, votes are cast in a circular Hough space and analysed to estimate the three parameters of the circle (x_0, y_0, r). The circular Hough space can be defined as

$$H(x_0, y_0, r) = \sum_i h(x_i, y_i, x_0, y_0, r) \qquad (2.2)$$

Where (x_i, y_i) represents an edge pixel and

$$h(x_i, y_i, x_0, y_0, r) = \begin{cases} 1 & if\ (x_i, y_i) is\ on\ the\ circle\ (x_0, y_0, r); \\ 0 & otherwise \end{cases}$$

The location in (x_0, y_0, r) which has the highest value of $H(x_0, y_0, r)$ is chosen as the parameter vector for the strongest circular boundary.

Wildes' approach modelled the eyelids as a parabolic arcs. The estimation of the upper and lower eyelids was achieved using a Hough transform based approach which is similar to the one described above. However, votes are cast for parabolic arcs instead of circles. Figure 2.2 show the process of iris segmentation using Hough transform.

Hough's transform method is generally faster than the integro-differential operator approach and it is able to find circles in the iris image even when parts of the iris is hidden through occlusion. Although the segmentation results in Figure 2.2, shows the effectiveness of the algorithm, its performance can be greatly affected by noise and low contrast between boundaries which is very common in non-ideal iris images. Several challenges have been noted in practical iris segmentation using the traditional approach. For example, most non-ideal iris images suffer from partial occlusion from the eyelids, eyelashes, and shadows.

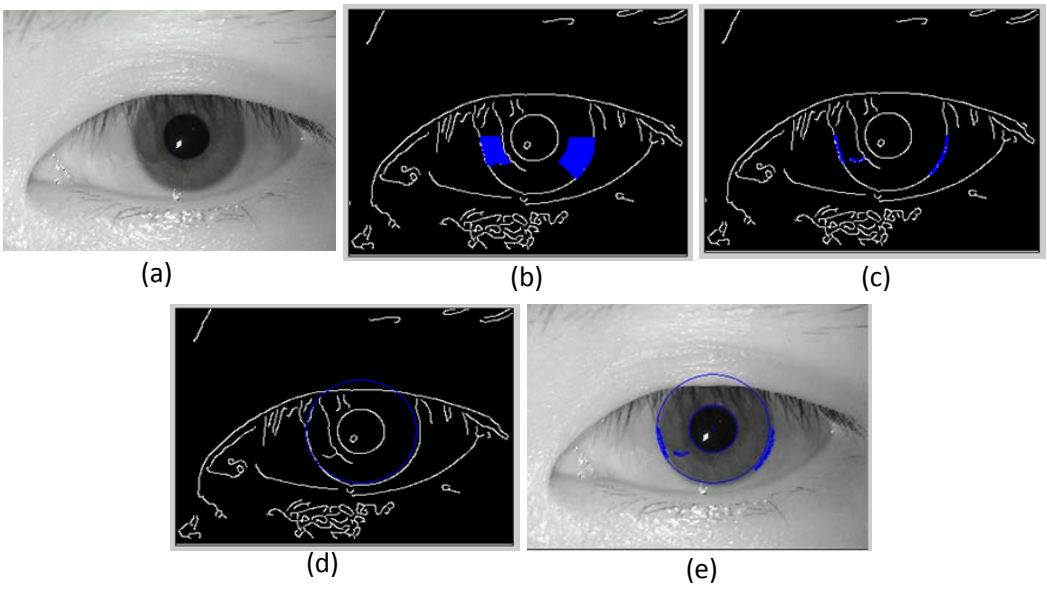

Figure 2.2: Iris segmentation process using Hough transform: (a) original iris image, (b) edge image showing casting of votes using Hough transform (c) edge image showing selected edge based vote casting, (d) edge image showing the fitted circle to the iris boundary, (e) segmented iris image.

The iris boundaries can also be affected by false edges introduced by specular reflections or point source reflection generated by the infrared lightning or user wearing glasses during iris capture. Moreover, it has been found that often, the pupillary and limbic boundaries of the iris are non-circular and can therefore lead to inaccuracies in fitting a simple shape to the iris boundaries. Some other challenges of iris segmentation include: defocusing, motion blur, poor contrast, and oversaturation etc.

2.3.3 Iris Segmentation using Active Contour Method

A paper by Daugman in 2007 [51] explained the use of active contours for fitting iris boundaries. Active contour which has been widely used in image segmentation is an energy minimization spline, which can be operated under the influence of internal contour forces, image forces and external constraint forces. First, the image gradient in the radial direction is calculated and an active contour model based on Fourier series expansion is applied to fit a contour to the image gradient data. The detection of occlusions by eyelids are modelled with separate splines. In any active contour method, there is a trade-off

between how closely the contour fits the data versus the desired constraints on the final shape of the contour. Therefore, Daugman modelled the pupil boundary with weaker constraints than the iris boundary, because he found that the pupil boundary tends to have stronger gradient data than the iris boundary. Daugman's method is dependent on gradient difference between the iris and pupil and/or iris and sclera/eyelid boundaries.

Similarly, Vatsa et al. [54] improved the speed of active contour based iris segmentation by using a two-level hierarchical approach. First, they found an approximate initial pupil boundary. The boundaries were modelled as an ellipse with five parameters. The parameters were varied in a search for a boundary with maximum intensity change. For each possible parameter combination, the algorithm randomly selected 40 points on the elliptical boundary and calculated total intensity change across the boundary. Once the pupil boundary was found, the algorithm searched for the iris boundary in a similar manner, this time selecting 120 points on the boundary for computing intensity change. The approximate boundaries of the iris were refined using an active contour approach. The active contour was first initialized to the approximate pupil boundary and allowed to vary in a narrow band of +/- 5 pixels. In refining the limbic boundary, the contour was allowed to vary in a band of +/- 10 pixels. These methods showed an improvement compared to the traditional circle fitting iris segmentation methods. However, active contour based on the level-set active functional is computationally intensive and is slow to converge. Also, active contour based on edge stopping function is highly sensitive to noise and occlusions which may distort the edges and causes the algorithm to fail. Moreover, active contour based on the stopping function is sensitive to low-contrast between edges. The two main types of active contour methods are discussed in sections 2.3.3.1 and 2.3.3.2.

2.3.3.1 Iris Segmentation Using Active Contour Based On Level-Set Method

Generally, the boundaries of the iris can be defined using a deformable contour described by an active contour model [51-57]. Active contour are of two main forms: active contour based on level-set method and active contour based on variation regional energy. The idea of representing an active contour as the level zero of a higher dimensional function ∅ (which is often a signed distance function) was first introduced

in [89]. Active contour (snakes) model have since been implemented for the segmentation of iris images [53], [56].

Active contour based on level-set (LS) is of the following form: Let Ω represent the image domain, and I represent the iris image. Now, consider evolving a coutour C in Ω, representing the boundary of an open set ω inside the image domain Ω. The active contour embeds the evolving curve as the zero-LS of a higher dimensional function, which can be defined as:

$$\emptyset(x, y, t = 0) = \pm d, \qquad (2.3)$$

Where d denotes the distance from (x, y) to C at time $t = 0$ and the positive or negative sign before d is selected if the point (x, y) is outside or inside the curve C, repectively. The curve evolution function solves the following PDE of the form [53]:

$$\frac{\partial \emptyset}{\partial t} = g(I)(c_1|\nabla_\emptyset| + c_2|\nabla_\emptyset|)\emptyset_0(x, y), \qquad (2.4)$$

Where, c_1 is a constant advection term that causes the curve to either expand or contract uniformly based on its sign, while c_2 is a smoothing function employed to smooth out the high curvature areas of the curve. The set $\{(x, y), \emptyset_0(x, y) = 0\}$ is employed to define the initial contour, while $g(I)$ is an edge stopping function which is used to stop the curve evolution when it hits the boundaries of the iris.

The function $g(I)$ can be defined as [53]:

$$g(I) = \frac{1}{1 + |\nabla G_\sigma(x, y) * I(x, y)|^\rho}, \rho \geq 1, \qquad (2.5)$$

Where, $G_\sigma(x, y) * I(x, y)$ represents the convolution of the image I with the Gaussian kernel $G_\sigma(x, y) = \sigma^{-1/2} e^{-|x^2+y^2|/4\sigma}$. The discretization of $\emptyset$ is achieved by applying a finite difference scheme which was proposed in [56]. In order to evolve the contour, the discretization and linearization of the contour parameters is performed as follows:

$$\emptyset_{i,j}^{n+1} = \emptyset_{i,j}^{n} - \Delta t[\hat{g}(I)(\hat{c}_1|\nabla_\emptyset| + \hat{c}_2|\nabla_\emptyset|)] \qquad (2.6)$$

Now, Δt represents the time step, while (x_i, y_i) represents the grid points between $1 \leq i, j \leq N$, and $\emptyset_{i,j}^{n} = \emptyset(x_i, y_i n\delta t)$ is used to approximate $\emptyset(x, y, t)$ with $n \geq 0, \emptyset^0 = \emptyset_0$. The $c_1|\nabla_\emptyset|$ can be estimated using an upwind scheme as follows:

$$c_1|\nabla_\emptyset| = \left[\max\left(\Delta_-^x \emptyset_{i,j}^n, 0\right)^2 + \min\left(\Delta_-^x \emptyset_{i,j}^n, 0\right)^2 + \max\left(\Delta_+^x \emptyset_{i,j}^n, 0\right)^2 + \min\left(\Delta_+^x \emptyset_{i,j}^n, 0\right)^2\right]^{1/2} \quad (2.7)$$

The term $c_2|\nabla_\emptyset|$ depends on the curvature $k(k = div\left(\frac{\nabla_\emptyset}{|\nabla_\emptyset|}\right))$, which can be estimated as follows:

$$c_2|\nabla_\emptyset| = -\epsilon K\left[\left(\emptyset_{i+1,j}^n - \emptyset_{i-1,j}^n/_2\right)^2 + \left(\emptyset_{i,j+1}^n - \emptyset_{i,j-1}^n/_2\right)^2\right] \quad (2.8)$$

Where ϵ is a constant.

In order to segment the image, the active contour $\emptyset_0$ is initialized and the curve C is evolved to the boundary of the object of interest in the image. Figure 2.3, shows some samples iris images segmented using active contour based on level-set functional.

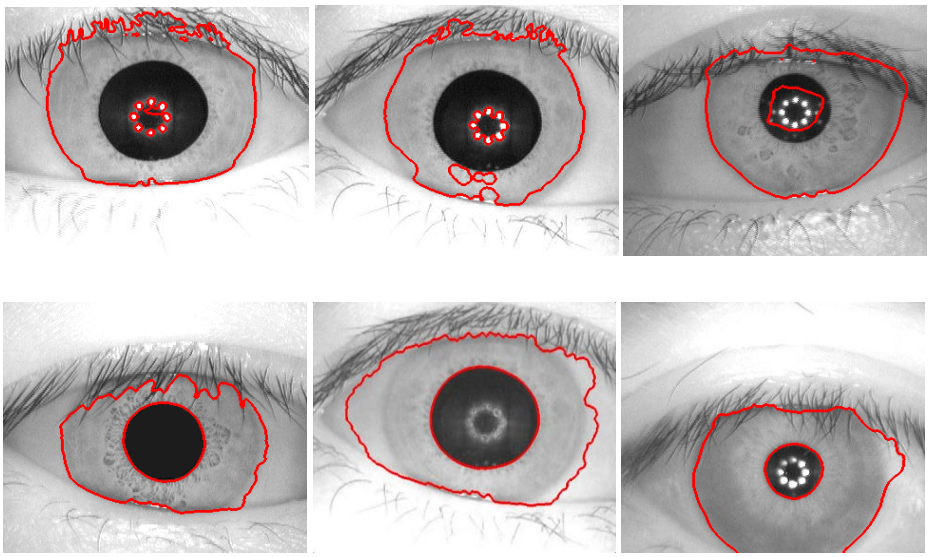

Figure 2.3: Examples of iris images segmented using level-set based active contour model: the upper row shows the effects of reflection of the segmentation model, the lower row shows the effects of eyelashes and smooth boundary between the iris and sclera on the model.

Active contour based on level-set method is able to segment the pupil accurately where the contrast between the edges is high. However, active contour based on level-set have some setbacks. Level-set based active contour is dependent on edge information which makes it difficult for it to segment the iris limbic boundary where there is low contrast between the boundaries. The images on the lower row of Figure 2.3, shows inaccuracies in the limbic boundary segmentation using level-set based active contour.

Also, Active contour based on level-set (LS) function is slow to convergence and is highly sensitive to initialization and noise. The upper row of Figure 2.3, shows the effects of noise and initialization on the iris image segmentation using level-set based active contour. These limitations leads to failure of the level-set based active contour in non-ideal iris images with diverse kinds of noise and occlusion.

2.3.3.2 Iris Segmentation Using Regional Energy Based Active Contour (Chan-Vese Model)

In 2001, Chan-Vese introduced a new active contour model based on regional energy minimization of the variational level-set function [84-85]. This model improved the speed and the accuracy of the standard LS based method significantly. In this study, we apply the Chan-Vese method to segment the pupil and the iris boundaries in order to better understand its strengths and weaknesses. Figure 2.3 is a sample of ideal iris image segmented using the regional energy based active contour (RAC). This showed better result compared to the LS method.

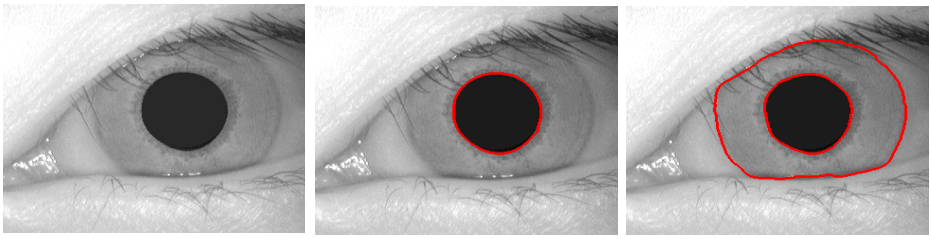

(a) (b) (c)

Figure 2.4: Iris segmentation using regional active contour (RAC) model: (a) original iris image, (b) pupil detection using regional energy based active contour, (c) iris detection using regional energy based active contour.

The active contour model based on regional energy is represented by a parametric curve of the form $v(s) = [x(s), y(s)]^T$, $s \in [0,1]$ which evolves through the iris image to minimize the energy functional:

$$E_c = \int_0^1 \left[\frac{1}{2}(\alpha|v'(s)|^2 + \beta|v''(s)|^2) + E_{ext}(v(s))\right] ds \qquad (2.9)$$

Where α and β are weighting parameters representing the smoothness or tautness of the contour, respectively. While v' and v'' are the first and second derivatives of $v(s)$ with

respect to s. E_{ext} is used to denote the external energy, which yields a small value at the object of interest (OBI), such as edge of the pupil or iris. The typical external energy for a gray-level iris image $I(x, y)$ for seeking edges can be given as:

$$E_{ext}^{1}(x, y) = -|\nabla I(x, y)|^2 \qquad (2.10)$$

$$E_{ext}^{2}(x, y) = -|\nabla[G_\sigma(x, y) * I(x, y)]|^2 \qquad (2.11)$$

Where, $G_\sigma(x, y)$ is a 2D Gaussian function while, σ and $*$ represents the standard deviation and a linear convolution, respectively. Also, ∇ represents the gradient operator. Therefore, at the minima of Equation (2.9), the contour must satisfy the Euler-Lagrange equation:

$$\alpha v'' - \beta v'''' - \nabla E_{ext}(v) = 0 \qquad (2.12)$$

Which can be considered as a force balance equation where $\alpha v'' - \beta v''''$ is the internal force to constrain the contour smoothness and tautness, and $-\nabla E_{ext}(v)$ is the external force that attracts the contour towards the object of interest (OBI). The solution of $v(s)$ is treated as a function of time t which is obtained when a steady state solution of the following gradient descent equation:

$$\frac{\partial v(s,t)}{\partial t} = \alpha v''(s,t) - \beta v''''(s,t) + f_{ext}\big(v(s,t)\big) \qquad (2.13)$$

is reached from an initial contour position of $v(s, 0)$. Now, to achieve a numerical solution to Equation (2.13) on a discrete grid, the discretization of s is iteratively solved using a finite difference approach. The continuous contour $v(s),\ s \in [0,1]$ is sampled and represented by a set of n discrete points $v_i, i \in \{0,1, \ldots., N-1\}$. The update procedure for the entire contour can be written in matrix form as:

$$(I + \tau B)V^{t+1} = V^t + \tau F^t \qquad (2.14)$$

Where I is the $N \times N$ identity matrix, $V^t = [v_0^t, v_1^t, \ldots., v_{N-1}^t]^T$ and $F^t = [f_{ext}(v_0^t), f_{ext}(v_1^t), \ldots., f_{ext}(v_{N-1}^t)]^T$ are $N \times 2$ matrices representing the positions and the external forces of the snakes at the time t, repectively. B is an $N \times N$ cyclic pentadiagonal matrix used to compute the internal force. Since $(I + \tau B)$ is a cyclic symmetric pentadiagonal positive definite matrix, the algorithm can be decomposed by for instance the Cholesky decomposition method.

The generalized RAC has a large capture range and has the ability to capture boundary concavities which is good for segmenting non-ideal iris images with irregular boundaries. Notwithstanding, there are still several unsolved problems, such as the ambiguous relationship between the capture range and the parameters, the sensitivity of the parameters to noise, especially impulse noise like occlusions and false edges and expensive computational cost. Figure 2.5, depicts an excellent pupil segmentation on ideal iris images with less noise and no occlusion on the pupil. However, the performance of the segmentation algorithm deteriorated rapidly with non-ideal iris images as shown in Figures 2.6 and 2.7.

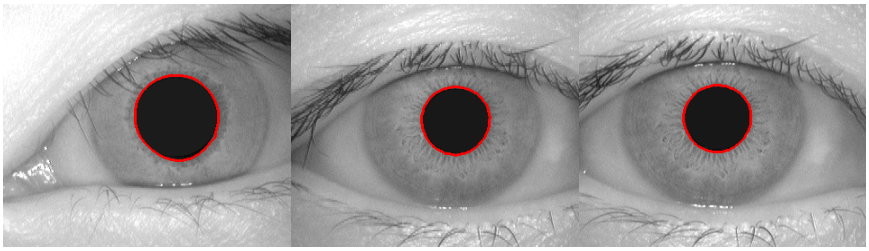

Figure 2.5: Samples of ideal iris images showing the results of pupil segmentation using active contour based on level-set method.

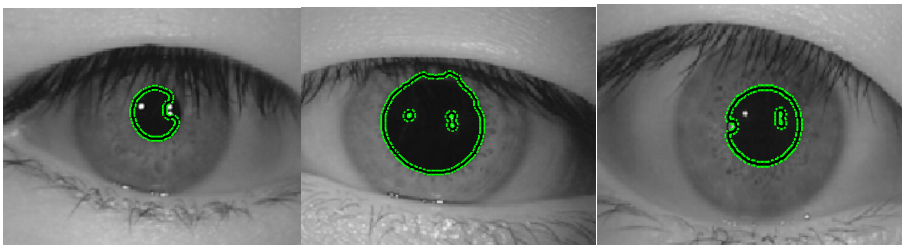

Figure 2.6: Samples of non-ideal iris images with the pupil boundary segmented using active contour based on level-set method.

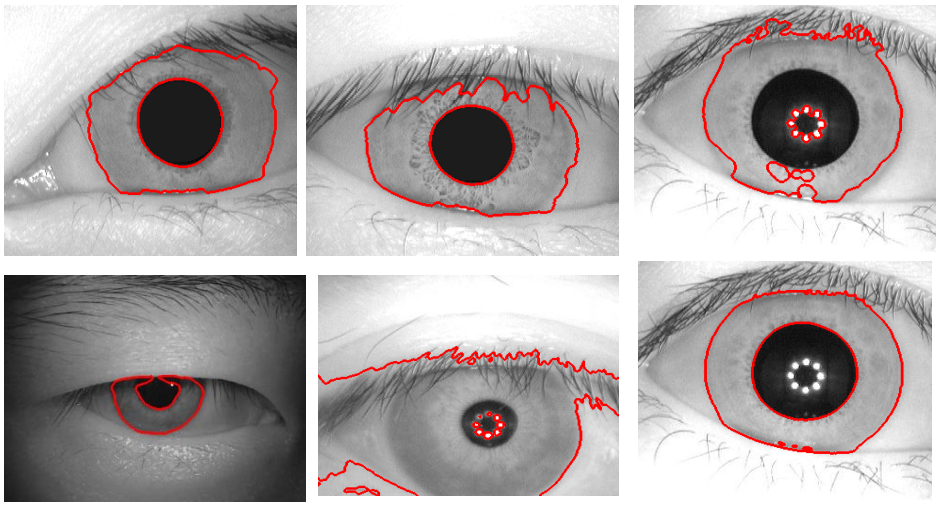

Figure 2.7: Samples of non-ideal iris images showing the results of pupil and iris boundaries segmentation using the RAC model.

The errors in the segmentation results shown in Figures 2.6 and 2.7 are as a result of some properties of the active contour model. Active contour are sensitive to local minima which is the reason why they are attracted to short edges like the reflection edges as shown in Figure 2.6. Also, RAC model is highly sensitive to occlusions and noises like the eyelid and eyelashes (see Figure 2.7).

2.3.4 Graph Cut Optimization

Graph cut optimization remains an active research area in the field of computer vision and graphics [50], [91-99]. Graph cut now forms the basis for many new signal and image processing applications. Researchers and scientists alike have successfully applied graph cut to solve problems like: dynamic programming, shortest paths, Markov random fields, statistical physics, simulated annealing and other regularization techniques, sub-modular functions, random walk, Bayesian networks and belief propagation, integral/differential geometry, anisotropic diffusion, level sets and other variational methods [91-98].

Graph cut is a multidimensional optimization tool which can enforce piecewise smoothness while preserving relevant sharp discontinuities within an image. Graph cut has proven to be an essential tool for interactive image segmentation but its potential for automatic image segmentation has not been fully explored [95]. Image segmentation, which can somewhat be defined as the process of assigning labels to every pixel in an image such that pixels with the same labels share certain visual characteristics, can be stated as a graph cut problem. The main goal of image segmentation is to simplify and/or change the representation of an image into something that is more meaningful and easier to analyse. Segmentation by computing a minimal cut on a graph is quite new but holds huge potentials as a means of dealing with many challenges inherent in noisy image segmentation [96]. This approach guarantees global solutions, which always finds best solutions, and in addition, these solutions are not dependent on a good initialization [91], [95-97]. Also, graph cut is guaranteed to converge and within polynomial time.

A graph is an abstract representation of a set of objects, where several pairs of the objects are connected by links as shown in Figure 2.8. A graph is made up of a set of vertices V also called nodes and a set of edges (arcs) E that connect them. An edge is related to two vertices, and the relationship can be represented as an unordered pairs of

vertices with respect to the particular edge. There are two special vertices in a graph called the source s and the sink t. Therefore, a graph can be said to a mathematical structure which can be used to model pairwise relationship between objects from a certain collection. A cut on the graph known as graph cut is the partitioning of the vertices of the graph into two disjointed subsets (in the case of binary graph). The cut on the graph determines the set of edges that has one end point in each subset of the partition. In a flow network, an $s-t$ cut is a cut that segments the source and the sink into different subsets and it consists of edges going from the source to the sink as shown in Figure 2.8b. There are two main links in a graph namely: the $t-link$, which connects each node to either the source or sink and the $n-link$ which connects one node to another. As shown in Figure 2.8, $t-links$ are shown in either red or blue lines while $n-links$ are shown in yellow lines.

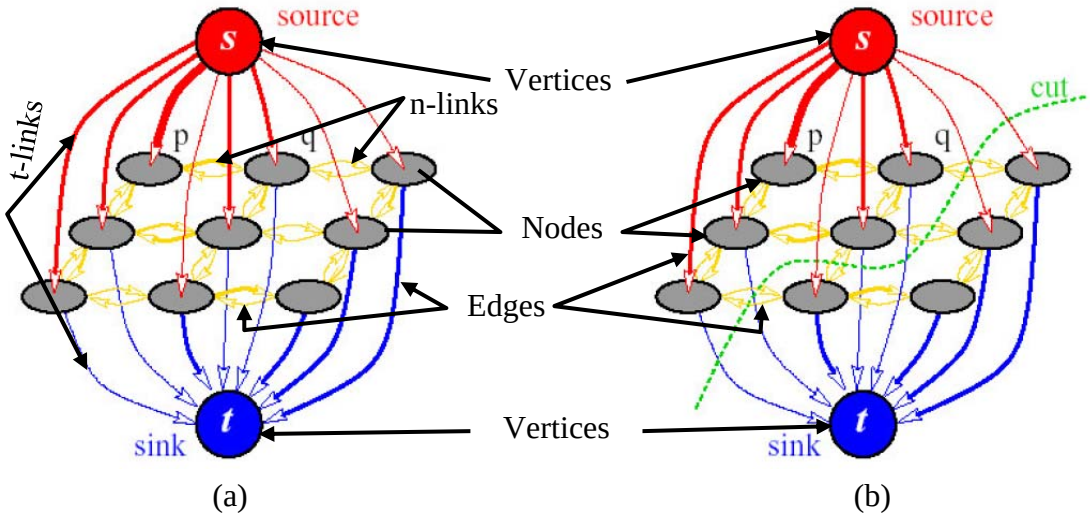

Figure 2.8: Structural diagram of graph cut optimization model [95]

Now, let $\boldsymbol{G} = (\boldsymbol{V}, \boldsymbol{E})$ represent the graph of an image, where $\boldsymbol{V}$ and $\boldsymbol{E}$ denote the set of vertices and edges of the graph $\boldsymbol{G}$, repectively. A weighted graph associates a label (weight) with every edge in the graph. A weight is a number associated with an edge which could represent a distance, time or cost. An $s-t$ graph as shown in Figure 2.8, is a weighted directed graph with two identifiable (binary) nodes, represented as the source s and the sink t. An $s-t$ cut $C(s,t)$, in the graph G is a set of edges E_{cut} such that there is no path from the source to the sink when E_{cut} is removed from G. The cost of a cut E_{cut} is the sum of edge weights in E_{cut}. The flow of the graph $f(u,v)$ is a mapping $f: E \rightarrow R^{+}$, $(u,v) \rightarrow f(u,v)$ which fulfils the conservation of flow and the weight

constraint. The value of the flow is defined by $|f| = \sum_{v \in V} f(s, v)$, where s is the source of the graph which represents the amount of flow passing from the source to the sink. The maximum flow problem can be defined as the maximization of $|f|$ which finds the maximum flow possible from some given source node to a given sink node. The max-flow min-cut theorem states that the maximum value of an $s - t$ flow is equal to the minimum weight of an $s - t$ cut. The main goal of graph cut image segmentation is to construct a graph such that the minimal cut on this graph will cut the boundaries connecting the pixels of the object from the rest of the image.

Therefore, the cut C on the graph is an arbitrary partitioning of the graph nodes into different subsets S and T. A cut on the graph can be defined as a binary labelling of f, whereby labels $f_p \in \{0,1\}$ are assigned to image pixels: if $p \in S$ then $f_p = 0$ and if $p \in T$ then $f_p = 1$. The cost of the cut $C\{S, T\}$ on the graph is computed as the sum of the weights of the various t-links and n-links in the graph. Each image pixel p contributes a regional cost of either $D_p(0)$ or $D_p(1)$ towards the t-link part of the cut cost, which is dependent on the label f_p assigned to the pixel by the cut (see Figure 2.8). The cost of the cut also includes the weights of several n-links $(p, q) \in N$. Therefore, the cut on the graph can be given as;

$$|C| = \sum_{p \in P} D_p(f_p) + \sum_{\substack{(p,q) \in N \\ p \in S,\ q \in T}} \omega(p, q), \qquad (2.15)$$

The cost C is defined by the energy of the corresponding labelling f:

$$E(f) \coloneqq |C| = \sum_{p \in P} D_p(f_p) + \lambda \cdot \sum_{(p,q) \in N} I(f_p = 0, f_q = 1), \qquad (2.16)$$

Where, $I(\cdot)$ is the identity function which gives a value of 1 if the argument is true and 0 if the argument is false. The first term in equation (2.15) is the regional or data term which ensures that the pixel labels f_p agrees with the observed data while the second term is the boundary term which penalizes discontinuities between neighbouring pixels. The parameter λ is used to weigh the relative importance between the data term and the boundary term. Therefore, when λ is very small, each pixel p is assigned a label f_p that minimizes the data cost $D_p(f_p)$ and vice versa. Also, if $\boldsymbol{\lambda}$ is big, then all pixels must choose one label that has a smaller average data cost and vice versa. Noise pixels and other outliers conforms to their neighbours which is one of the main reasons

why graph cut can easily overcome the local maxima problems inherent in the active contour model.

Although, the above approach have shown excellent segmentation results in some natural images, the same cannot be claimed for such images as the iris. This is because, the global optimisation method encounters problems with heterogeneous image like non-ideal iris images with so many artefacts and noise.

2.4 Iris Feature Extraction

2.4.1 Wavelet Transform for Image Feature Extraction

Recent research works on features extraction are focusing more attention on multichannel and mulit-resolutional analysis algorithms such as Gabor filters and discrete wavelet transform techniques. In this work, we have chosen to further study discrete wavelet transform which has the potentials for more efficient texture analysis and have been successfully applied in computer vision and image processing tasks. Wavelet transform is a powerful tool for texture analysis and representation [65], [67], [69], [70], [77]. A wavelet can be defined as a small wave, with an irregular and asymmetric waveform of effectively limited duration that has an average of zero. Wavelet analysis can be likened to breaking up a signal into shifted and scaled versions of the original/mother wavelet. Figure 2.9 illustrates a selection of common mother wavelets used in practical applications. The wavelet transform of a continuous signal, $f(t)$, is given as [85]

$$F_c(\tau, s) = \frac{1}{\sqrt{|s|}} \int_{-\infty}^{\infty} f(t)\psi\left(\frac{t-\tau}{s}\right) dt \quad where\ \tau, s \in \mathbb{R}(s > 0) \qquad (2.17)$$

where the original wavelet is denoted by $\psi(t)$ and the factor $1/\sqrt{|s|}$ is used to conserve the norm. The parameters τ and s denote the location of the wavelet in time and scale, respectively. The elements in $F_c(\tau, s)$ are called wavelet coefficients, each wavelet coefficient is associated to a scale (frequency) and a point in the time domain but without phase information.

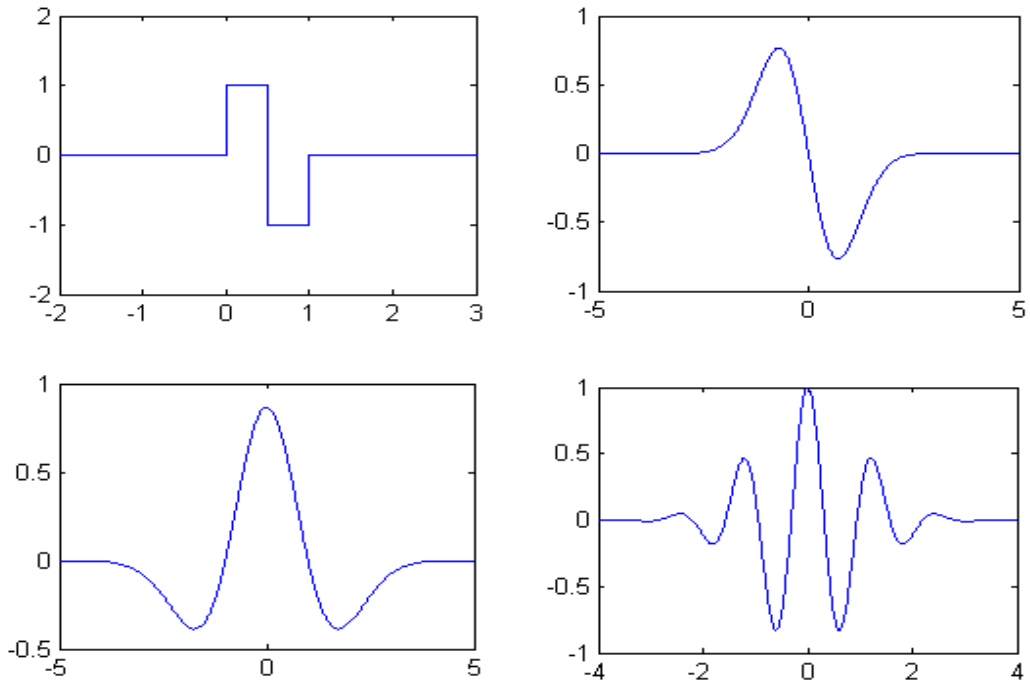

Figure 2.9: Four mother wavelets. (a) Harr. (b) Gaussian wave (first derivative of a Gaussian). (c) Mexican hat (second derivative of a Gaussian). (d) Morlet (real part)

The lack of phase information is a major constraint of DWT for feature extraction. The global information of a signal can be characterised by a large scale transformation which corresponds to the low frequency while, the small scales transformation correspond to high frequency which provides the details of a signal [85]. The decomposition step of a DWT generates two sets of coefficients called 'approximation' and 'detail' vectors which is obtained by convolving the original signal with a low-pass filter and a high-pass filter, respectively, and followed by dyadic decimation, i.e., removing every odd element of an input sequence, as illustrated in Figure 2.10. Reconstruction of the original signal is accomplished by upsampling, filtering, and summing the individual subbands [107].

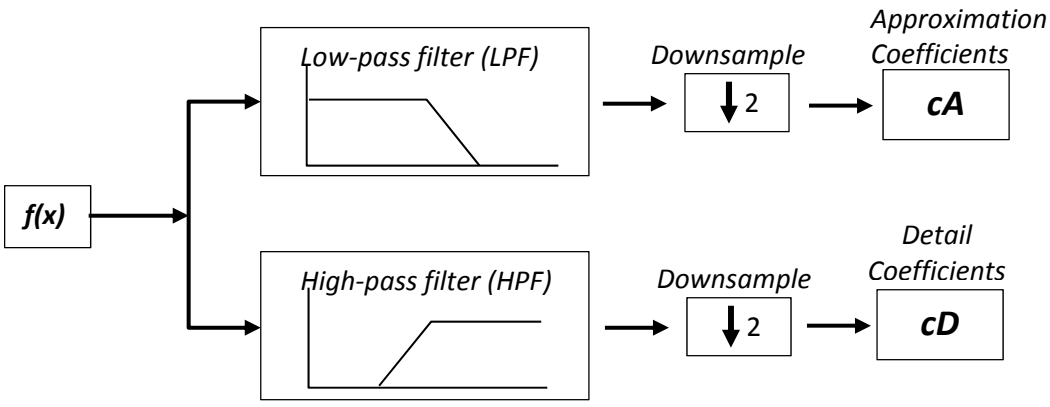

Figure 2.10: One-level decomposition algorithm introduced by [58]. Downsampling process keeps the even indexed elements to reduce the overall number of computations.

Using the same idea, the two-dimensional wavelet coefficients of an image can be achieved by employing separable filters for each dimension (i.e., row and column) along with downsampling process as illustrated in Figure 2.10. The outputs of the decomposition algorithm in Figure 2.11, denoted as; cA, cD_V, cD_H, and cD_D, are called the approximation, vertical detail, horizontal detail, and diagonal detail subbands of the image, respectively.

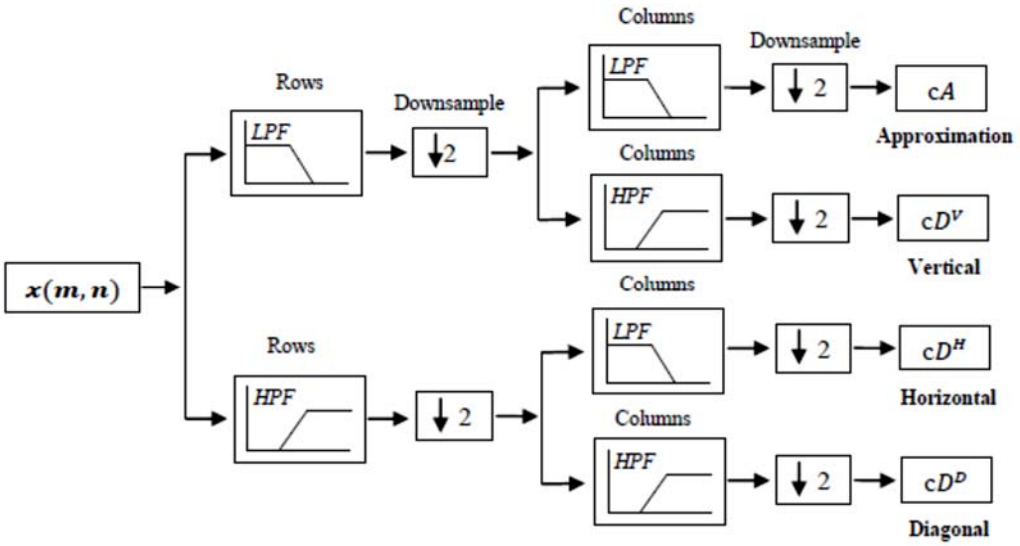

Figure 2.11: Diagram showing one-level DWT decomposition algorithm for a given image.

Although the discrete wavelet transform (DWT) has multi-scale and mulit-resolution benefits for image feature extraction, there still exists some major setbacks. The DWT is based on real valued oscillating wavelets which causes the coefficients to oscillate positive and negative around singularities thereby making singularity extraction very difficult. This means that a small shift in the image signal produces great perturbation in the wavelet coefficient's oscillating pattern around the singularities. Therefore, the problems of shift invariance exists in DWT. Again, DWT suffers from aliasing problems caused by the down-sampling operation. The limitation in directional selectivity is another major problem with DWT. Texture analysis using DWT provides singularities (edges) in only three directions $\{0^0, 45^0, 90^0\}$ and without phase information which limits its rotational selectivity and makes application of DWT to image analysis difficult.

2.4.2 Complex Wavelet Transform

The complex wavelet transform (CWT) is a relatively new development which is based on discrete wavelet transform (DWT) [81-83], [114-115]. The CWT is designed to provide solutions to many of the problems limiting the application of DWT for image analysis. CWT proffers effective solution to most of the major limiting factors of DWT like: shift variance, limited orientation selectivity, aliasing problem (absence of phase information) and oscillations around singularities. These limiting factors greatly hinder the use of DWT for modelling and processing of geometric features of images like ridges and edges. CWT is nearly shift invariant and directionally selective in two or higher dimensions [114]. Higher dimensionality using CWT can be achieved with a minimal redundant factor of 2^d for n-dimensional signal, which is substantially lower compared to the undecimated DWT. Therefore, CWT is a coherent multiscale and multidimensional signal processing algorithm which is able to exploit both the phase and magnitude information of the image unlike the DWT.

Unlike DWT, which uses real-valued oscillating wavelets to analyse signals, CWT employs Fourier transform which is based on complex-valued oscillating sinusoids free from the problems of aliasing, oscillations from positive to negative domain, and shift variance. The complex-valued oscillating sinusoid can be given as [114]:

$$e^{j\Omega t} = \cos(\Omega t) + jsin(\Omega t) \quad (2.18)$$

Where $j = \sqrt{-1}$. The oscillating cosine and sine components corresponding to the real and imaginary parts, respectively, form a Hilbert transform pair (i.e., they are 90^0 out of phase with each other). The magnitude of the Fourier transform does not oscillate positive and negative like DWT but rather provides a smooth positive envelope in the Fourier domain. This simply implies that the magnitude of the Fourier transform is perfectly shift invariant with a small linear phase offset encoding the shift and as such CWT is nearly shift invariant. Also, the Fourier coefficients are not aliased and do not need a complicated aliasing cancellation property to reconstruct the image. The CWT with complex-valued scaling function and complex-valued wavelet can be represented as [115]:

$$\psi_c(t) = \psi_r(t) + j\psi_i(t) \qquad (3.18)$$

Where $\psi_r(t)$ is the real and even part and $j\psi_i(t)$ is the imaginary and odd part of the function. Also, $\psi_r(t)$ and $\psi_i(t)$ form a Hilbert transform pair (90^o out of phase with each other) and therefore, $\psi_c(t)$ is an analytical signal and supported on only one-half of the frequency axis.

Then, the complex wavelet coefficients can be obtained by projecting the signal onto the Fourier domain $2^{jl2}\psi_c(2^j t - n)$, which can be given as:

$$d_c(j,n) = d_r(j,n) + jd_i(j,n) \qquad (3.19)$$

With magnitude

$$|d_c(j,n)| = \sqrt{[d_r(j,n) + jd_i(j,n)]^2} \qquad (3.20)$$

And phase

$$\angle d_c(j,n) = arctan\left(\frac{d_i(j,n)}{d_r(j,n)}\right) \qquad (3.21)$$

Where $|d_c(j,n)| > 0$. The CWT analyses the signals and represents both the real valued signals and complex-valued signals. The CWT enables a multiscale signal analysis that exploits the complex magnitude and phase information. Therefore, a large magnitude indicates the presence of a singularity while the phase indicates its position within the support of the wavelets [111-112], [114-115].

CWT have not been widely applied in signal and image processing due to the complexity of designing complex filters that will meet the perfect reconstruction property. Also, the CWT is only approximately magnitude/phase and shift invariant, which means that its application is still limited. In order to overcome these limitation, Kingsbury [81] designed a dual-tree version of the CWT which employs two trees of real filters in order to generate the real and imaginary parts of the wavelet coefficients. The dual-tree complex wavelet transform (DT-CWT) for 1D signal are as shown in Figure 2.12. The DT-CWT is implemented using two critically sampled DWTs which are in parallel to each other as show in Figure 2.12. The outputs of each tree are downsampled by the summation of the two trees. However, the aliased components of the signal are supressed during the reconstruction stage in order to achieve shift invariance. As shown in Figure 2.12, the upper part of the tree represents the real part of the transformation while the lower part of the tree represents the imaginary part. The idea behind the dual-tree approach is quite simple. The dual tree employs two real DWTs; the first DWT gives the real part of the

transform while the second DWT gives the imaginary part [112]. In the first layer of the decomposition, a sample delay between tree A and tree B is used to ensure that the first layer of the second sample of tree B is just the lost value of A. This is equivalent to not taking the second sample (see Figure 2.12). For subsequent layers of decomposition, there is a half-sample delay interval between tree A and tree B.

Therefore, the practical implementation requires that when odd length biorthogonal filters are used in tree A, even length filters can be used in the other tree in order to ensure uniform interval between samples from the two trees below the first level and satisfy perfect reconstruction (PR) conditions. The two sets of filters are jointly designed so that the overall transform is approximately analytic.

From Figure 2.12, if $h_0(n)$ and $h_1(n)$ denote the low-pass and high-pass filter pair for the upper FB, respectively and $\mathrm{g}_0(n)$ and $\mathrm{g}_1(n)$ denote the low-pass and high-pass filter pair for the lower FB.

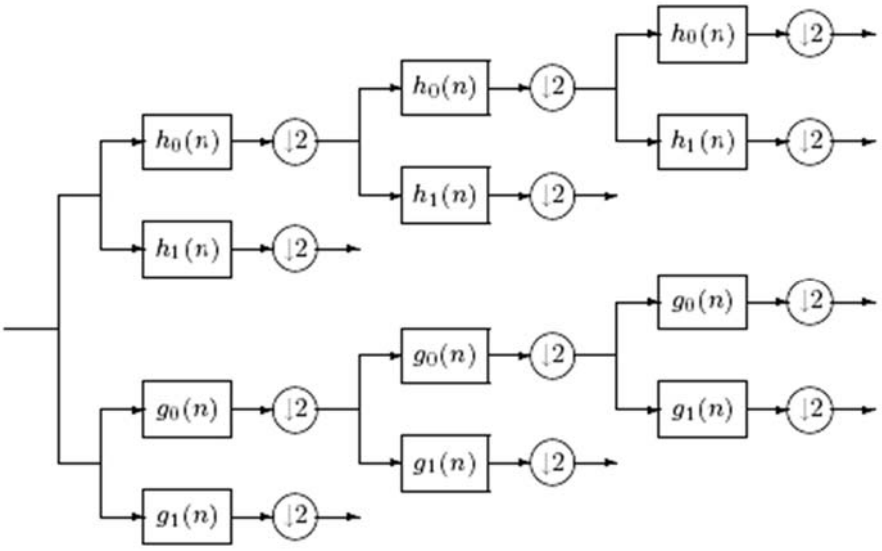

Figure 2.12: Diagram of the analysis FB for the dual-tree CWT.

Then, the two wavelets associated with each of the two real wavelet transforms can be represented as $\psi_h(t)$ and $\psi_{\mathrm{g}}(t)$. Therefore, the filters are designed so that $\psi_{\mathrm{g}}(t)$ is approximately the Hilbert transform of $\psi_{\mathrm{h}}(t)$ which is denoted as $\psi_{\mathrm{g}}(t) \approx \mathcal{H}\{\psi_h(t)\}$.

The extraction of the rich and complex iris textures demands the implantation of multi-scale, multiresolution analysis approach. DT-CWT which is a multi-scale, multiresolutional wavelet transform based on the Fourier representation of the signal is well suited for this task. The extension of DT-CWT from one dimension to two dimensions provides for even greater directional selectivity. The extension is achieved

through separable filtering. The real textured images contains relevant information in both the first and second quadrants of the spectrum. Therefore, the column filter outputs are also filtered by the complex conjugates of the row filters in order to elicit more information. This gives rise to 4:1 redundancy for two dimensional signals. Therefore, the subsampled outputs of the row filters and their complex conjugates form six bandpass images, three in each quadrant. These subimages are strongly oriented at $\pm [15^o, 45^o, 75^o]$. These orientations are obtained by separating the complex filters into positive and negative frequencies in both horizontal and vertical directions [110]. The many advantages of DT-CWT highlighted here include: multi-scale and multi-resolution analysis ability, magnitude/phase and shift invariance, non-aliased, etc. However, some major setbacks still exist with 2-D DT-CWT. The DT-CWT is only strongly oriented in six direction which is a limitation to its rotational selectivity. Greater orientation selectivity will be highly advantageous for iris feature representation.

2.5 Related Works

2.5.1 History of Iris Biometrics

The history of person identification based on iris dates back over 100 years [1-14]. However, automatic iris recognition is relatively more recent, dating back only decades ago [7-15]. In 1882, a French police officer Alphonse Bertillon carried out the first research trying to use eye measurements to identify criminals [1], [6] and later in 1886, Bertillon [1], suggested that the human eye (eye colour) can be used for biometric recognition [16-18]. Later, in 1936, Frank Burch [7] first proposed the use of iris patterns for human identification. In a clinical textbook "Physiology of the Eye" of 1953 where F. H. Adler [3] contributed a chapter, he described how the marking of the iris are so distinctive that the photographs of the iris can be used as a means of identification, instead of the fingerprints. Apparently, Adler's work was based on comments by a British ophthalmologist J. H. Doggart [2], who in his book "Ocular Signs in Slit-Lamp Microscopy (OSSLM) 1949 has written that "*Just as every human being has different fingerprint, so does the minute architecture of the iris exhibit variations in every subject examined*." The first patented work on iris recognition was that of Flom and Safir in 1987 [4]. They obtained a US patent for an unimplemented conceptual design of an automated iris biometrics system which is based on Adler's and Doggart's earlier proposals. However, it was in 1992 that a breakthrough study by Johnston [5], proved that the

patterns of the iris remains stable for a period of at least 15-months interval. The research was based on iris images acquired from 650 individuals in the interval of 15-months. Their report highlighted the complexity of an iris image, including specular highlights and reflections. The report concluded that iris biometrics held a potential for both verification and identification tasks, but no experimental results were presented to support their report.

The pioneer research work and the basis for almost all commercially implemented iris biometric systems is the work of Daugman [8-11], [14-15]. In 1994, Daugman [8-9] patented a publications describing an operational iris recognition system in some detail. Daugman's approach has now become a standard reference model for Iris biometrics as the field has continued to develop with his concepts. Almost all current commercial iris biometric technologies are based on Daugman's work due to the Flom and Safir patent and the Daugman patent being held for some time by the same company.

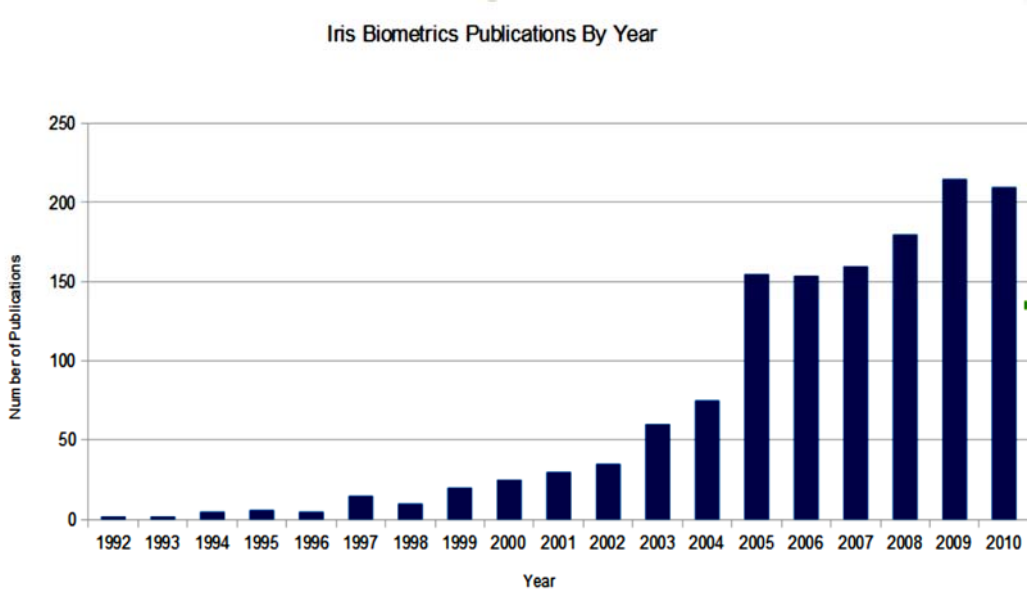

Figure 2.13: Iris biometric publication by year [15].

Although, Daugman's algorithms still remains significant in public deployments of iris recognition, academic research into many areas of iris technology have exploded within the last decade. Figure 2.13, shows a chart of iris biometrics publications by year up till 2010. As can be seen from the chart, there has been a geometric progression in research into the field of iris recognition in the last few decades. Also, in a survey papers presented by Bowyer *et al.,* [16-18], there were over 1,000 published papers that addressed different areas of iris biometric technology during the last few years.

2.5.2 Review of Selected Relevant Literatures

Daugman [8], [11], proposed the traditional iris segmentation approach based on the approximation of the pupillary and limbic boundaries of the iris as circles. Given the acquired eye image, an integro-differential operator was proposed for detecting the iris inner and outer boundaries through an N-dimensional search of the image parameter space. Following the correct segmentation of the iris region, Daugman proposed a normalization process based on the rubber-sheet model which transforms the iris from radial coordinate system to polar coordinate system for size invariance. The normalized iris image is then convolved with 2-D Gabor filters in order to extract the rich textural information of the iris sample. He proposed Hamming distance (HD) as a measure of similarity between the iris template and other templates held in the database. Daugman's approach yielded an impressive performance where high quality iris image acquired under constrained imaging condition is applied.

Similarly, Wildes [12], proposed the localization of iris boundaries by computing the binary edges followed by Hough transform. Hough transform considers the set of edge points and finds a circle that best fits most edge points representing the iris boundary. Wildes also applied Laplacian of Gaussian filters at multiple scales in order to compute the iris template. Correlation was adopted as a similarity measure in order to obtain the similarity between the iris templates. Wildes [12], demonstrated the effectiveness of his approach. His approach show an improved speed compared to Daugman's approach. However, these two traditional iris recognition system are based on the assumption that iris boundaries are circular. The pupillary and limbic boundaries of the iris are not perfectly circular or elliptical, which is a major source of error to shape dependent models adopted in Daugman's and Wilde's approaches. Also, in Daugman's approach, the search through the N-dimensional parameter space is inefficient and computationally intensive.

In an effort to overcome these challenges, many new modifications or combination of the traditional segmentation approaches began to emerge in literature. In [19], Masek proposed a modified method based on the application of circular Hough transform for the detection of the iris and pupil boundaries. He then employed 1D log-Gabor filters for the extraction of the iris features while HD was used for template matching. Also, Tisse et al., [20] proposed a segmentation method based on the combination of integro-differential operators and Hough Transform. His method was able to reduce computation time and excluded potential centres that lies outside of the eye image. However, it did not consider eyelash occlusions and noises which might influence

the results of the algorithm. Liam et al. [21], proposed a simple method based on thresholding and function maximization in order to obtain the two ring parameters representing the iris inner and outer boundaries. While, in [22], Liu et al. adopted a modification of the circular Hough transform to improve the iris segmentation. They applied a noise reduction and a hypothesis-and-verify scheme to improve the accuracy and robustness of Wildes method. Also, they introduced an eyelid detection technique where, the upper and lower eyelids are modelled as two straight lines. In another approach, Trucco and Raseto [24], proposed to find the optimal circle parameter of the iris boundaries by a simulated annealing algorithm. All these methods tried to either improve speed or accuracy but not both. Also, eyelids/eyelash occlusions as well as other noise factors were not given proper considerations.

Soon, researchers began to pay more attention to noise and occlusion detection in iris segmentation [25-36]. In [25], Haung et al., proposed a coarse segmentation of the iris using edge detection filters and Hough transform before normalization. The noise due to eyelids and eyelashes are then segmented by edge information based on phase congruency method. In [26], Li Ma et al., proposed an iris recognition approach based on characterizing key local intensity variations. The basic idea was to use the sharp local variation points to represent characteristics of the iris boundaries. Feature extraction was performed by constructing a set of 1D intensity signals to isolate the most important information from the original 2D image. A position sequence of local sharp variation points in such signals were captured as features, using a particular class of wavelets. A matching scheme based on the XOR operation was then adopted to measure the similarity between a pair of position sequences. These methods failed to consider low quality iris image captured under less constrained imaging conditions which limits its applicability.

Nowadays, the challenges posed by non-ideal iris images captured in less-constrained imaging conditions have started to catch the attention of researchers and scientist alike [37-57]. In [39], Schuckers et al. tried two different approaches of handling “off-angle” irises. In both approaches, they sought to transform an off-angle image into an equivalent frontal image before segmentation. Also, He et al. [43-45], presented an iris boundaries segmentation based on pulling and pushing method. A cascaded Adaboost learning algorithm is first implemented to learn if the input image is an iris image and the rough position of the centre and size of the iris in the image. The final segmentation of the iris boundaries is then achieved based on edge fitting and the pulling and pushing method. The eyelids were segmented using edge detection followed by curve fitting process, while eyelash detection is achieved using a learned statistical prediction

approach. Proenca and Alexandre [46-48], proposed a segmentation method which first extracts the position and intensity feature information for each pixel of the iris image and applies fuzzy k-means clustering algorithm on the feature vector to produce a normalized intermediate image. Edge map construction is then applied to localize the boundaries of the iris using the normalized intermediate image. Their results showed that this method significantly improved edge map based segmentation methods for non-ideal iris images. Ryan et al. [49] presented an alternative fitting algorithm, called the Starburst method, for segmenting the iris. The iris image is first filtered using a smoothing filter and a gradient detection filter. Then, the darkest 5% of the image pixels was set to black, and all other pixels to white. A Chamfer image was then created where the darkest pixels in the Chamfer image are the pixel farthest from any white pixel in the threshold image. They used the darkest point of the Chamfer image as a starting point for iris segmentation. Next, they computed the gradient of the image along rays pointing radially away from the starting point. Two highest gradient locations assumed to be points on the pupillary and limbic boundaries were retained. The detected points were fit with several ellipses using randomly selected subsets of points. An average of the best ellipses was reported as the final boundary. The eyelids were detected using active contour method. Pundlik et al. [50] presented another alternative segmentation algorithm based on graph cut. Their algorithm was a labelling routine instead of a fitting routine like the Starburst method. Their first goal was to assign a label - either “eyelash” or “non-eyelash” - to each pixel. Then after removing specular reflections, the gradient covariance matrix was used to measure the intensity variation of each pixel in different directions. Eigenvectors and eigenvalues obtained using the gradient covariance matrix are used to create a probability map, P that assigns the probability of having high texture in its neighbourhood or not to each pixel. The “energy” corresponding to a particular labelling of the image pixel was written as a function of a smoothness term and a data term. The data term was based on a texture probability map. They treated the image as a graph where pixels were nodes and neighbouring pixels were joined with edges, and they used a minimum graph cuts algorithm to find a labelling that minimized the energy function. The second goal was to assign each pixel a one of four labels: eyelash, pupil, iris, or background. They used a method similar to the initial iris segmentation for this; however, this time they used an alpha-beta swap graph-cut algorithm. Finally, they refined their labels using a geometric algorithm to approximate the iris boundaries with an ellipse. This is computationally intensive method given the alpha beta swap for all the pixels of the image is very tasking.

Although most of these approaches yielded good results, many of them are based on supervised learning which is computationally intensive.

Recently, the application of active contour model for the segmentation of the iris boundaries began to gain the attention of many researchers [51-57]. In [51], Daugman proposed a new method of segmenting iris boundaries using active contours based on the Fourier series approximations to the iris data. He adopted a statistical inference method for detection and exclusion of the eyelashes. Feature extraction and matching were conducted using Log-Gabor filtering and Hamming distance computation, respectively. Also, in [52], Shah and Ross proposed the segmentation of iris boundaries using geodesic active contour model. The pupil is first segmented by a binarization method followed by circle fitting to the pupil's boundary. A contour is then initialized and evolved from the pupil boundary toward the iris boundary in order to determine the accurate boundary of the iris. Vatsa et al. [54] tried to improve the speed of active contour segmentation by using a two-level hierarchical approach. First, they found an approximate initial boundary of the pupil. Then, the boundary was later modelled as an ellipse with five parameters. The parameters were varied in a search for a boundary with maximum intensity change. For each possible parameter combination, the algorithm randomly selected 40 points on the elliptical boundary and calculated total intensity change across the boundary. Once the pupil boundary was found, the algorithm searched for the iris boundary in a similar manner, this time selecting 120 points on the boundary for computing intensity change. The approximate iris boundaries were refined using an active contour approach. The active contour was initialized to the approximate pupil boundary and allowed to vary in a narrow band of +/- 5 pixels. In refining the limbic boundary, the contour was allowed to vary in a band of +/- 10 pixels. This approach can lead to failure of the algorithm if the first step of the process is erroneous. Therefore, a new method is highly needed to address the challenges of effective and efficient segmentation of non-ideal iris images.

In similarly way, a lot of different techniques for iris feature extraction have been proposed in literature [12], [58-81]. A survey paper by Patil et al. [76], summarised enormous number of papers and their different alternative methods for iris feature extraction. Daugman [8-11], was first to apply the 2-D Complex Gabor filters to extract the rich iris information. Gabor filters have been extensively used in computer vision and machine learning, especially for texture analysis. Gabor method is capable of extracting the visual properties of the iris in different directions but it naturally suffers from some setbacks. The Gabor filter is an even symmetric filter which has a DC component that is affected by the changes in the background illuminations of the image. Also, Gabor filter

is not completely a band pass filter therefore, Gabor function tends to overrepresent the low frequency component of the filter and also underrepresent the high frequency component of the filter [61], [81-82]. These setbacks can easily be overcome by applying some modification or using the Log-Gabor version of the filter. The 2-D Log-Gabor filters have witnessed great popularity in image processing field. The Log-Gabor filter did not inherit the DC component problem of Gabor filters therefore, it is better able to handle textured image information. In [121], Yao et al. in their paper "Iris recognition algorithm using Modified Log-Gabor Filters" was able to represent iris features using Log-Gabor method. Also in [61], the multichannel Gabor filter-based iris recognition scheme was proposed, and in [62], the circular symmetry filters were used for iris recognition. These methods tried to improve the complex Gabor wavelet method earlier proposed by Daugman. However, the improvements comes with a cost. The slow speed of techniques like the 2-D Log Gabor filter or multi-channel Gabor filter is a source of worry.

In another approach, Boles and Boashash [12], [32], was first to propose iris feature extraction technique based on wavelet transform (WT) zero crossing. They implemented a wavelet function which is the first derivative of the cubic spline for the construction of the iris feature representation. Similarly, Rydgren et al. [65], proposed an iris feature extraction technique based on wavelet packets. They determined that feature extraction techniques based on discrete wavelet functions are generally faster compared to Gabor method. However, discrete wavelets normally suffer from shift variance and lack of phase information. Wavelet packets is an extension of the discrete wavelet transform which combines the idea of best basis selection and entropy basis criteria for signal representation.

In [63], a new method based on Discrete Cosine Transform (DCT) was introduced for iris feature extraction. Also, Belcher and Du [71] proposed a region-based scale invariant feature transform (SIFT) approach for iris feature extraction. They cited multiple advantages of using SIFT namely: the method "does not require highly accurate segmentation, transformation to polar coordinates, or affine transformation". They divided the iris area into three regions: left, right, and bottom. Each of the regions is then subdivided into more sub-regions, each containing a potential feature point. The unstable points are first eliminated before finding the dominant orientation and feature point descriptions using the SIFT approach. When comparing two images, they only compared a feature from a given sub-region in the first image with the corresponding sub-region in the second image, or with the eight nearest sub-regions in the second image.

Bodade and Talbar [81] suggested the use of a 2D Dual Tree Complex Wavelet Transform (CWT) and a 2D Dual Tree Rotated CWT which provided shift invariant features in more directions than a Discrete Wavelet Transform (DWT) and are more computationally economical than Gabor filters. Although this technique is highly promising, it is not rotationally invariant.

A more comprehensive review of iris recognition literatures can be found in a survey paper presented by Bowyer et al. [16-18] and [76] which listed an enormous number of papers which have tried alternative methods of iris recognition. Very few researches have been conducted using graph cut optimization, complex wavelet a filters (CWF), particle swam optimization (PSO) and SVMs. In this research, we develop and iris recognition system based on combination of graph cut optimization and active contour for the robust segmentation of iris image, and a principally rotated complex wavelet filters (PR-CWF) was adopted for iris feature extraction while feature selection is achieved using particle swam optimization (PSO). The classification of the iris templates is achieved using SVMs.

2.6 Summary

In this chapter, some key iris segmentation approaches are presented which includes IDO, Hough transform and active contours. Also, a background study of graph-cut optimization is also presented which aims at unearthing the characteristics and advantages of graph-cut energy minimization technique. Moreover, a feature extraction technique based on wavelet transform and complex wavelet transform were analysed to highlight their strengths and weaknesses. Then, a brief summary of the some related works that are important to this study is presented as discussed. Despite all the research and developments in the area of iris recognition, the segmentation and feature representation of non-ideal iris images remains unsolved. In the coming chapter, an efficient and effective solution to iris segmentation using graph cut based active contour will be presented.

Chapter 3

3. IRIS SEGMENTATION FOR IRIS BIOMETRICS

In this chapter, a novel fast and accurate iris segmentation method for accurate estimation of the inner (pupil) and outer (limbic) boundaries of the iris is presented. This chapter mainly focused on addressing the common problems of iris segmentation including: irregularity of iris boundaries, noise and reflection, occlusions from eyelids and eyelashes, blurriness and non-uniform illuminations. To achieve these objectives, the iris boundaries are modelled using a dynamic approach based on graph-cut energy minimization and active contour model (GCBAC). In section 3.1, we briefly presented a short background of the problem. Then, in section 3.2, other related works are considered and reviewed in brief. Section 3.3, describes the pre-processing steps for detecting and eliminating any specular reflections that might be present in the original eye image. While in section 3.4, we present the process of localizing the pupil and limbic boundaries of the iris. Section 3.5, describes other post-processing steps which is aimed at refining the segmentation result and dealing with other artefacts like occlusion. The samples of the segmentation results are provided in section 3.6, and finally in section 3.7, a summary of the key points of this chapter is presented.

3.1 Overview of the Proposed Approach

In non-ideal iris images, the low quality images captured under low-constrained imaging condition can be heavily affected by noise and other artefacts which can negatively impact on the segmentation result. Generally, most iris segmentation algorithm tries to enhance the quality of the image before segmentation. Also, most current segmentation algorithms carry out iris boundaries segmentation in two dependent steps. However, in this work, we propose a 2-level 2-step hierarchical process for iris boundaries segmentation. The two levels are carried out independently in order to contain errors. The

algorithm starts by first estimating the rough boundary of the pupil before the finally segmenting the pupil through a refining process. Also, the outer (limbic) boundary is segmented using the same process. Figure 3.1, illustrates the main components of the proposed iris segmentation framework.

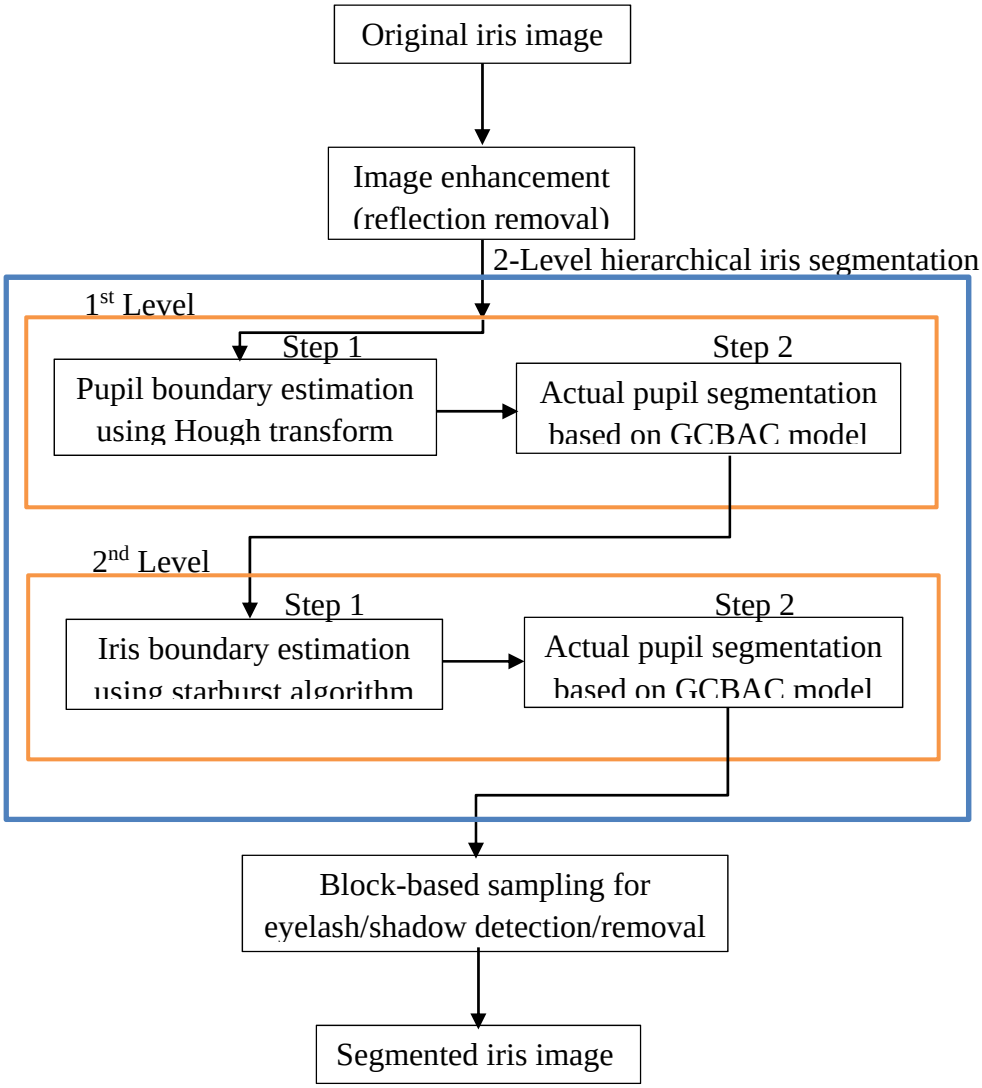

Figure 3.1: The block diagram showing the main components of the proposed iris segmentation approach. Pupil and iris segmentation on two levels hierarchical approach as well as pre-processing and post-processing processes for noise detection and removal.

The segmentation process uses grayscale component of the original iris image. Therefore, visible wavelength (VW) images where they exists are first converted to grayscale image before the segmentation process.

3.2 Introduction

Most current iris recognition algorithms have reported high performance and accuracy from their experimentation and testing. However, their performances are usually based on ideal iris images obtained in highly constrained environment, where the images are acquired using very sophisticated imagery setup. The performance of such system can deteriorate quickly when low quality iris images acquired under less co-operative imagery environment are used. The quality of an image is a major factor in most pattern recognition problems. Low quality images often present distorted patterns or misleading information which can result in false rejection. With the diversification of iris recognition to areas such as schools, hospitals, airport, banks, border control, and prisons, iris based authentication systems have now become quite popular and now implemented for surveillance and monitoring. Low quality iris image captured on the move, in a user operated setting, or at a distance are fast becoming the order of the day in modern implementation of iris recognition. Figure 3.2 shows samples of non-ideal iris images obtained under flexible imaging setup.

In a constrained capturing setup, subjects are conditioned to stop and look into the iris camera from a predetermined distance, position their head and sight, and then, their iris images are captured. However, in unconstrained iris imaging system, the iris image can be capture on the move, at a distance of up to 8 meters or in a user operated environment. Iris images captured in such an unconstrained environment normally result in non-ideal iris images with varying levels of noise and artefacts present. In non-ideal iris images, the iris region may be severely occluded by eyelids, eyelashes and shadows, the eye may not be properly opened, or the iris may be obscured by specular reflections and other artefacts. These noise factors can have severe effects on the segmentation results, and consequently, the overall recognition accuracy. The non-ideal iris images are normally affected by noises like: motion blur, camera diffusion, head rotation, gaze direction, camera angles, reflections, contrast, luminosity, and other size and shape irregularity problems due to contraction and dilation of the pupil [44], [48].

Several iris recognition methods have been proposed by many researchers and scientists alike to effectively tackle the different aspects of iris recognition [8-57]. While most of the researches are focused on ideal iris images, recently, there have been a new important directions for iris based biometrics researches. The strive for development of a robust iris segmentation algorithm as well as non-invariant multiscale and multiresolution

feature extraction and selection technique for representing the important textural features of “non-ideal iris images” is shifting the boundaries of research today. In this chapter, we deploy a methodology to compensate for the various non-idealities found in non-ideal iris images in order to effectively and efficiently define the inner and our boundaries of the iris. Our main interest is to improve the iris recognition performance though accurate and efficient localization of non-ideal iris images, captured under a flexible imagery setup. Figure 3.2 show some samples of non-ideal iris images which are obtained from CASIA and UBIRIS iris databases. The non-idealities found these images ranges to various degrees from occlusion, specular highlights, blur, variations in illumination, to dilation and constriction of the pupil.

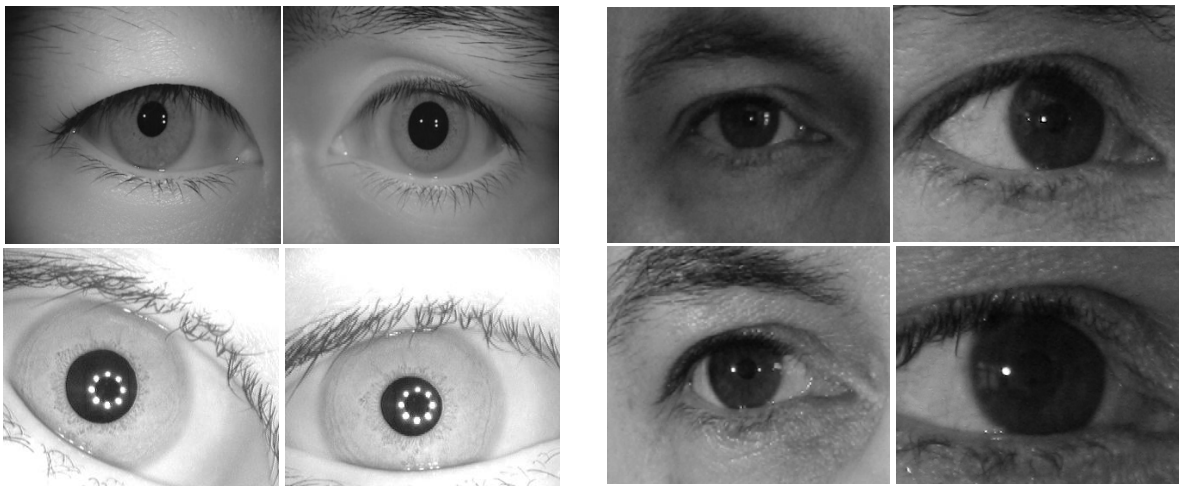

(a) (b

Figure 3.2: Samples of non-ideal iris images taken from CASIA and UBIRIS datasets: (a) images from CASIA iris dataset, (b) images from UBIRIS dataset.

Therefore, a new and enhanced method for coping with the various challenges of non-ideal iris images needs to be developed. From the sample iris images shown in Figure 3.2, the different shapes of iris boundaries can be seen. Therefore, the general assumption that iris boundaries are circular or elliptical can no longer hold for non-ideal iris images. For instance, in iris images where the eye is half open, the highly occluded regions can be extracted, which leads to false recognition and thus, the segmentation performance can be greatly affected [51]. Considering these challenges, a new and improve method of iris segmentation algorithm is developed here for non-ideal iris image segmentation.

In this chapter, we propose a two-level two-step hierarchical approach for iris segmentation. The first level of the segmentation process deals with the segmentation of the inner (pupil) boundary, while the second level performs the outer (limbic) boundary

segmentation. Each of the iris boundaries are segmented in two steps. This design is aimed at containing and resolving any segmentation error within each level/step and making sure that errors at one level or step does not affect the segmentation result in subsequent levels or steps. In the first step of the first level, the rough approximate boundary of the pupil is estimated. Subsequently, in the second step of the first level, a contour is initialized on the estimated boundary obtained from the first step and the contour is then evolved to the actual boundary of the pupil. Similarly, in the second level of the hierarchy, the same procedure is repeated again for the segmentation of the limbic boundary. The final contour at each level is estimated by refining the initialized contour using graph-cut energy minimization based on active contour model (GCBAC). Before the start of the segmentation process, an initial pre-processing step is carried out on the image to detect noise and specular reflections that are usually present in non-ideal iris images. Then, after segmentation, a post-processing method is also employed to detect and exclude any superimposed eyelashes/shadows which might be present in the iris image.

In the pre-processing step, the highest intensity areas of the original iris image are marked out and a multiscale edge weighted high-pass filter is developed to detect closed contours within the highest intensity areas representing reflections regions. Closed contour within the highest intensity areas are identified as holes representing reflection points in the iris image. The detected reflections are then filled using a modified adaptive exemplar based image in-painting method [104]. In order to approximate the initial pupil boundary, the pre-processed iris image is complimented and a circular Hough transform is deployed to directly search for circles in the iris image. Detected circles are further refined to find the circle representing the approximate pupil boundary. A contour is then initialized around the approximate boundary and graph cut based active contour (GCBAC) is applied to finally segment the pupil boundary. Once the pupil final boundary has been determined, the same procedure is repeated to segment the iris boundary except that this time an energy based starburst algorithm is developed and used for the rough approximation of the limbic boundary in the first step. The limbic boundary has lesser contrast between the boundary compared to the pupil boundary and it is normally occluded with eyelids and eyelashes. Therefore, the earlier method based on Hough transform used for approximating the pupil boundary will fail in the case of limbic boundary. An energy based starburst algorithm is therefore used to search of energy transition in different angles along rays pointing from the centre of the image to the

boundary of the image. The energy transition points are detected and refined and finally a contour is initialized on the points to represent a rough estimate of the limbic boundary.

Finally, in order to model the small short variation in intensity of the iris as a result of superimposed eyelash or shadow pixels, a block based approach is adopted to calculate local energy of each pixel in each image block and predict the absence or presence of eyelash or shadow per block. The image is first partitioned into non-overlapping blocks and blocks are then classified into candidate eyelash (CEL), non-candidate eyelash (NEL) and approximate eyelash (AEL) based on the sharpness and smoothness of the block. The blocks are classified using a Bayesian classifier which is a simple probabilistic classifier based on the application of the "Bayes theorem" with strong naïve independence. Finally, eyelash/shadow pixels are detected using statistical prediction method.

3.3 Reflection Detection and Removal

In the first phase of the iris segmentation process, a method is employed to detect and remove reflections which is capable of influencing the iris recognition performance. Reflections when they occur within the iris portion is capable of introducing spurious information into the iris pattern, which can degrade the recognition accuracy. Also, when reflection occur near the iris boundaries, they normally possess stronger properties than the properties of the pupil or iris edges which means that it is capable of influencing the segmentation algorithm and leading to erroneous segmentation. Therefore, it is very important that a fast and accurate algorithm for detecting and removing reflections without greatly altering the iris structure is developed.

Reflection detection and removal or more generally object detection and removal is a very challenging task in computer vision and image processing due to vast variations in the shapes and locations of objects in an image. Reflections in iris images can be classified into weak and strong reflections according to their intensity levels. Most popular methods for detecting and removing/filling reflection in iris images tend to significantly alter the iris structure making further processing with the same image difficult. For instance, one of the most popular methods for reflection removal is by evolving the image with a partial differential equation (PDE) called flood filling [29-30], [47], which interactively erodes away the specular reflection component at each pixel. Although, this method tends to yield impressive results, it significantly alters the structure

of the iris image and reduce its quality significantly. Figure 3.3, illustrates the process and shows the result of reflection removal using the flood filling approach. Original iris image is first complemented and a flood filling is performed on the entire image before the image is complemented back to its original form again. Although this method seems to produce a good visual result, the structure of the iris image is greatly altered to a large extent which may affect further processing using the same image.

Other methods of specular reflection removal in iris images include: interpolation method, radial autocorrelation, and mathematical morphological approach to mention but a few. These methods suffers from either limited accuracy or speed which is a major hindrance to its practical implementation. Some of them also greatly alter the structure of the iris image in the process of reflection removal.

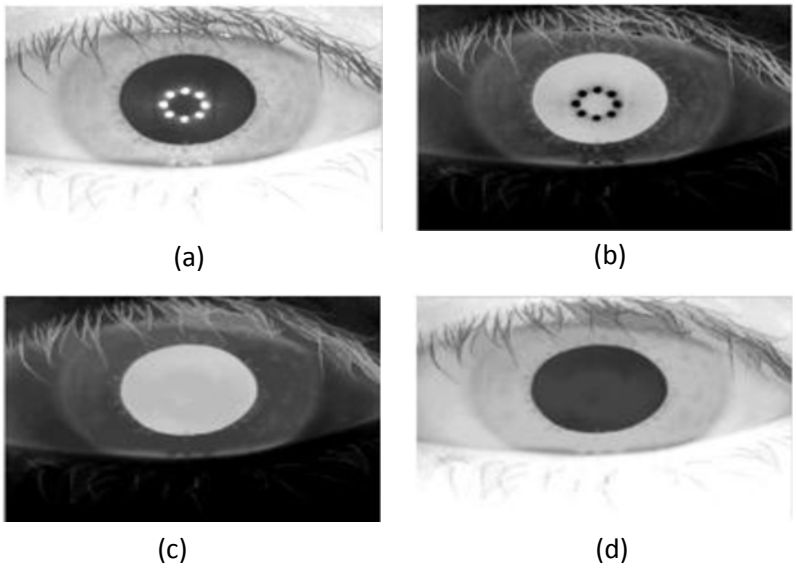

Figure 3.3: Result of reflection removal from an iris image using the flood filling approach; (a) original iris image, (b) complemented iris image, (c) filled iris image (d) final result of the flood filling.

We propose a two-steps approach to reflections detection and removal which aims to fill only the reflection points while the unaffected areas of the image are unaltered. In the first step, an adaptive threshold approach is employed to detect the areas of highest intensity in the image using the average intensity (brightness) of the image. Then, a multilevel edge detection method using adaptive high-pass edge weighted filter is employed to detect closed contours in the areas of highest intensities which represent the reflection points. In the second step, a modified exemplar based image in-painting method is employed for filling the reflection points. This method is superior to other methods in

terms of speed, accuracy and ability to retain the original structure of the unaffected parts of the image. Figure 3.4, illustrates the process of reflection detection and removal.

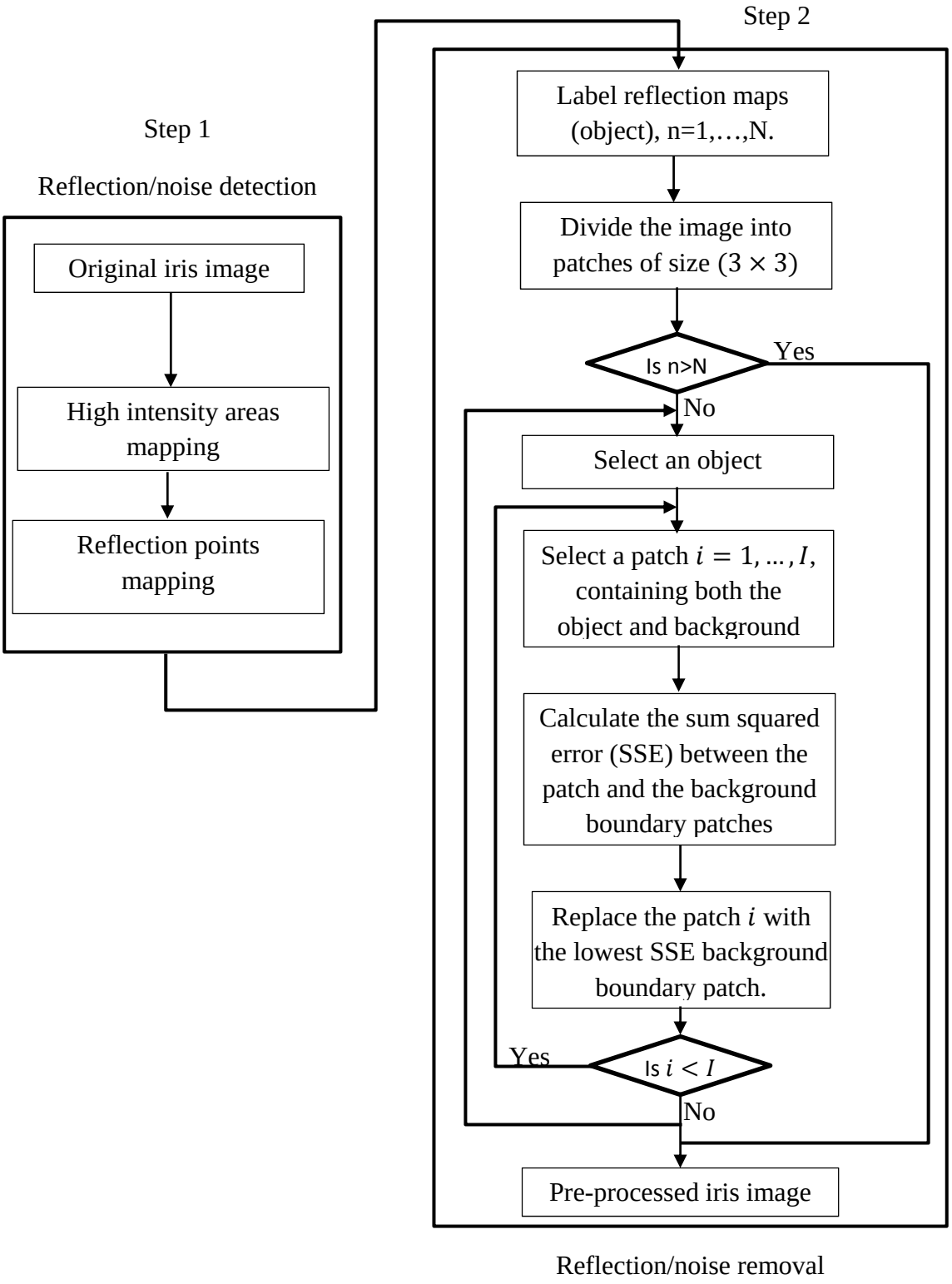

Figure 3.4: The block diagram of the reflection/noise detection and removal process: closed contour representing reflections are detected after filtering in the first step while the second step uses an exemplar based image inpainting method to fill the detected points.

The method proves to be very effective at enhancing the image while preserving the original structure for further processing. Also, because of the restriction of the algorithm to the boundary of the fill region, the algorithm proves to be also very fast.

3.3.1 Reflection Detection and Mapping

Usually, specular reflection appear as the brightest points surrounded by large gradient values in iris image [33], [34]. According to Kong and Zhang [33], strong reflection areas can easily be detected by deploying a simple threshold approach. However, calculating ideal threshold for detecting both weak and strong reflections present in a heterogeneous image like iris is a trivial task.

In our approach, we try to compensate for the variations in luminance of the iris images by using adaptive thresholding. The image brightness is first computed and a threshold is determining based on the image brightness. The threshold process is used to detect the high intensity areas of the image instead of reflection points as proposed in [33]. In the next step, the reflection points are then detected within the high intensity regions by finding closed edges representing reflections within the region. This ensures that both weak and strong reflections are detected.

Given the iris image $I(x, y)$, where (x, y) denote the location of a pixel, the regions of highest intensities can be detected by the following inequality expression [26]:

$$I(x, y) > \beta_s \qquad (3.1)$$

Where $I(x, y)$ denotes the intensity of the image and β_s is the brightness of the image which is given as:

$$\beta_s = \frac{\sum_{i=1}^{N} I(x, y)}{N} \qquad (3.2)$$

Where, N denotes the total number of pixels in the image calculated by multiplying the row size by the column size. Figure 3.5(b) shows the result of fixed thresholding method on the iris image using the 5% brightest intensity as the threshold. Figure 3.5(c) is the result of our adaptive thresholding method based on the brightness of the image.

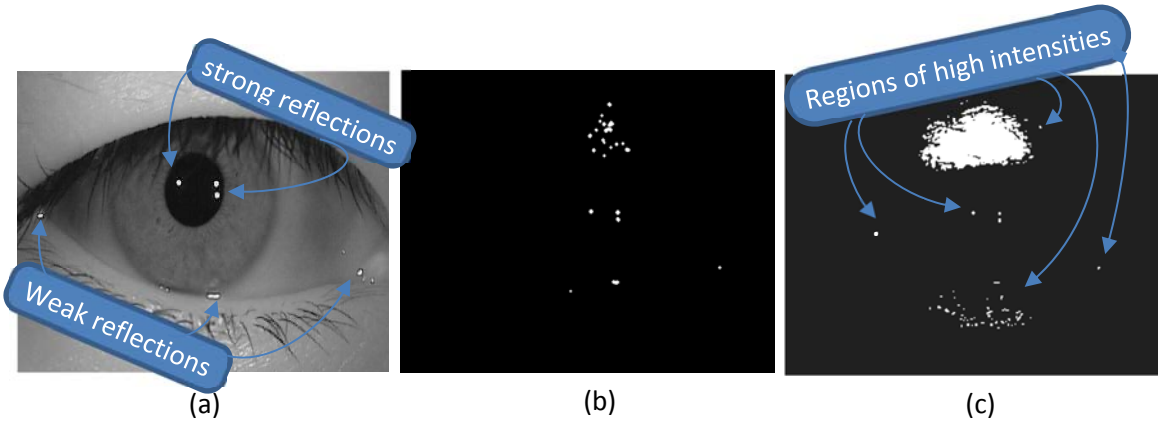

Figure 3.5: Results of thresholding the iris image using different approaches: (a) original iris image, (b) Fixed threshold using 5% brightest pixel intensity, (c) adaptive threshold using image brightness.

It can be noted from Figures 3.5(b) and (c) that the fixed threshold method using 5% brightest intensities of the image failed to detect a weak reflection on the left side near the medial canthus of the iris image marked with a circle but the adaptive threshold method using Equations (3.1) and (3.2) was able to detect it. Although it can be seen from Figure 3.5(c) that areas of hue saturation was largely detected, this is refined in subsequent steps and the actual reflection points mapped.

Once the areas of highest intensity have been marked out as shown in Figure 3.5(c), a multi-scale edge-weighted high-pass filter is employed to detect closed contours (edges) which represent the reflection point boundaries. The closed contours are mapped as reflection points representing the boundaries of reflection in the iris image as shown in Figure 3.6(b).

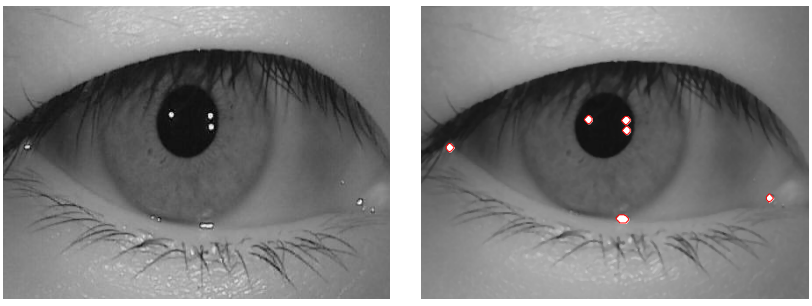

Figure 3.6: Reflection maps on iris image; (a) original iris image, (b) iris image with reflection maps

Experiments based on image intensity histograms carried out on the datasets in both CASIA and UBIRIS databases indicates that the intensity values of reflections in iris images are normally greater than the image brightness value. Areas of highest intensities normally include the reflection points and parts of the eyelids areas affected by hue

saturation (see Figure 3.5c). To detect edges within the marked high intensity regions, a multi-scale edge weighted highpass filter is applied to the image. Edges that form closed contours represent reflections and are marked with reflection maps as shown in Figure 3.6b.

The iris image is now filtered using the adaptive multi-scale edge weighted highpass filter in order to detect the varying edges representing the reflection boundaries. A high-pass filtered iris image can be represented as:

$$f(x,y) = |\mathcal{E}f(x,y)|^p Hf(x,y) \qquad (3.3)$$

Where $|\mathcal{E}f|^p$ is the image formed by raising every point $Lf(x,y)$ in the image $\mathcal{E}f$ to the p-th power. The image $|\mathcal{E}f|^p$ weights the highpass filtered image Hf pointwise according to the strength of the local edges $\mathcal{E}$. Further details on highpass filtering can be found in [117]. The smoothed image $f(x,y)$ is now decomposed by applying a discrete wavelet transform (DWT). At scale 2^j, three detail images are obtained $W_{2^j}^h$, $W_{2^j}^v$ and $W_{2^j}^d$ and an approximation image A_{2^j}. The superscripts h, v, and d represent horizontal, vertical and diagonal detail coefficients, respectively. Edges in the candidate reflection areas are characterized at each scale 2^j by computing the local maxima of the detailed coefficients which is given as [110]:

$$D_{2^j}f(x,y) = \sqrt{\left|W_{2^j}^h f(x,y)\right|^2 + \left|W_{2^j}^v f(x,y)\right|^2 + \left|W_{2^j}^d f(x,y)\right|^2} \qquad (3.4)$$

An edge-weighted highpass filtered image is computed by pointwise manipulation of highpass filtered image Hf with $\left|D_{2^j}f\right|^p$ which produces a P + 1st-order weighted highpass filters tuned to edges at scale 2^j. The multiscale analysis produces a set of edge-weighted highpass filters, each tuned to edges at prescribed scale. Therefore the reflection map $R(x,y)$ can be given as,

$$R(x,y) = \sum_{p=1}^{P}\sum_{j=1}^{J}\left|D_{2^j}f\right|^p Hf \qquad (3.5)$$

Which represent the boundaries of the reflection points.

The reflection maps of the detected points are as shown in Figures 3.7b and 3.7c, which illustrates the boundaries of the reflection points. Once the reflection points are detected, further processing is carried out to remove the reflections.

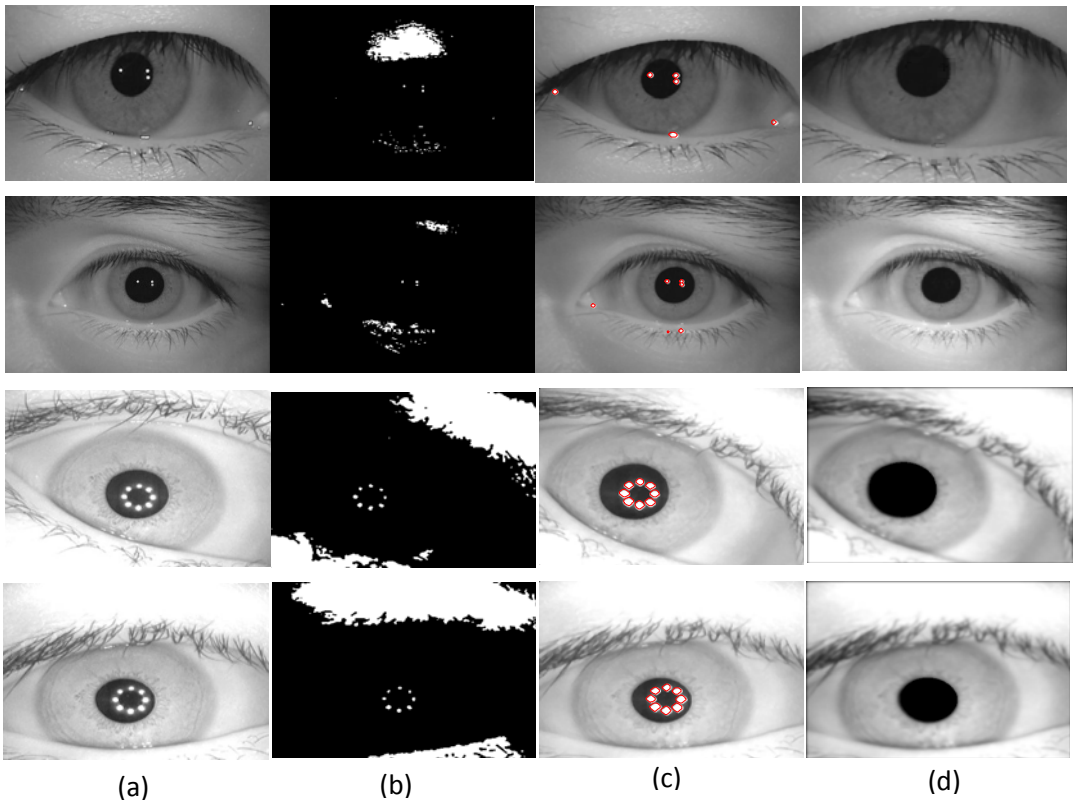

Figure 3.7: Iris images showing reflection detection and removal using the proposed algorithm; columns (a) Original iris images, (b) Thresholded iris images, (c) Iris images with reflection maps, (d) Iris images with reflections filled.

3.3.2 Reflection Removal

After reflection detection (mapping of the reflection points), a modified adaptive exemplar based image in-painting is applied to fill the reflection points. Exemplar based image in-painting [107], [108], have been widely used in vision computing for restoring natural images with some defects. Exemplar based image in-painting seeks to fill the areas of defects considered as “holes” in an image by searching for the best exemplar (similar) information from the non-defect region and simply copying it to the defected region. There exists some setbacks to this method which include erroneous reconstruction of edges and a global search for best exemplar which is time consuming. We modify this model to better adapt to edges and limit the search area to the boundaries of the holes

(reflection points) in order to improve speed. Full details of exemplar based image in-painting can be found in [107].

Now, Given the original image $I(x, y)$ with mapped reflection points, let's denote a reflection point as Ω while the boundary of the reflection point (contour) be denoted by $\delta\Omega$. For clarity, we refer to the reflections points as "holes" or "fill region" while the rest of the image is referred to as the "target region". The method in [107] is adopted in this work with some modification to enhance edge reconstruction and improve patch similarity computation.

In order to compute the similarity between the fill region and the target region, a patch of the image is selected at any one time. A patch given as ψ_i is a square sub-region of the image centered at pixel i. Generally, the size of ψ_i is decided to be slightly larger than the largest distinguishable texture element. The most common patch size of 9 x 9 is normally used for natural images but in this work a patch size of 3 × 3 is adopted which is more effective for highly textured images like the iris image. The fill patch given as ψ_p must contain a mixture of regions: part of the fill region (hole) and part of the target region. Whenever a patch of the fill region ψ_{pi} is selected, a search is conducted through the target region. When N-most similar patch is found, the ψ_{pi} patch is linearly combined with the target patch ψ_{qi} to predict the unknown region of ψ_p. In order to limit the search area to the reflection boundary, priority is given to the patches based on distance. The priority for the filling order $P(p)$ is based on the product of two terms, $C(p)$ confidence term and $D(p)$ data term and is given as [107]:

$$P(p) = C(p) * D(p) \quad (3.6)$$

Where

$$C(p) = \frac{\sum_{q \in \psi_p \cap \bar{\Omega}} C(q)}{|\psi_p|}, \qquad D(p) = \frac{|\nabla I^{\perp}_{p} \cdot n_p|}{\alpha}$$

and $|\psi_p|$ is the area of ψ_p, and α is a normalization factor (which is $\alpha = 255$ for the grayscale iris image), and n_p is a unit vector orthogonal to the boundary $\delta\Omega$ of the point p. In order to improve edge reconstruction, the data term is optimized in a non-linear fashion by modifying Equation (3.6) as shown in Equation (3.7).

$$\hat{P}(p) = C(p) * \exp\left(\frac{D(p)}{2\sigma^2}\right) \quad (3.7)$$

The squared exponential of the data tern $D(p)$ increases the influence of the data term on Equation (3.7) thereby increasing the match between ψ_p and ψ_{qi} closer to the boundary. The selection of the patch ψ_{qi} from K-similar patches is achieved by minimizing the sum of squared distance SSD which is given as

$$\psi_{qi} = \arg\min_{\psi_{q\in\bar{\Omega}}} d_{SSD}\left(P\psi_p, P\psi_q\right) \quad (3.8)$$

Where d_{SSD} is the SSD distance, while the $\{P\}$ extracts the known region from the patch ψ_p (known or already filled pixels). The results of the filling method is as shown in Figure 3.7(d).

3.4 Iris Boundaries Segmentation

In this section, we present the iris boundary segmentation model using a graph cut based active contour (GCBAC) model. The algorithm adopts a 2-level 2-step hierarchical approach which performs pupil segmentation first before the limbic boundary segmentation. Each level of the segmentation process is performed in two steps with initial boundary approximation performed first before the final boundary segmentation. This type of approach is aimed at tracking and handling any error which may arise at any level to make sure it is resolved at that level and not carried over to the subsequent levels and cause failure of the whole algorithm. Figure 3.8, shows the block diagram of the iris boundaries segmentation process. In the first hierarchical level of the segmentation process which is the segmentation of the pupil boundary, the first step of the algorithm starts by roughly approximating the pupil's boundary using a method based on circular Hough transform. Then, the final boundary of the pupil is segmented by refining the initial approximate contour based on the proposed GCBAC model. After pupil boundary segmentation, the same process is repeated again to segment the iris limbic boundary except that the initial approximation of the limbic boundary is carried out using an energy based method. The rough estimation of the limbic boundary is achieve using a modified energy based starburst algorithm. The first step of the iris segmentation process is a prerequisite for contour initialization. The main aim is to initialize the active contour close enough to the actual boundary of the pupil or iris in order to enhance segmentation accuracy and reduce computational time.

The model benefits from high accuracy and reduced processing time by initializing the active contour close enough to the actual boundary. The model showed improved performance compared to other methods that evolve the contour from the pupil boundary to the iris boundary.

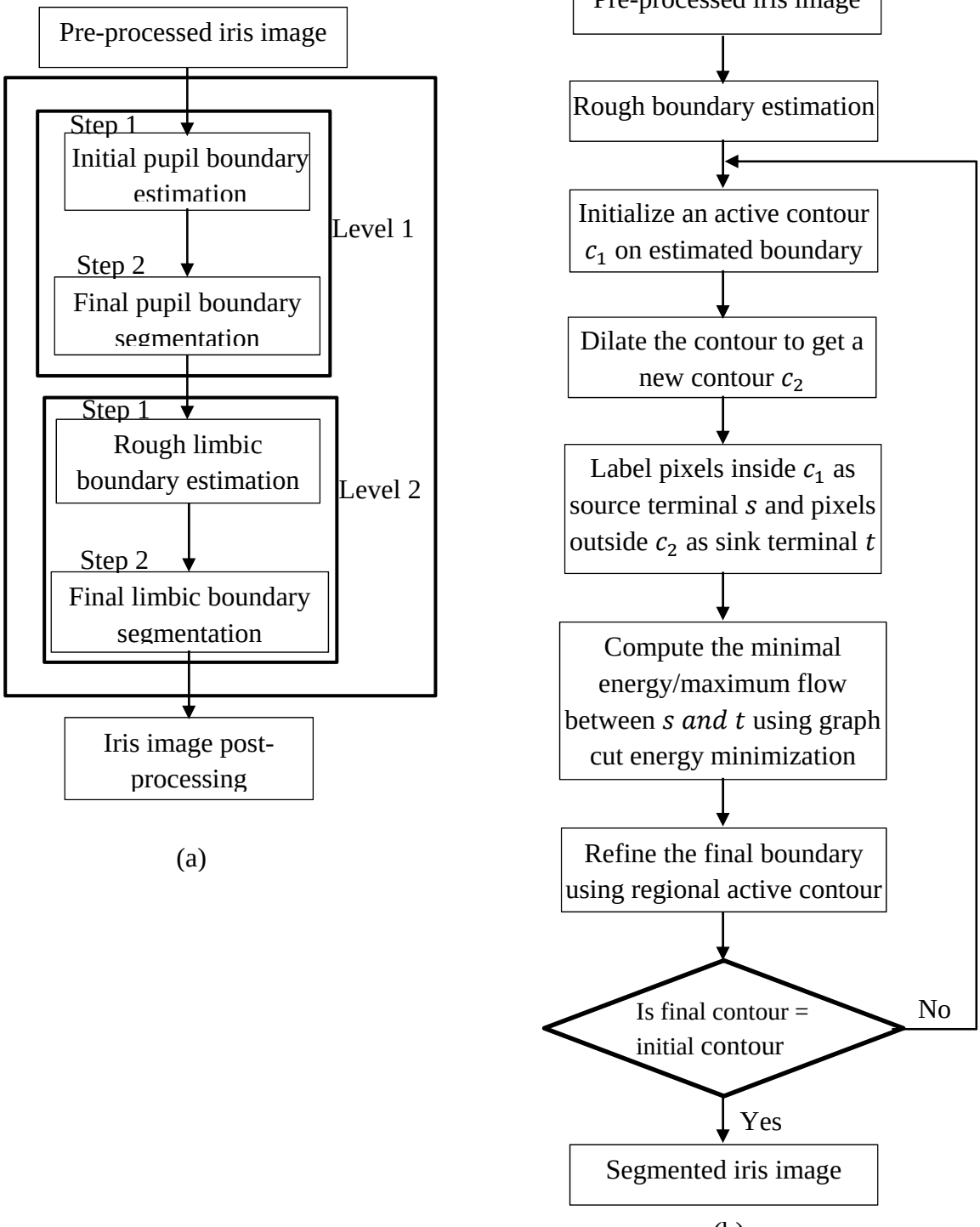

Figure 3.8: Block diagram illustrating the 2-level hierarchical segmentation approach for the iris inner and outer boundaries of the iris. (a) The 2-level hierarchical pupil and limbic boundary segmentation process. (b) Detailed block diagram showing the segmentation process at each step.

3.4.1 Estimation of the Approximate Pupil Boundary

The pupil is the darkest portion of the eye image which is surrounded by the relatively lighter coloured iris. Consequently, there exists a large contrast between the dark pupil and the surrounding iris portion in most iris images. The pupil can sometime be partially eclipsed by occlusions from the eyelids/eyelashes. Also, as a result of the reflective properties of the cornea and the infrared IR source lights normally used to capture the iris image, the pupil and its surrounding can be affected by specular reflections. In order to effectively approximate the pupil's boundary, the pre-processed iris image is now complimented and convolved with a smoothing filter. Then, a circular Hough transform is employed to search for and detect circles within the pre-processed iris image. The detected circles are called candidate pupils C_p. An evaluation scheme is developed to find the candidate pupil C_{pi} which corresponds to the actual pupil based on established properties of the pupil. The final segmentation of the pupil's boundary is subsequently achieved by refining the resulting initial contour of the pupil using the proposed graph-cut based active contour (GCBAC) model detailed in section 3.4.3.

A Hough transform is essentially a shape detector, which has been widely used to detect straight lines and circles in edge images [12]. The greatest advantage of Hough Transform is that it can be successful even when the shape to be detected is partially hidden. In this context, the pupil's shape is usually close to a circle but can sometime be partially hidden by the eyelids/eyelashes. This makes Hough Transform an attractive method for estimating the boundary and position of the pupil.

The circular Hough transform search of the iris image normally produce many candidate pupils as shown in Figure 3.9(c). These candidate pupils includes the actual pupil and many fake pupil candidates normally emanating from the eyelash region. In order to select the actual pupil from the candidate pupils and also, eliminate the chances of choosing a 'fake pupil', we make some assumptions based on some distinct features of the pupil.

1) The pupil is the darkest circular or near circular portion of the iris image located closest to the centre of the image.
2) The actual pupil candidate is the candidate with the smoothest intensity variations.

These assumptions are based on a pre-processed iris image where specular reflections have been removed. Based on these assumptions, we perform a rough

segmentation of the pupil using a method similar to the one in [27]. The whole image is searched for circles using circular Hough transform and the circle with the shortest distance to the centre of the image is selected as the pupil. Figure 3.9(c) shows some sample iris images with many detected candidate pupil circles. The blue marker shown on the images of Figure 3.9(c) indicates the centre of the iris image while the red asterisk markers show the centre of the candidate pupil circles.

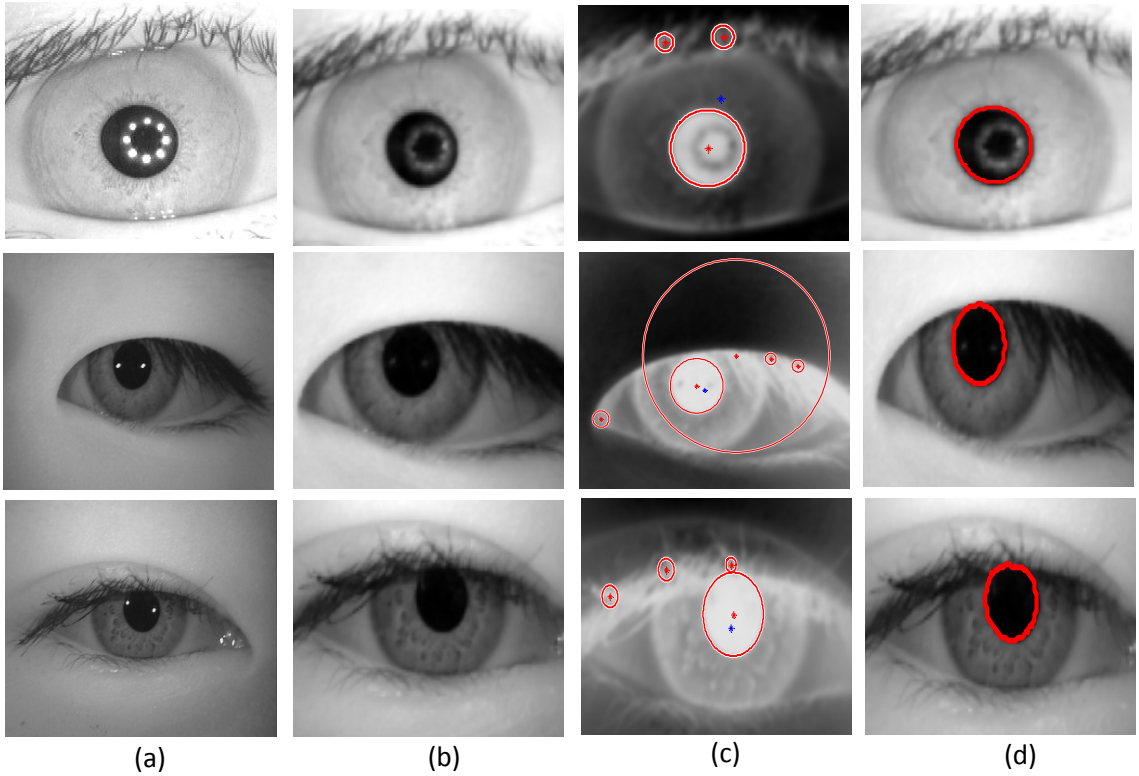

Figure 3.9: Iris images showing the approximate pupil's boundary estimation process; (a) original iris image, (b) pre-processed iris image, (c) complement of the iris image showing the pupil candidates, (d) segmented pupil.

The image is first complemented before convolving it with a square matrix of size $(n \times n)$ of all ones to reduce noise. Circular Hough Transform is then applied to search for candidate pupils C_p in the image. The Euclidian distances of all the C_p from the centre of the image are then computed. The $C_p$with the lowest Euclidean distance to the image centre is then chosen as the pupil.

Considering some non-ideal iris images, the rotation of the eye can cause the iris to be located nearer to the boundary of the iris image instead of image centre. Therefore, in order to compensate for such non-ideality and to avoid the error of selecting a 'fake pupil' candidate that is closer to the centre of the image as the pupil, we further refine the pupil candidates with an additional condition.

A measure of the entropy of the candidate pupils C_p can help to distinguish the real pupil candidate from the "fake pupils" candidates. In our investigation, detected fake pupil candidates normally lie within the dark eyelash region as shown in the images of Figure 3.9(c). These fake candidates normally present higher entropy values (higher intensity variation) compared to the real pupil candidate.

Now, the adjusted intensity values I^{C_p} of the pupil candidates C_{pi} are calculated by convolving the intensity values of the image with a square matrix of size (5×5) of all ones in order to smoothen the image and reduce noise. Hough transform is employed to detect the pupil's candidates within the image. The actual pupil candidate is selected based on their distances from the image centre and the intensity variation (entropy) within the candidate pupil circle. This can be stated mathematically as follows:

$$I^{C_p}(x,y) = \frac{I'_{x,y}}{1 + 3d^2_{(x,y)}} + H \qquad (3.9)$$

Where d^2 represents the Euclidean distance measure between a pupil candidate and the centre of the image. H is a measure of dispersion inside a candidate pupil C_p computed using Shannon entropy which is defined as

$$H = \sum_{i=1}^{m} P_i log \frac{1}{P_i} = -\sum_{i=1}^{m} p_i log P_i \qquad (3.10)$$

I' is the adjusted intensity value which is given as

$$I' = (255 - I) * 1_{n \times n} \qquad (3.11)$$

The value of n is selected based on the 5% of the image resolution. $I'_{x,y}$ is the intensity of the image within a candidate at location (x, y). The candidate with the highest adjusted intensity is selected as the true pupil candidate. The result of the procedure is as shown in Figure 3.9(d). The Hough's Transform returns three parameters (x_0, y_0, r): representing the coordinates of the pupil centre x_0 and y_0 and the radius r. These three parameters are used to initialize a contour close enough to the pupil's boundary in the next phase of the segmentation approach.

3.4.2 Approximate Iris Boundary Estimation

To approximate the iris limbic boundary, we employ a modified starburst algorithm. Starburst algorithm has been successfully used for the processing of low quality images and in eye tracking technologies. The starburst method provides a rough estimation of iris limbic boundary for contour initialization. Figure 3.10, shows the process of approximating the iris limbic boundary using the modified starburst algorithm. Finally, in the subsequent subsections, the iris and pupil boundaries were refined/segmented using the active contour based model described in sections 3.4.4, 3.4.4.1, 3.4.4.2.

Starburst is a randomized local search algorithm which has since been used to model eye tracking technologies [49], [109]. Starburst was first proposed by Li et al. [109] to compensate for the high degree of noise present in low cost off-the-shelf camera images. The original starburst algorithm proved to be a stable way of tracking the eye under NIR illumination. Although the starburst algorithm have been quite successful for eye tracking purposes, they do have some inherent setbacks when applied to iris boundary estimation which include: difficulty in distinguishing between features of the pupil and the limbus boundaries, erroneous feature points generated by specular reflections that can cause the algorithm to fail, and the eyelashes and eyelids which can introduced noisy feature points that are able to influence the result of the algorithm.

Recall that in our earlier pre-processing step of section 3.3, possible specular reflections that might exist in the original iris image have been detected and eliminated. This presents us with a better quality iris image for further processing. Also, the difficulty in distinguishing between the pupil and limbus boundaries feature points can be simplified by the hierarchical segmentation framework adopted in this work. In the first phase of the hierarchy, the pupil is segmented and the information obtained from the pupil segmentation helps to identify and eliminate the feature points belonging to the pupil in the next phase which is the limbic boundary segmentation.

Our adaptation of starburst algorithm, shown in Figure 3.10, requires the determination of a proper initialization point in the image. This initialization point of the starburst algorithm is chosen to the centre of the pupil whose coordinates has been determined in Section 3.4.1. Rays from the centre of the pupil are projected away in a star-like fashion towards the boundary of the image. The gradient change is computed along each ray which is used to identify feature points at the points of highest intensity changes. Two highest feature points along each ray are retained and the rest are discarded.

In order to reduce the effects of eyelash which mostly occlude the upper region of the iris, a steerable filter is applied to the image before implementing the starburst algorithm computation. The two feature points retained represents the iris boundary and a possible eyelid/eyelash edges. To discard the non-boundary feature points, a distance measure as well as an energy based method is employed to distinguish between the noisy feature points belonging to the possible eyelash and the limbic boundary feature point. Later, the remaining feature points are then interpolated using B-spline cubic interpolation to form a closed contour.

To detect feature points on the rays, a dot product is used to calculate the components of the gradient collinear with rays pointing radially away from the originating point. In each ray, the two feature points are marked at the points of highest gradient change within an experimentally determined epsilon distance. Feature points that fall on the pupil boundary are first eliminated before selecting the two highest feature points.

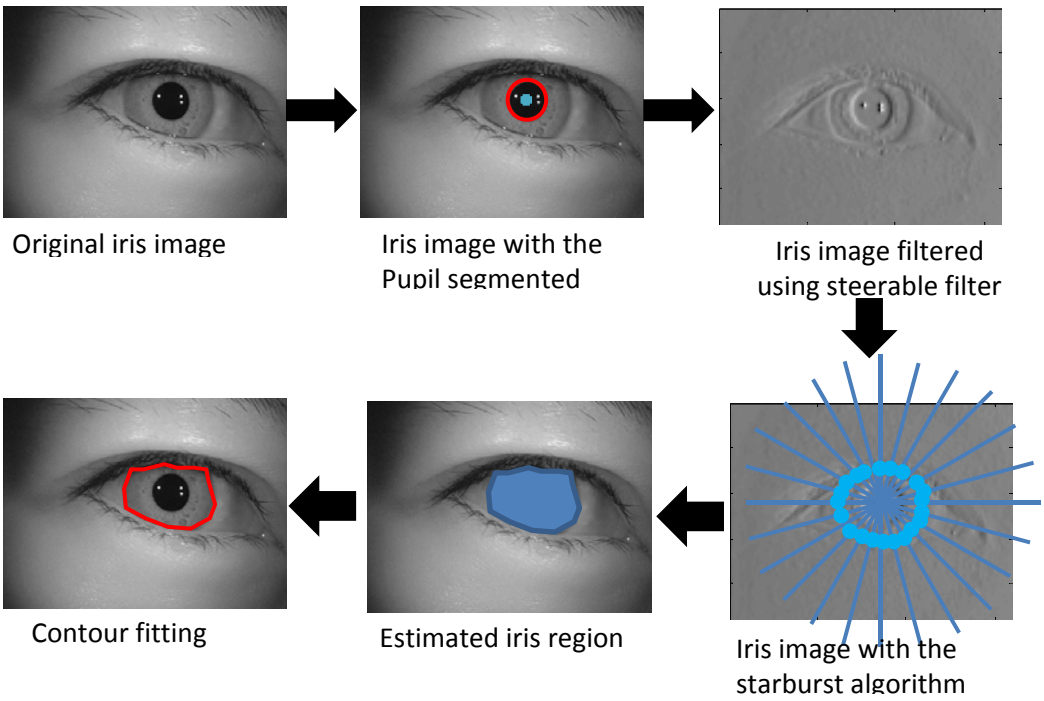

Figure 3.10: Iris boundary approximation process using the modified starburst algorithm.

In order to select the two feature points with highest intensity change, a ranking system is introduced to classify each of the feature points based on their energy and distance from the centre point. The ranks indicate which of the feature points fits more to the iris boundary and which is considered as noise. A rank of 1 is given to the feature points with high energy and closer to the origin of the ray, while a rank of 2 is given to feature points further away from the origin of the rays with lower energy. Surviving

feature points are classified into two categories: iris, and junk. The junks are discarded while the iris feature points are then interpolated using B-spline interpolation to form a closed contour. The contour is then used for the initialization of the GCBAC model in section 3.4.4.

3.4.3 The Proposed Graph-Cut Based Active Contour (GCBAC) Model

In this section, a graph cut based active contour model (GCBAC) model is proposed for the final refinement/segmentation of the iris boundaries. Accurate extraction of iris boundaries is an important issue which have been widely investigated in the field of computer vision and image processing. The extraction of accurate and optimal boundaries of the iris has great challenges which include: occlusions of the boundaries, noise and other artefacts in the image. The problem of extracting an optimal iris boundary can be naturally formulated as an energy minimization problem. However, it is very difficult to define a cost function that can solve for the global optimal result, and even if a cost function is defined, the minimization problem is still difficult to solve. The GCBAC model presented here is a combination of the idea of iterative deformation of active contour and the global optimization properties of graph cut.

This approach is different from the traditional active contours because, it uses graph cut energy to iteratively deform the contour and its cost function is defined as a summation of edge weights on the graph. This implies that the resulting contour at each iteration is the global optimum within the contour neighbourhood (CN). The adoption of CN is used to overcome graph cut's well-known shortcoming of biasness to shorter boundaries [93-102]. Also, the combination of the two approaches (graph cut and active contour) is able to overcome another well-known shortcoming of active contour model of yielding to local maxima. Nevertheless, the proposed model still retains the graph cut's advantages as a global optimization tool and computation within a polynomial time. Also, as a result of its global optimization properties of GCBAC, the model is able to segment irregular boundaries and easily overcome the problem of noise and outliers in the iris image. This ensures that the proposed scheme is able to overcome the level-set's greatest disadvantage of slow convergence and the potential of getting stuck at local maxima while maintaining the advantage of active contour deformation to trace irregular boundaries.

Several methods have been proposed for segmentation of the iris portion from the original eye image [11-13], [19-58]. However, most of these methods are solely based on boundary or regional information which is highly limited. Graph cut method utilizes both boundary and regional information for the segmentation of image which is highly advantageous. The combination of regional and boundary information enables graph cut to find optimal boundary and overcome the problem of outlier and noise in the image. Graph cut establishes an objective energy function which reaches a minimum value at the object's boundary.

Now, let c_1 denote an initial curve representing the approximate pupil or limbic boundary of the iris as obtained from sections 3.4.1 and 3.4.2, respectively. Also, let c_2 represent a new contour obtained by dilating the initial contour to its surrounding neighbourhood area as shown in Figure 3.11(b). Given the pre-processed eye image $I(x, y)$ with d_1 and d_2 representing the pixels inside c_1 and outside c_2, respectively as shown in Figure 3.11. A graph $G = (V, E)$ is established with a set of vertices V, and a set of edges E as shown in Figure 3.11. The vertices or nodes of the graph is a set of terminals (pixels) $V = \{v_1, v_2, \ldots\ldots, v_n, s, t\}$ with two special terminals called the source s and the sink t. Figure 3.11(c) shows the structure of a graph with its terminals and their links. The edges (links) corresponds to a set of connections between vertices $E = \{u, v\}$. There are two types of links which include: the $t-links$ and $n-links$. The $t-links$ include edges which connect the terminal nodes to the neighbouring nodes while, the $n-links$ are the links that connect the neighbouring pixels together. The edges in the graph are assigned with a non-negative measurements of the similarity between neighbouring pixels p and q called edge weights $\omega(i, j)$. The edge weights which is also known as cost are obtained from the measurement between neighbouring pixels. A cut is a subset of edges which is denoted as C and expressed as sum of edges with maximum cost representing areas of highest dissimilarity in the image. The pixels inside c_1 and outside c_2 the contour D, represents the two special terminal nodes (seeds) called the source s and the sink t.

In the works of Boykov and Kolmogorov [96], the computation of minimal surfaces or geodesics with placement of markers was studied. Two seeds was specified and their method automatically finds the optimal curve (or surface) separating the two sets of seeds by computing the minimal energy between them. Graph cut tries to find the maximal flow of energy from node s, to node t, which is equivalent to computing the

minimal cut on the graph G [95], [97], [98-102]. A cut $c(S,T)$ is given by a pair of complementary subsets of nodes (S,T) where $s \in S$ and $t \in T$. Image segmentation can be regarded as a pixel labelling problem where the label for the object can be set to 1 while that of the background can be set to 0.

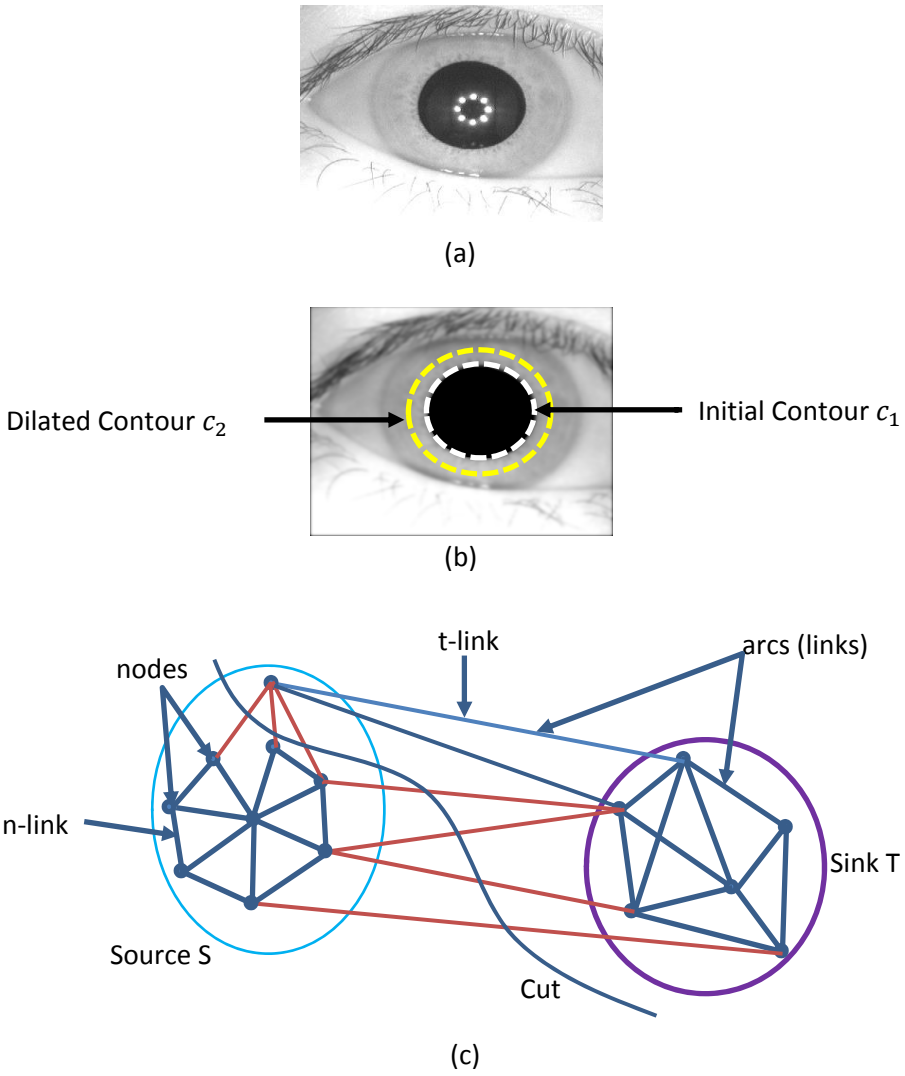

Figure 3.11: An illustrated diagram of the graph cut segmentation process. (a) Original iris image, (b) pre-processed iris image with initialized contours (c) graph cut segmentation diagram showing the source and sink and connections.

The segmentation process can be achieved through the minimization of an energy function called graph energy. So, let the label $L = \{l_1, l_2, l_3, \dots, l_i, \dots l_p\}$, where p is the number of pixels in the iris image and $l_i \in \{0,1\}$. The set L contains two labels $\{0,1\}$, where the pixels labelled 1 belongs to the object while the pixels labelled 0 belongs to the background. The energy function can be defined according to Equation (12), which can be minimized using the max-flow/min-cut in the $s-t$ graph [98].

$$E(\psi) = E_B(\psi) + \varphi E_R(\psi), \qquad (12)$$

E_B is the boundary energy term which incorporates the boundary constraint into the segmentation process while, E_R is the regional energy term representing the regional image energy information in the segmentation process. The boundary term is used to penalize dissimilar neighbours in the graph cut equation, while the regional term penalizes pixel labels based on local properties of the negative log-likelihood of the image intensities. Also, φ is a regularization term between the regional and the boundary information which weights the importance of each in the equation. When φ is set to 0, the regional information is ignored and only the boundary information is considered. The regional energy term can be defined as [99-101]:

$$E_R = \sum_{p \in P} R_p(L_p), \qquad (13)$$

Where $R_p(l_p)$ is the penalty for assigning the label l_p to the pixel p. The weight of $R_p(l_p)$ is obtained by comparing the intensity of the pixel p with the given intensity histogram of the object and background. The weights of the $t - links$ is defined as follows:

$$E_p(1) = -lnPr(\left(I_p\middle|'Object'\right), \qquad (14)$$

$$E_p(0) = -lnPr(\left(I_p\middle|'bkground'\right), \qquad (15)$$

Therefore, when the probability of the object $Pr(\left(I_p\middle|'Object'\right)$ is larger than that of the background $Pr(\left(I_p\middle|'bkground'\right)$, $E_p(1)$ will be smaller that $E_p(0)$. This indicates that the pixel is more likely to belong to the object rather than the background and the penalty for grouping the pixel into object is much smaller than that of grouping it to background. Thus the regional term is fully minimized when all of the pixels have been correctly separated into two subsets. Similarly, the boundary term $B_{<p,q>}$, is defined by the increasing function of $\left|l_p, l_q\right|$ as follows [101]:

$$B_{<p,q>}\, \alpha \exp\left(-\frac{\left(I_p - I_q\right)^2}{2\sigma^2} \cdot \frac{1}{dist(p,q)}\right), \qquad (16)$$

Where I_p and I_q represents neighbouring pixels and σ denotes the camera noise. This indicates that when the intensity difference between the two neighbouring pixels is small, the penalty is high, otherwise it is low. Therefore, the energy function is more

likely to reach a minimum value at the boundary of the object rather than at any other point. In Boykov and Jolly [95], it was shown that the minimized energy of the graph can be computed by a min-cut through max-flow energy on the image. Thus, the minimum energy problem can be converted to the graph cut problem. In order to get a reasonable segmentation result, the assignment of the weight in the $s-t$ graph is very important. Table 3.2, shows the assignment of weight in the $s-t$ graph image.

Edge	Weight	Condition
$< p, q >$	$B_{<p,q>}$	$\{p, q\} \in N$
$\{P, S\}$	$\varphi . E_R(0)$	$p \in P\ (Uknown)$
	K	$p \in\ Object$
	0	$p \in Background$
$\{P, T\}$	$\varphi . E_R(1)$	$p \in P\ (Uknown)$
	0	$p \in\ Object$
	K	$p \in Background$

Table 3.1: The assignment of weights to the $s-t$ graph image.

From the table, it can be inferred that when the intensity of the pixel is inclined to the object, the weight of the pixel and the $s-node$ will be larger than the weight of the neighbouring pixel and the $t-node$. Therefore, the cut is more likely to occur at the edge with smaller weight and dissimilar intensity values. Also, for neighbouring pixels, when their intensity difference is smaller, the weight is bigger which is more likely to be separated by the cut. Thus the implementation of the graph cut can be fulfilled by the max-flow/min-cut as described in [95 -101].

A cut on the graph partitions the nodes of the graph into subset of edges such that the terminals becomes separated. In combinatorial optimization, it is always normal to define cost of a cut as the sum of edge weights (cost) of the edges that it severs. Therefore, as illustrated in Figure 3.11, the partitioning of the nodes corresponds to the segmentation of the underlying image. A minimum cut generates a segmentation that is optimal in terms of the properties that are built into the edge weights. Therefore, the cost of the min-cut on the graph can be defined as [95]:

$$Cut(S,T) = \sum_{i \in S} \sum_{j \in T} \omega(i,j), \qquad (3.17)$$

The minimal cut on the graph can be computed in polynomial time, which guarantees good speed. The GCBAC model tries to relate the cost of the cut on the graph to the length of an underlying curve as shown in Figure 3.13 (a).

Now, consider an image which is embedded in a discrete grid. The neighbourhood system N_g of the image can be of different forms as shown in Figure 3.12 (a-c). The edges of the neighbourhood system forms a family of lines in different directions [–, /, |, \ ] as shown in Figure 3.13 (a).

The cost of an (s,t) cut in the constructed graph is now equivalent to:

$$c(S,T) = \sum_{i \in S} \sum_{j \in T} c(i,j) = \sum_{k=1}^{N_g} \alpha_n(k)\omega_k, \qquad (3.18)$$

Where $\alpha_c(k)$ is the number of arcs or edges of the family of lines k that connects S to T, and ω_k is the weight of the arcs of family of lines k.

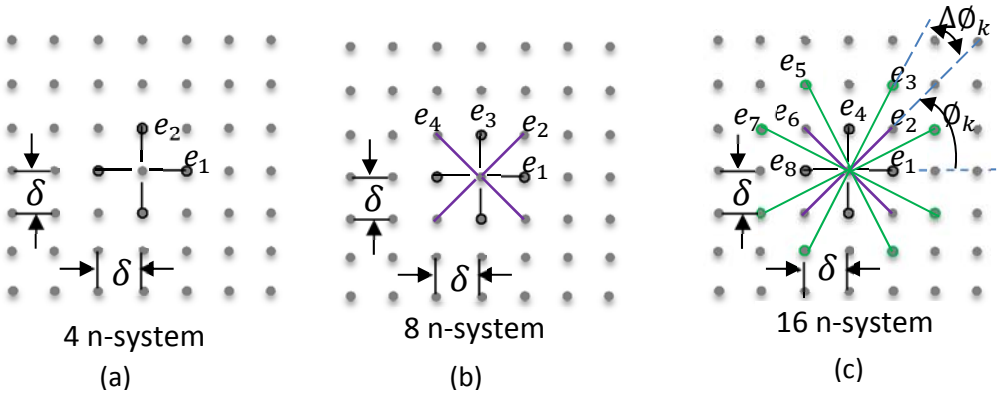

Figure 3.12: The graph neighbourhood system, (a) 4 neighbourhood system, (b) 8 neighbourhood system and (c) 16 neighbourhood system.

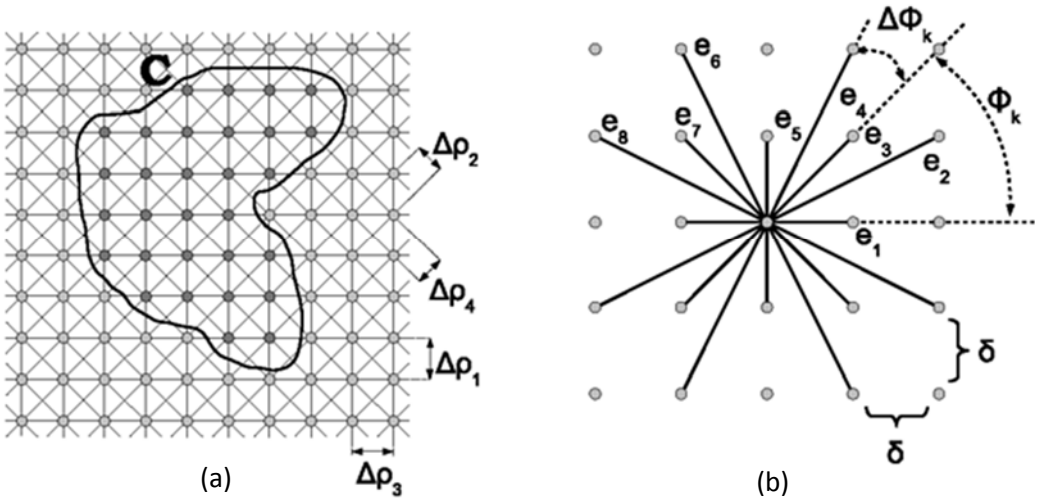

Figure 3.13: The 16-neighbourhood system, Cauchy-Crofton formula used to establish a link between a finite set of lines and the length of the curve C.

In order to relate the family of arcs or lines (as shown in Figure 3.9 (a)) formed using graph cut, with the continuous contour representing the boundary of the image, the Cauchy-Crofton formula is employed to relate the length of the curve C to a measure of a set of lines intersecting it. Let $L(\rho, \theta)$ be a straight line which is represented in the polar coordinates by the two parameters (ρ, θ). The Cauchy-Crofton formula which can be used to establish the Euclidean length of the curve is given as:

$$|C|_{\varepsilon} = \frac{1}{2}\int_{0}^{\pi}\int_{-\infty}^{\infty} N(\rho,\theta)dpd\theta, \qquad (3.19)$$

Where $N(\rho, \theta)$ is the number of lines $L(\rho, \theta)$ intersecting with the curve C, and C is a regular curve. The Cauchy-Crofton formula can be extended to Riemannian space, such that the length of the curve C according to the metric tensor D is given by:

$$|C|_{R} = \frac{1}{2}\int_{0}^{\pi}\int_{-\infty}^{\infty} \frac{detD}{2(u_L^T D_{uL})^{3/2}} N(\rho,\theta)dpd\theta, \qquad (3.20)$$

Where u_L is a unit vector in the direction of the line L.

Now, the neighbourhood system N_g on the discrete grid, can be defined by a finite set of undirected vectors e_k, where $N_g = \{e_k : 1 < k < n_g\}$. Each of the vectors e_k generates a family of lines as shown in Figure 3.12. The lines are made up of a family of lines which are separated by a common distance $\Delta\rho_k$. In each direction θ_k, there exist a family of parallel lines separated by a distance $\Delta\rho_k$ as shown in figure 3.13(a).

The approximation of the Euclidean length of the curve C can be obtained by the discretization of Equation (3.20), which is given as follows:

$$|C|_{\varepsilon} = \frac{1}{2}\sum_{k=1}^{n_g}(\sum_{i}\alpha_c(i,k)\Delta\rho_k)\Delta\theta_k = \sum_{k=1}^{n_g}\varphi_c(k)\frac{\delta^2\cdot\Delta\theta_k}{2|e_k|}, \qquad (3.21)$$

Where i is an index of the k^{th} family of lines, while $\alpha_c(i,k)$ is the count of the number of intersections of lines i of the k^{th} family of lines with the curve C. The total number of intersections of the k^{th} family of lines with the curve C can be given as $\alpha_c(k) = \sum_i \alpha_c(i,j)$.

In order to set the arc weights, the Cauchy-Crofton's formula given in Equation (3.19) is used. The arc weights are set such that the cost of the graph approximates the Euclidean length of the contour separating the two sets c_1 and c_2 as follows:

$$c(c_1,c_2) = \sum_{k=1}^{n_g} n_c(k)w_k \quad where\ w_k = \frac{\delta^2\Delta\theta_k}{2|e_k|}, \qquad (3.22)$$

This can be extended to the Riemannian metric using the following weights:

$$\omega_k(p) = \frac{\delta^2\cdot|e_k|^2\cdot\Delta\theta_k\cdot\det(D(p))}{2(e_k^T D(p)e_k)^{3/2}}, \qquad (3.23)$$

Where $\omega_k(p)$ is the weights of the arcs leaving the node p, while $D(p)$ is the local Riemannian metric at point p. This is able to show explicitly the relationship between the cost of graph cut and the geometric length of the contour separating the sets c_1 and c_2 which is defined by the cut.

The method we have described here is computationally expensive and it cannot be used iteratively on a large dataset. However, inspired by this approach, we propose a new method for fast and accurate computation of approximate geodesics and minimal surfaces based on the Chan-Vese active contour model.

3.4.3.1 The Modified Total Variation Normalization Approach

Active contour based on variational level-set method was introduced by Chan-Vese [86], [87]. The Chan-Vese model is a special case of Mumford-Shah functional for segmentation by level-sets. It is different from other active contour models in that it is not edge dependent which means that it is more capable of detecting objects whose boundaries are not gradient dependent. The region detection step was accomplished in sections 3.4.1 and 3.4.2, which provides a set of regions which is passed as an initialization to the GCBAC segmentation method. We exploit the efficiency and accuracy of a global optimal total variation segmentation approach to calculate the accurate boundary of each of the boundaries of the iris. This hybrid algorithm combines active contour with a graph cut's regional model to create an energy functional for iris segmentation. Instead of discretizing the Euler-Lagrange equations as shown earlier, we discretize the variation functional based on Chan-Vese model. The GCBAC model can now be formulated using binary level set function $\emptyset = \{\emptyset | \Omega \rightarrow \{0,1\}\}$, representing inside and outside the contour C. Where $\emptyset$ is a function representing the level-set functional of the iris image and Ω is a set of labels representing subsets of the image belonging to either foreground or background. Therefore, we derive a curve evolution solution for the min cut problem. The min cut problem originates from graph cut partitioning as shown in Equation 3.17. In continuous domain, the equivalent energy functional can be defined as follows [87]:

$$\min_{\emptyset, c_1, c_2} E_{CV}(\emptyset, c_1, c_2) = v \int_{\Omega} |\nabla \emptyset| dx + E^{data}(\emptyset) \qquad (3.24)$$

Where

$$E^{data}(\emptyset) = \int_{\Omega} \{\emptyset |c_2 - \mu^0|^{\beta} + (1 - \emptyset)|c_1 - \mu^0|^{\beta}\} dx \qquad (3.25)$$

The discretization of the Equation (3.24), is achieved by using the anisotropic variant of the total variation term. The anisotropic variant, using 1-norm is given as:

$$TV_1(\emptyset) = \int_{\Omega} |\nabla \emptyset|_1 dx = \int_{\Omega} |\emptyset_{x_1}| + |\emptyset_{x_2}| dx, \qquad (3.26)$$

Now, let $\rho = \{(i,j) \subset \mathbb{Z}^2\}$ denote the set of grid points. For each pixel $p = (i,j) \in \rho$, the neighbourhood system $N_p^k \subset \rho$ for four neighbourhood system is defined as

$$N_p^4 = \{(i \pm 1, j), (i, j \pm 1)\} \cap P, \qquad (3.27)$$

Where P denotes the all the neighbouring pixels of p.

Therefore, the discrete energy function of the GCBAC can be formulated as:

$$\min_{\emptyset, c_1, c_2} E_d = v \sum_{p \in \mathcal{P}} \sum_{q \in N_p^k} \omega_{pq} |\emptyset_p - \emptyset_q| + \sum_{p \in \mathcal{P}} E_p^{data}(\emptyset_p), \qquad (3.28)$$

Where

$$E_p^{data}(\emptyset_p) = \left\{ \emptyset_p |c_2 - \mu_p^0|^\beta + (1 - \emptyset_p) |c_1 - \mu_p^0|^\beta \right\}, \qquad (3.29)$$

The weights ω_{pq} is therefore given as:

$$\omega_{pq} = \frac{4\delta^2}{k\|p - q\|_2}, \qquad (3.30)$$

This is similar to the weights derived from the Cauchy-Crofton formula of integral geometry as shown in Equation (3.19).

The discretization problem of Equation (3.28) can be minimized globally using graph cut optimization. Graph cut is a well-known global optimization technique which is able to find global solution for a given set of boundary conditions. Due to the duality theorem provided by Ford and Fulkerson [69], there are now several fast algorithms for this kind of problem out there. It was introduced as a computer vision tool by Greig et al. [70], in connection with Markov random fields [63], and has later been studied by Kolmogorov et al. [62- 64]. It has been widely applied in many areas of computer vision including: stereo vision, segmentation [53], and noise removal and image restoration [55].

The discrete energy function E in Equation (3.28), is composed of pairwise interaction terms between binary variables which can be minimized using graph cuts. Therefore the graph representation of the total variation problem can be given as [96]:

$$\min_{\mathcal{V}_s, \mathcal{V}_t} c(\mathcal{V}_s, \mathcal{V}_t) = \min_{\emptyset} E_d(\emptyset, c_1, c_2) + \sum_{p \in \mathcal{P}} \sigma_p, \qquad (3.31)$$

Where $\sigma_p \in \mathbb{R}$ are fixed for each pixel $p \in \mathcal{P}$. The graph is constructed such that there is a one-to-one correspondence between cuts on G and the level set function $\emptyset$. The minimum cost cut will correspond to the level set function $\emptyset$ minimizing the energy in

Equation (3.28). In the graph, the two vertices are associated to each grid point $p \in \mathcal{P}$ which are denoted by $v_{p,1}$ and $v_{p,2}$ and corresponds to the set of pixels inside and outside the contour C. Hence the set of vertices is defined as

$$\mathcal{V} = \left\{ \left\{ v_{p,i} \middle| p \in \mathcal{P},\ \ i = 1,2 \right\} \cup \{s\} \cup \{t\} \right\} \qquad (3.32)$$

The edges are constructed such that the relationship in Equation (3.29) is satisfied. For each grid point $p \in \mathcal{P}$, the edges constituting the data term can be defined as:

$$\varepsilon_D(p) = (s, v_{p,1}) \cup (v_{p,1}, t) \cup (v_{p,2}, t) \cup (v_{p,1}, v_{p,2}) \cup (v_{p,2}, v_{p,1}), \qquad (3.33)$$

Where ε_D is the set of all data edges which is defined as $\cup_p \in p\varepsilon_D(p)$. Also, the edges corresponding to the regularization term is defined as

$$\varepsilon_R = \{(v_p, v_q), \forall p, q \subset \mathcal{P}\ s.t.\ q \in N_p\}, \qquad (3.34)$$

Weights are assigned to edges such that the relationship in Equation (3.34) is satisfied. The regularization edge weights are given as:

$$\omega(v_p, v_q) = \omega(v_q, v_p) = v\omega_{pq}, \qquad \forall\ p \in \mathcal{P}, q \in \mathcal{N}_p, \qquad (3.35)$$

And, the weights on the data edges ε_D for a grid point such as $p \in \mathcal{P}$ is given as:

$$A(p) = \omega(v_p, t),\ \ B(p) = \omega(s, v_p), \qquad (3.36)$$

Therefore, a cut $C(\mathcal{V}_s, \mathcal{V}_t)$, on the graph corresponding to the level set function can be defined as:

$$\emptyset_p = \begin{cases} 1 & if\ v_p \in \mathcal{V}_s \\ 0 & if\ v_p \in \mathcal{V}_t \end{cases}, \qquad (3.37)$$

3.4.4 Pupil/Iris Boundary Segmentation Using GCBAC

The GCBAC model presented in section 3.4.3.1, provides us with a method for computing the global optimal partition of iris boundaries in the eye image. This is achieved by first transforming the image into an edge capacitated graph $G(V, E, \omega)$ and then computing a minimum cut on the graph. Each pixel within the image is mapped to a vertex $v \in V$ and if two pixels are adjacent, there exist and undirected edge $(u, v) \in E$ between the corresponding vertices u and v. Edge weight is assigned according to a

measure of similarity between two pixels as shown in Table 3.1. A cut on the graph will partition the nodes into two subsets with minimum capacity where the summation of edge weights across the cut is minimized. Therefore, the corresponding contour on the graph will partition the image into two segments with the minimum between-segments-similarities. The contour that partitions the image into two subsets S and T corresponds to a cut $c(S,T)$ on the graph.

The GCBAC proposed in this work is a kind of narrow-band algorithm using the basic concept proposed by Boykov and jolly [92]. Given an initial contour as determined in sections 3.4.1 and 3.4.2, the algorithm iteratively searches for the closest contour and replaces the initial contour with a global minimum within the contour neighbourhood.

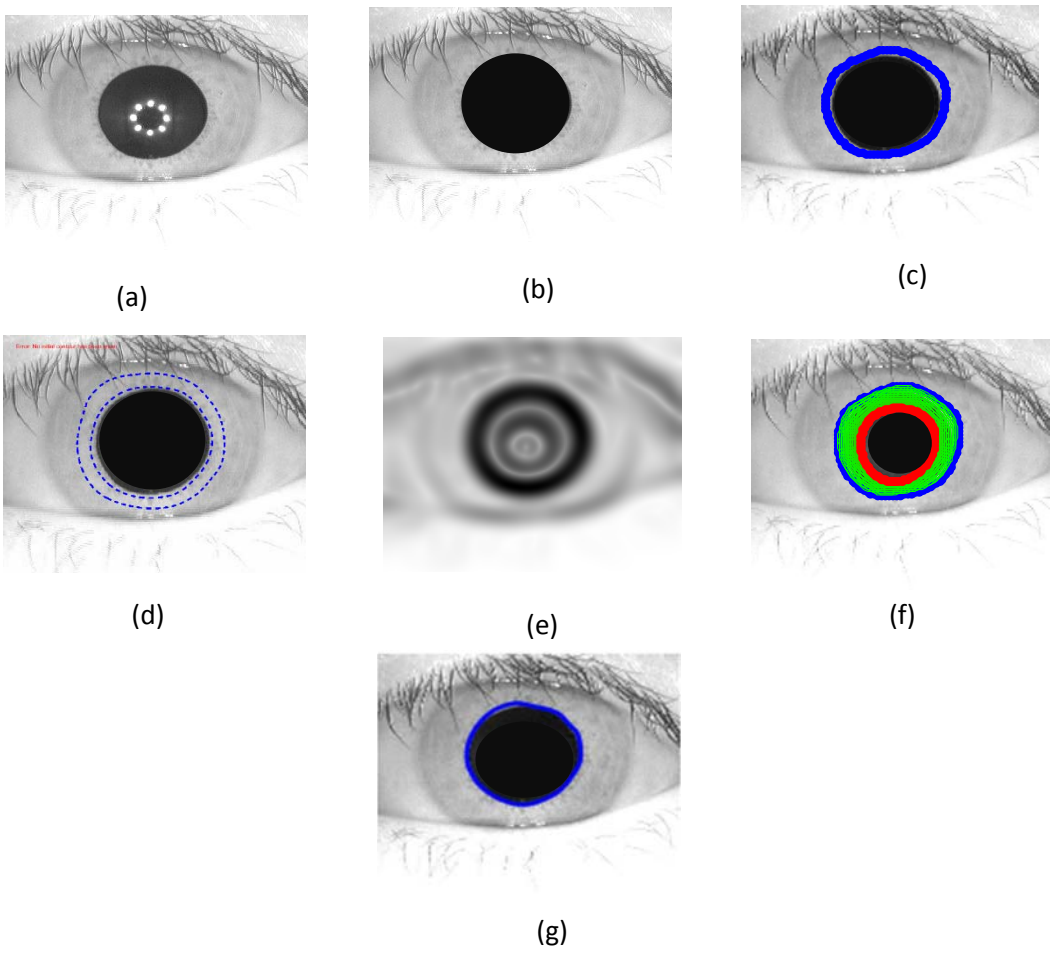

Figure 3.14: Sample iris image showing the GCBAC segmentation process for the pupil: (a) original iris image (b) pre-processed iris image (c) iris image showing initialized contour on the approx. pupil boundary, (d) iris image showing the initialized contour and the dilated contour (e) GCBAC energy image, (f) iris image showing the initial contour and the dilated contour with the pixels labelling process in-between, (f) final image showing the segmented pupil.

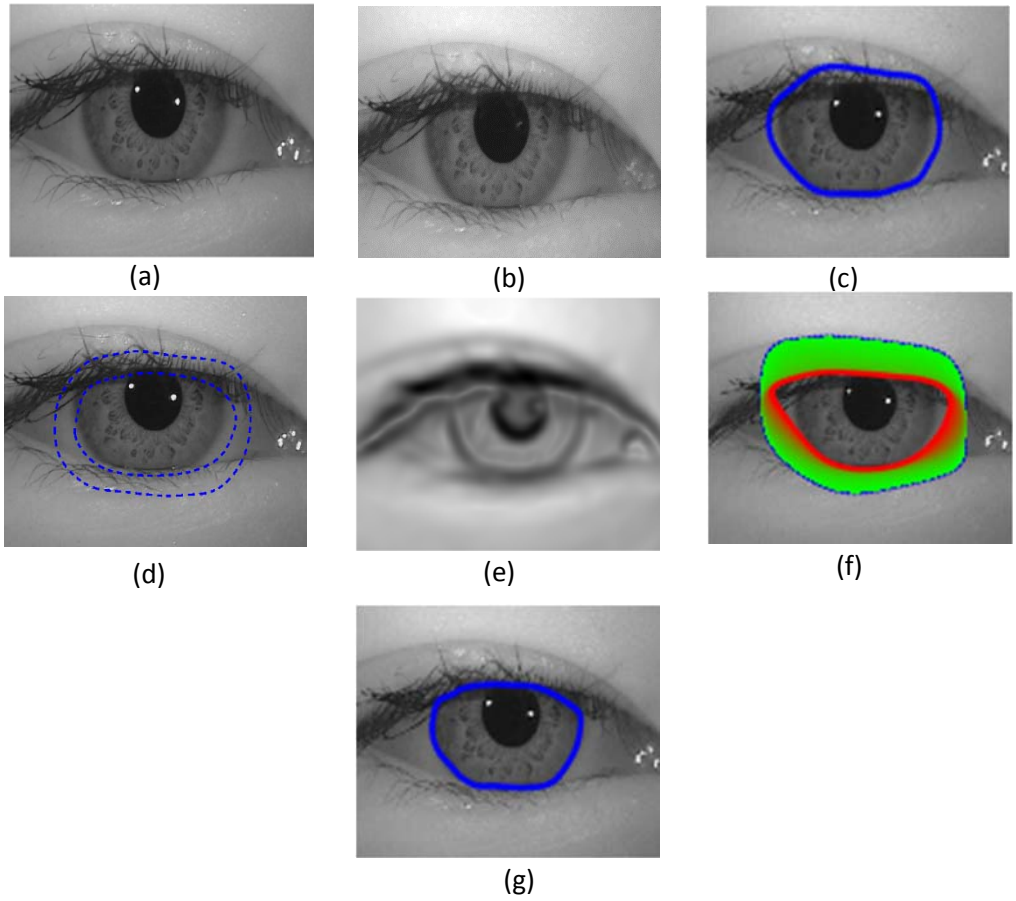

Figure 3.15: Sample iris image showing the GCBAC segmentation Process for the iris: (a) original iris image (b) pre-processed iris image (c) iris image showing initialized contour on the approximate iris boundary, (d) iris image showing the initialized contour and the dilated contour (e) GCBAC energy image, (f) iris image showing the initial contour and the dilated contour with the pixels labelling process in-between, (g) final image showing the segmented pupil.

Consider the original iris image to be segmented. The image is first pre-processed according to the proposed algorithm in section 3.4. This initial step is carried out to detect and remove noise and reflection which is capable of influencing the segmentation result. Now, a contour is initialized at the approximate boundary of the iris as shown in Figure 3.14 and 3.15. The initial contour is dilated into its contour neighbourhood (CN) in order to create a narrow band around the initial contour and minimize time. For the pupil segmentation, a structuring element of $+5$ is used to dilate the contour while for iris segmentation a structuring element of $+10$ was adopted. The computation of the minimal cut on the graph is achieved by minimizing the graph cut energy equation in (3.31). The difference in intensities within and outside the initial contour is computed using graph cut optimization, and a new contour is initialized based on the new subsets computed using the graph cut energy. The evolution of the contour to the new subset boundary does not

require an edge stopping function which is one of the main advantages of the proposed GCBAC. The edge stopping is now determined based on the result of the cut on the graph.

Given the pre-processed iris image, a contour is initialized in the first level at the approximate boundary of the pupil. Also, a contour embedding function $\emptyset$ is initialized as a signed distance function to $\gamma(t = 0)$. The discretization of the evolving contour is performed in a highly non-uniform manner according to Equation (3.26). The evolution of the contour needs to be fit to points on the iris boundary. The implication is that the thin-plate spline energy driving the contour will tend to zero if all the contour points lies on a circle. However, where there is non-uniform evolution of the contour, the thin-plate energy starts to rise in accordance to the degree of deviation of the contour from the initial contour. Therefore, a simple solution was proffered in [56] to deal with this problem. In [56], the difference between the initial contour and the evolved contour is computed in order to regulate the contour evolution scheme. Thus, where the difference between initial contour and the evolved contour is zero (which signifies that the evolution has reached the minimum cut), then the contour evolution is stopped. Also, if the difference is more a threshold of ± 5, (indicating that the evolution is highly irregular), the contour is re-initialized. However, where the graph cut boundary is irregular, the thin-plate spline energy may not be minimized and the contour can evolve continuously. This can affect the segmentation result and lead to the contour incorrectly encompassing some portions of the sclera inside the final contour. Therefore, refining the graph cut result using mathematical morphology approach yields a more precise contour on the iris boundary.

The proposed GCBAC model, has the advantage of overcoming the splitting and merging of the contour around boundaries. This particular property is very important in order to handle effects of radial fibres which can sometime be thick in some parts of the iris image, or dark crypts which might be present in the ciliary region of the iris image, leading to prominent edges. In segmentation techniques based on parametric curve (e.g., the snake segmentation technique [34]), the problem of “local minima” can cause the curve to terminate at some of these prominent edges. However, GCBAC is able to overcome such problems by basing the curve evolution on the graph cut energy which is not dependent on local information only. Thus, the proposed algorithm is able to deal effectively with the problem of local minima thereby ensuring that the final contour corresponds to the true iris boundary.

Also, the contour evolution process around a narrow band accelerates the evolution procedure significantly and hence, the whole discretization and normalization process is performed in less than a second in a C-Language environment. The evolution of the contour can be non-uniform around the boundary which is influenced by obstacles such as eyelashes, shadow, blur, etc. Therefore, the embedding function is re-initialized again after few iterations, by re-computing as a signed distance function from the new contour.

This hierarchical formation approach adopted here minimizes possible errors. The final segmentation of the iris boundaries is carried out in the following steps.

1. Set the index of the current step to $i = 0$.
2. Initialize a contour C on the given image according to Sections 3.4.1 and 3.4.2.
3. Dilate the current contour c_i into its contour neighbourhood $CN(c_i)$ within an outer contour OC_i.
4. Identify all the vertices belonging inside and outside the initial contour C as the source s_i and the sink t_i, respectively.
5. Compute the $s - t$ min cut to obtain a new boundary that better separates the inner boundary from the outer boundary.
6. Terminate the algorithm if the resulting contour $\hat{c}$ reoccurs, otherwise set $i = i + 1$, and return to step 1.

The iris images in figure 3.15, shows samples of iris images segmented using the proposed approach. The result show the accuracy of the segmentation method.

3.4 Eyelash Detection

Eyelashes are most times superimposed in the iris in non-ideal iris images. This can significantly hamper the recognition accuracy if not detected and excluded. The eyelash appears in the iris image as dark transient signals with high intensity variation than the background. This can easily be measured using the traditional wavelet transformation. In order to overcome the challenge normally posed by the heterogeneous nature of iris images, a block based approach is adopted for the estimation of the eyelash region before final detection of the eyelashes.

Let $I(N, M)$ be the original iris image which is then subdivided into blocks where each block is a sub-image of the original image. For each block $n \times m$, the local energy

is computed using discrete wavelet transform (DWT), which is a multiscale frequency decomposition technique [85]. The high frequency sub-bands of the detailed wavelet coefficients denoted by $D_i = \{HL, LH, HH\}$ are able to capture the high frequency variations in both horizontal, vertical and diagonal directions. The lowest computational cost wavelet transform, the Haar wavelet with one level of resolution is chosen to decompose each block into four frequency bands of size $\frac{n_l}{2} \times \frac{m_l}{2}$. The square root of the second order moment of wavelet coefficients in each detailed coefficient D_i is computed as defined in [50].

$$f(k) = \left(\frac{1}{2}\sum_{i=0}^{\frac{X_l}{2}}\sum_{j=0}^{\frac{Y_l}{2}} W_{k,i,j}^2\right)^{\frac{1}{2}} \qquad (3.33)$$

Where $k \in D_i$ and W_k represents the matrix of wavelet coefficients of the block in the D_i set. The texture descriptor representing the maximum energy of the block (local energy) is determined as

$$E_n = max f(k), \quad \forall k = D_i \qquad (3.34)$$

Where $f(k)$ is the energy of the high frequency sub-bands. A 1-D energy vector E_n, is then used in block wise clustering approach to capture the region of interest (ROI) as shown in Figure 3.16c.

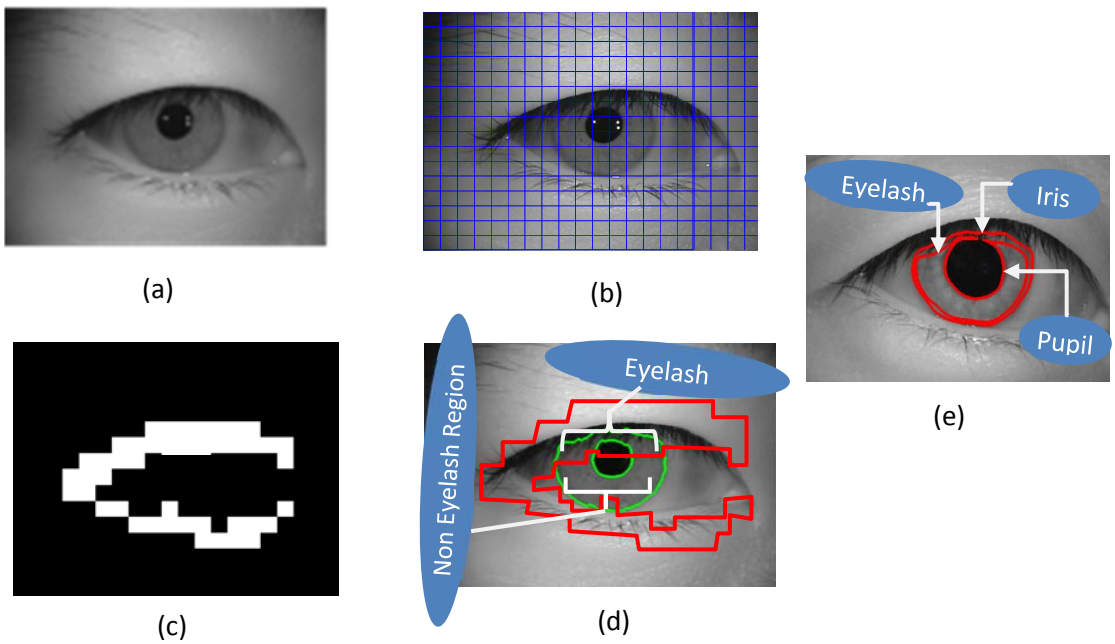

Figure 3.16: The eyelash detection process: (a) original image, (b) image partitioned into blocks, (c) result of block based classification, (d) iris image showing the candidate eyelash and non-candidate eyelash regions, (e) Eyelash segmented iris image

The classification of the blocks into candidate eyelash region (CES) and non-eyelash (NES) regions was achieved using a Bayesian classification approach. A Bayes classifier is a simple probabilistic classifier based on applying Bayes' theorem (from Bayesian statistics) with strong (naive) independent assumptions to predict data classes. Despite their naive design and over-simplified assumptions, naive Bayes classifier has worked quite well in many complex real world situations. Three regions are defined namely: high frequency B_H blocks, low frequency $B_L$blocks and medium frequency $B_M$blocks, respectively. High frequency blocks include regions in the image with high frequency (sharp edges) such as eyelash blocks, and pupil edge blocks. Having known the location of the pupil edges from the pupil segmentation process in section 3.4.4, it is very easy to eliminate the pupil edge blocks from the region of interest blocks. Low frequency blocks (with no edges at all or very smooth edges) include blocks such as limbic edge blocks and other smooth areas of the image while medium frequency blocks include blocks with weak edges such as separable eyelash blocks. Therefore the blocks of interest (BOI) is given as the sum of medium frequency B_M blocks and high frequencyB_H blocks. The regions are first estimated by applying k-means classifier to roughly cluster E_n into three classes and final classification is achieved using Bayes classifier given as follows:

$$P(x_n|E) = \frac{P(E^k|x_n)P(x_n)}{P(E)} \qquad (3.35)$$

Where $P(E^k|x_n)$ denotes the probability distribution of the extracted feature component E^k conditioned by the clustered result x_n.

Now, in order to detect the eyelash pixels, a relative difference ratio (RDR) based on energies of the eyelash candidate and non-eyelash candidate regions was used. This idea stems from the fact that the eyelash is normally darker than the surrounding iris background pixels and as such they portend higher energy than the iris pixels.

Let $E_i^{\vec{d}}(x,y)$ be the regional energy term for a particular region of the iris, and $D_{i,k}^{\vec{d}}(x,y)$ be the gray level intensity value of the pixel in position(x,y). Where i is the resolution level, and $\vec{d}$ is the direction symbol representing horizontal, vertical and diagonal directions of the detailed coefficients of the wavelet transform and k represents the region. The regional energy can be computed as:

$$E_i^{\vec{d}}(x,y) = \sum_{n' \in L, m' \in K} \left[D_i^{\vec{d}}(n+n', m+m') \right]^2, \qquad (3.36)$$

Where $\overrightarrow{d} = 1,2,3$. The relative difference ratio of the eyelash candidate and non-eyelash candidate regions are then evaluated as

$$RDR = \frac{\left(\mu E_{i,k1}^{\vec{d}} - \mu E_{i,k2}^{\vec{d}} \right)}{\mu E_{i,k1}^{\vec{d}}}, \qquad (3.37)$$

Also, the standard deviation σ_i of the non-eyelash candidate region is also computed. Now for every iris pixel, if the mean energy $\mu E_i^{\vec{d}}$ (energy in horizontal, vertical and diagonal directions) is greater than one of its eight neighbours and is less than T, then the pixel is considered as an eyelash pixel. T is a threshold which is determined as:

$$T = \mu E_{i,k1}^{\vec{d}} - 2.5\sigma_i, \qquad (3.38)$$

3.5 Iris Image Normalization and Enhancement

Normalization is performed on the segmented iris image in order to achieve size invariance of the iris sample. We adopt the rubber sheet model [11] to normalize or unwrap the isolated iris area. The eyelash may occlude the iris region and significantly impact of the recognition performance. We apply eyelash detection strategy described in section 3.4, to exclude the eyelash portion. We create a binary mask based on the extracted iris contour and detected eyelashes. Since the elicited iris regions does not exhibit exact circular or elliptical properties, and may exhibit arbitrary shapes, a circle fitting strategy proposed by Shah and Ross [52] is employed to compensate for the size irregularities of the iris. In order to transform the detected iris region to rectangular form, the radius and corresponding centre coordinates of the iris needs to be estimated. Shah and Ross [52], considered only those points on the contour laying on the iris/sclera boundary, since the circle that fits all the points of the extracted contour may all lie inside the actual iris boundary especially if a significant portion of the iris is occluded by the eyelids. In our approach, we approximate the radius R, at six points selected from the extracted iris contour at the angles of [-30^o, 30^o, 0^o, 150^o, 180^o, 210^o] with respect to the

horizontal axis, and their average distance from the centre of the pupil are calculated. A circle fitting strategy is then adopted so that all the points on the contour are within a distance of $R \pm 15$ pixels from the centre of the pupil. The centre values obtained through the elliptical fitting process and the approximate radius of such as circle are used for the unwrapping process. Full description is available in [52]. The normalization produces a 2-D array with the horizontal dimensions corresponding to the angular resolution, and the vertical dimensions corresponding to the radial resolution. The images shown in Figure 3.13a, illustrates the approximate iris/pupil contours, while Figure 3.13b, shows the segmented iris images after iris/pupil localization, eyelash detection and iris/pupil boundary approximations.

In order to compensate for the elastic deformation of the iris texture, the localized iris regions is unwrapped into a normalized rectangular block of a fixed size 64×512, by converting from the Cartesian coordinate system to the polar coordinate system [11]. Given $I(x, y)$ as the localized image, the polar representation of the form $I(r, \theta)$ can be obtained as follows:

$$r = \sqrt{(x - x_i)^2 + (y - y_i)^2}, \qquad 0 \leq r \leq r_{max}, \quad (3.39)$$

$$\theta = tan^{-1}\left(\frac{y - y_i}{x - x_i}\right), \qquad (3.40)$$

Where r and θ are defined with respect to the centre coordinates (x_i, y_i). The centre coordinate values obtained during the elliptical fitting are used as the centre points for unwrapping the iris image.

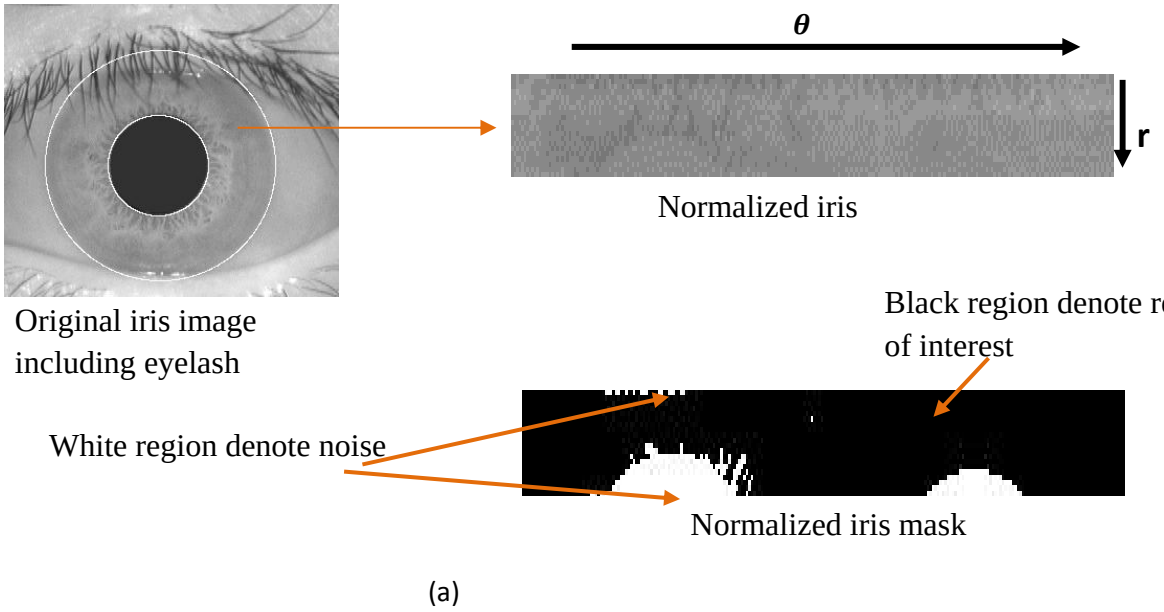

(a)

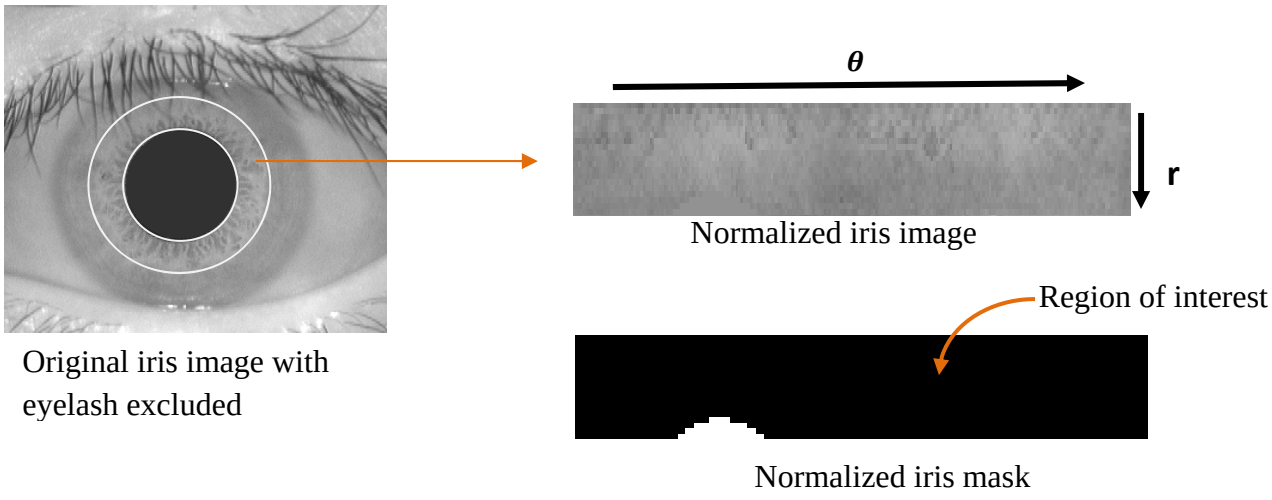

(b)

Figure 3.17: (a) unwrapping of the iris image without eyelash exclusion, (b) unwrapping of the iris image with the eyelash occluded region excluded.

Figures 3.13a and b, show the normalized iris images. Since the normalized iris images are of relatively low contrast, and may also be affected by non-uniform illumination due to the positioning of light sources, a local intensity based histogram equalization technique is applied to enhance the image. This technique improves the quality of the normalized iris image, thereby increasing the recognition accuracy. Figures 3.13c and d show the effects of iris image enhancement using the histogram equalization technique.

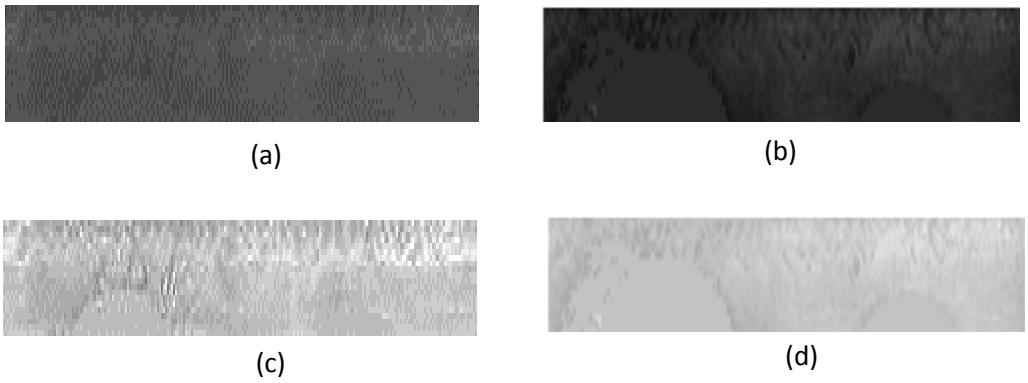

Figure 3.18: The results of the iris sample enhancement; (a, b) shows the unwrapped iris image before enhancement, (c, d) shows the unwrapped iris image after enhancement.

3.6 Summary

In this chapter, the model for the accurate segmentation of the pupil and iris boundaries have been presented. The key steps of this model include: reflection detection and removal using a multiresolution edge-weighted highpass filter and an exemplar based image inpainting method, iris boundaries segmentation using a two level, two steps hierarchical approach based on graph cut optimization and active contour method and a post processing operation for the removal of eyelashes and shadows using a block based classification and statistical prediction method. A normalization method based Daugman's rubber sheet model is also applied to normalize the segmented iris image. The algorithm is accurate at localizing iris boundaries by combining both local and regional information of the iris to estimate and refine iris boundaries. Also, the algorithm is robust at handing most of the non-idealities of the iris image using pre-processing and post-processing operations.

Chapter 4

4 DISTINCTIVE IRIS FEATURE EXTRACTION AND CLASSFIFICATION FOR IRIS BIOMETRICS

This chapter presents the feature extraction and classification methods used in this work. In Section 4.1, a brief introduction to the subject of iris feature extraction and classification for iris recognition is presented. The proposed feature extraction methodology is discussed in Sections 4.2 and 4.3. While, Section 4.4 introduces the iris pattern matching and classification process adopted in this work. Section 4.7 summarizes the key points and contributions of this chapter.

4.1 Introduction

Due to the increasing demand for enhanced security, iris based biometrics for personal identification has become a hot research topic in the fields of pattern recognition, computer vision, machine learning and computer security [13-46]. Most current state-of-the-art iris recognition algorithms focus mainly on improving the iris pre-processing module for iris recognition, but recently, important new directions have been identified in the area of iris feature extraction research for iris biometrics. Iris feature extraction is a process used for extracting or deriving informative and non-redundant values (features) from the iris sample which is intended to facilitate the learning and/or recognition of an individual's iris pattern. The iris feature extraction is effectively a type of dimensionality reduction technique that efficiently represents interesting parts of the iris image as a compact feature vector. This is useful in order to reduce the dimensionality of the feature vector and for fast image matching and classification. It is also important for the representation of the iris sample with a more invariant feature vector which is more stable even if there is a change in the original sample by rotation, scale, size, and translation. The general aim of iris feature extraction and representation is to represent the iris sample with a small enough as well as discriminative enough feature vectors which is able to distinguish one sample from another. By discriminative feature vector we mean the ability

of the feature vector to possess unique information that can distinguish it from the feature vector of another sample.

Daugman [8-11] in his work utilized a multi-scale 2-D complex Gabor filters to demodulate the texture phase structure information of the iris image. The decomposition of the iris image using the 2-D complex Gabor filters generated a 1024 complex-valued phasors which denote the phase structures of the iris at different scales. The phasors are then quantized into four quadrants in the complex plane giving rise to 2048 component iris code, used to represent the iris. This can be considered to be of high dimensionality as a feature code. The high dimensionality of the iris code can have a major impact on the efficiency of the subsequent matching and classification modules. A method needs to be adopted in order to reduce the dimensionality of the iris code while still maintaining a high level of accuracy of IrisCode for representing an individual's iris pattern.

In this chapter, we propose an iris recognition scheme based on Principally Rotated Complex Wavelet Filters PR-CWF for iris texture feature extraction. Particle Swam Optimization (PSO) is employed for feature selection and encoding while adaptive support vector machine (ASVMs) is used for matching and classification. PR-CWF is able to elicit important discriminative iris features from the iris image in the directions of the principal texture pattern. In the second stage, the PSO which is a population based stochastic optimization technique is employed to select optimal features from the feature vector pool for the correct representation of the iris sample. Also, instead of using the entire iris image for feature extraction, we elicit the iris information from a subsample of the localized iris image in order to reduce errors caused by occlusions from eyelids, eyelashes and shadow.

The selection of a feature subset from the original feature vector pool is relatively new in the field of iris feature extraction [53]. The process is aimed at significantly lowering the dimensionality of the feature set and increasing the overall speed of the system. The iris sample normally contain high level of textural features with comparatively small number of samples per subject, which makes accurate and reliable iris pattern classifications a difficult task [54-63]. The huge textural information in the iris create high level of redundancy in the extracted iris features. A feature selection scheme can be used to select the best features from the feature pool in order to reduce the feature dimensionality.

There have been many traditional selection schemes like *the Principal Component Analysis (PCA), Independent Component Analysis (ICA), Singular Value Decomposition (SVD),* etc., used for this kind of task. However they mostly require a sufficient number

of samples per subject in order to select the salient feature sequence present. Moreover, accumulating a large number of samples is costly due to the resources needed for the management of such huge data. Therefore, feature subset selection is a multi-criterion optimization problem, which increase the speed of the iris recognition system by lowering the computational task.

New feature selection schemes like *Genetic Algorithm* (GA) *and Neural Networks (NN)* have been proposed to solve this problem and produce improved performance. However, they also suffer from slow convergence and the likeliness to fall into local minima. The particle swam optimisation PSO which has many similarities with evolutionary computation technique like GA, presents an alternative approach to solving this kind of problem. PSOs are generally very effective in rapid global search of large, non-linear and poorly understood data [66]. The PSO is preferred to GA because it is easy to implement, has few parameters to adjust and unlike GA, PSO do not have evolution operators like crossover or mutation. In view of the many advantages of PSO, we adopt PSO based technique for the selection of the optimal feature subset from the extracted feature sequence.

SVMs have successfully been applied to solve a lot of classification problems due to their outstanding ability to interpret data geometrically. SVM is able to discriminate one class of data from the other by separating them with a hyperplane which has the maximum margin, for the binary cases [55], [56]. An SVM is a supervised learning model with associated learning algorithm which uses a vector space based machine learning method to find a decision boundary (hyperplane) between two classes that is maximally far from a point in the training data. The scheme is able to discount some points as outliers or noise in the classification process. With SVMs, the classification accuracy can be estimated by their expected misclassification rate on the target dataset. Therefore, it is assumed that the costs for different types of misclassification error are the same. However, this assumption is not always the case in many real world situations [56]. The two cases in which the above-mentioned assumptions are not valid are described as follows: The first case is the sample ratio bias, where in some conditions, especially in the one-versus-many condition, the sample proportion between two classes is highly unbalanced. The second case is a case where, the different types of misclassification error may have different costs, which can lead to different misclassification losses [57]. Most of the iris datasets suffer from the lack of sufficient iris samples per subject. Therefore, we have adopted the adaptive approach of SVMs by taking into account the above-mentioned issues. The proposed classification scheme with adaptive SVMs is well suited

for different datasets (like the CASIA [189] and the UBIRIS Nonideal [192] datasets), where the number of samples per subject is not fixed.

4.2 Distinctive Iris Features Extraction

In this section, we propose to apply the principally rotated complex wavelet filters (PR-CWF) to elicit the iris textural information from the iris image [27], [53]. The PR-CWF is formulated by constructing a complex wavelet filters and rotating the filters in the direction of the principal texture direction of the image. In comparison to Gabor wavelets which are symmetric with respect to their principal axis, and discrete wavelet transform (DCT) which is based on real value oscillating wavelet, complex wavelet transform is based on complex-valued oscillating sinusoids which is shift invariant, does not oscillate positive and negative around singularities and still maintains all other advantages of the DWT as already highlighted in Chapter 2, Section 2.4.

Several distinctive feature extraction algorithms have been proposed by many researchers to extract important iris feature set from the iris sample [56-60]. However, most of these algorithms do not perform well for non-ideal iris images captured under less-constrained imagery setup. A feature extraction method based on multiscale and multiresolution application of PR-CWF on the normalized and enhanced iris sample is proposed to cope with the low quality and degraded iris images under study in this work.

Some of the related research works on iris feature extraction have proposed interesting approaches which are relevant to this work. In [72], an extension of Gabor wavelet-based algorithm, which utilizes the local ordinal information extracted from original unfiltered images, was proposed to represent iris images while the modified Log-Gabor filters were deployed in [61] to extract the iris phase features which is more tolerant to the background illumination. Cai et al. [64], proposed an optical wavelet packet transform (OPWT) technique for the extraction of the iris features while, Bodade et al. [79], introduced the application of a combination of complex wavelet and rotated complex wavelet to elicit iris information.

In this work, PR-CWF is used to extract the characteristic values of the iris from the normalized (and enhanced) iris image, and the technique is well suited for analysing signals in a multi-resolution mode. The segmented iris image is first divided into four sectors. The upper and lower sectors are eliminated because of possible eyelash occlusion.

The right and left sectors as shown in Figure 4.2 and 4.3, are normalized and used for feature extraction. The normalized (unwrapped) iris image is first enhanced by applying a median filter to reduce the effects of non-uniform illumination and improve the quality of the image. Then, the principal direction θ of textures in the normalized iris image is computed using principal component analysis before iris feature extraction is performed using PR-CWF. The details of the process for the iris feature extraction are presented in the following subsections.

4.2.1 Principal Texture Direction Computation

Principal component analysis (PCA) have been widely used in the fields of pattern recognition and machine learning for feature analysis. PCA technique is normally employed to emphasise variation and highlight strong patterns in a dataset. It can be defined as a mathematical procedure that uses orthogonal transformation to convert as set of data of possibly correlated variables into a set of values of linearly uncorrelated variables called principal component [122-124]. The Principal Component Analysis (PCA) used in this work is only applied in order to compute the principal texture direction (PD) before application of complex wavelet filters to extract the iris features. The computation of the principal texture direction is very important since a subset of the features is going to be used as the end for representing the iris image. The most distinctive feature of the iris sample can be elicited by filtering along the principal texture direction. The principal texture direction (PD) of the iris texture pattern is first computed and the angle θ of the principal direction is subsequently determined by maximizing the variance of the projections of the input normalized image.

Now, given the normalized iris sample $N(i,j)$ we derive the principal components PC by maximizing the variances in the directions of the principal vectors. For the given normalized iris sample, with X Y-dimensional vectors n_j aligned in the data matrix X. Let u be a direction which is a vector of length 1. The projection of the j-th vector n_j onto the vector u can be computed using Equation (4.1) given as:

$$P_j = \vec{u}^T \cdot \vec{n}_j = \sum_{i=1}^{M} u_i n_{i,j} \qquad (4.1)$$

We now find a direction u that maximizes the variance of the projections of all the input vectors t_j, $j = 1, \dots N$, $i = 1, \dots, M$. The maximization function is given as follow:

$$J^{PCA}(\vec{u}) = \sigma^2(P_j) = \frac{1}{N}\sum_{j=1}^{N}(P_j - \overline{P})^2 = \dots = \bar{u}^T \sum \bar{u}, \qquad (4.2)$$

Where $\sum$ is the covariance matrix of the data matrix N**.** Let $N(i,j)$ denote a normalized iris image. The PCA can be given as:

$$\sum = \frac{1}{N}\hat{X} \,.\, \hat{X}^T, \qquad (4.3)$$

Where $\hat{X} = X - \mu \,.\, 1_{1xN}, \qquad \mu = [\mu_1, \dots\dots, \mu_m]^T$

So that

$$\sum = \begin{bmatrix} a_1 - \mu_1 & b_1 - \mu_1 & c_1 - \mu_1 \\ a_2 - \mu_2 & b_2 - \mu_2 & c_2 - \mu_2 \\ a_3 - \mu_3 & b_3 - \mu_3 & c_3 - \mu_3 \end{bmatrix}, \qquad (4.4)$$

From the covariance matrix $\sum$, the eigenvalues and eigenvectors are calculated. The eigenvalues and eigenvectors represents the direction of principal texture pattern. The largest eigenvalue equals the maximal variance, while the corresponding eigenvector determines the direction of the maximal variance.

For instance, the 1,1 entry of $\sum$ is given as:

$$\sum_{11} = \frac{1}{3-1}((a_1 - \mu_1)^2 + (b_1 - \mu_1)^2 + (c_1 - \mu_1)^2), \qquad (4.5)$$

Which is precisely the variance of the first variable. Also the 2, 1, entry of the covariance $\sum$ can be given as:

$$\sum_{11} = \frac{1}{3-1}\big((a_1 - \mu_1)(a_2 - \mu_2) + (b_1 - \mu_1)(b_2 - \mu_2) + (c_1 - \mu_1)(c_2 - \mu_2)\big), \qquad (4.6)$$

The eigenvector corresponding to the highest eigenvalue is the principal eigenvector and its angle can be given as:

$$\theta = arctan\frac{\lambda_i - \sum_{11}}{\sum_{21}}, \qquad (4.7)$$

Where λ_i represents the eigenvalues. Once the principal texture orientation has been computed, a complex wavelet filter is constructed in order to elicit important iris information in the direction of the principal texture.

4.2.2 Construction of the 2-D Complex Wavelet Filters

Once the principal texture direction is determined, a complex wavelet filter (CWF) is built and rotated in the angle θ of the principal texture direction and in the opposite angle of $\theta - 90^o$ in order to extract important iris information. This approach enables us to extract shift invariant and rotation invariant iris information for iris representation. As discussed earlier in Chapter 2, multiscale transforms are powerful tools for signal and image processing. The 1-D wavelet transform, which acts as a multiresolution version of the Nth-order derivative operator with N vanishing moments can be a good example of the multiscale transform. The extension of the I-D wavelet to multiple dimensions (especially 2-D) has gained the attention of researchers in image processing [56-60]. This is typically achieved by forming tensor product basis functions. Practically, the extension of 1-D wavelet transform to 2-D wavelet transform can be achieved by filtering the row and columns of the signal using separable filters. However, the major problem of separable wavelets is that it is not well matched to the singularities occurring in images, such as lines and edges, which can be arbitrarily oriented or even curved. Therefore, even the 2-D discrete wavelet transform suffers from poor directionality, shift sensitivity and lack of phase information which is the initial motivation behind the development of complex valued DWT. Moreover, the complex wavelet transform constructed in 2-D format is able to overcome most of the challenges of DWT highlighted earlier.

The complex wavelet transform (CWT) uses complex-valued filtering (analytic filter) to decomposes the real/complex signals into real and imaginary parts in the transform domain. The real and imaginary coefficients are them employed to calculate the amplitude and phase information, which holds the information needed to accurately describe the energy localization of the oscillating functions (wavelet basis). A detailed review of works in the domain of complex wavelets can be found in [122-123]. The design and supporting works of the complex wavelet transform is discussed in the following sections.

4.2.2.1 The Discrete wavelet Transform

The complex wavelet filters for signal analysis is constructed using two separable discrete wavelet filters. The term wavelet is used to refer to the oscillatory vanishing waves with time limited extend, which has the ability to describe the time-frequency plane with atoms of different time supports [115]. A wavelet is a mathematical tool which can be used to extract information from different kinds of signals, including images. Mathematically, a wavelet ψ can be stated as a function of zero average, having the energy concentration in time which can be given as [114]:

$$\int_{-\infty}^{\infty} \psi(t)dt = 0, \quad (4.8)$$

Then for more flexibility in extracting time and frequency information, a family of wavelets can be constructed from the function $\psi(t)$, which is also referred to as the 'Mother Wavelet', normally confined to a finite interval. 'Daughter Wavelets', $\psi_{u.s}(t)$ can then be formed from the 'Mother Wavelet' by translation and dilation with factors u and s, respectively, which can be expressed as follows [113-114]:

$$\psi_{u,s}(t) = \frac{1}{\sqrt{s}} . \psi\left(\frac{t-u}{s}\right) \quad (4.9)$$

Using these wavelets as a basis, the wavelet transform is able to decompose a signal over a set of dilated and translated wavelets in a multiresolution approach. This technique ensures that the time resolution is increased when the high frequency portion of the signal is analysed and the frequency localization is increased when analysing the low-frequency portion of the same signal.

The first implementation of wavelet is the continuous wavelet transform C_oWT which is highly redundant and difficult to implement for discrete types of signal. The discretization of the scale and translation variable of the wavelet termed Discrete Wavelet Transform (DWT) was introduced to overcome these challenges of C_oWT [110]. The discrete wavelet transform (DWT) is an implementation of the wavelet transform using discrete set of wavelet scales and translations that obey some defined rules. The first rules states that the scaling function $\emptyset$ must be orthogonal to its discrete translation which can be given by the dilation equation as follows [111]:

$$\emptyset(x) = \sum_{k=-\infty}^{\infty} \alpha_k \emptyset(S_x - k), \qquad (4.10)$$

Where S is a scaling factor usually chosen as 2. Also, the area between the function must be normalized and the scaling function must be orthogonal to its integer translations, which can be stated mathematically as follows [111]:

$$\int_{-\infty}^{\infty} \emptyset(x)\emptyset(x+l)dx = \gamma_{0,l}, \qquad (4.11)$$

Where, $\emptyset(.)$ is the scaling function and γ is the normalized function.

The discrete wavelet transform (DWT) involves the evaluation of the scale and shift parameters on discrete grid of time-scale plane which leads to a discrete set of continuous basis functions. The time-scale plane can be indexed using two integers, where the first integer, j corresponds to the discrete scale step while the second integer, n corresponds to the discrete translation step. The discretization is performed by setting the dilation parameter $s = s_0^j$ and the translation parameter $u = ks_0^j u_0$, for $j, k \in \mathbb{Z}$. Where, $s_0 > 1$, represents the dilated step, and $u \neq 0$, represents the translated step. The family of wavelets can then be given as:

$$\psi_{j,n}(t) = s_0^{-j/2}\, \psi\left(s_0^{-j}\, t - k\, u_0 s_0^j\right), \qquad (4.12)$$

Therefore, the discrete wavelet decomposition of a function $f(t)$ can be given as:

$$f(t) = \sum_j \sum_k D_f\,(j,n)\ \psi_{j,n}(t), \qquad (4.13)$$

Where $D_f\,(j,n)$ represents the 2-D set of coefficients of the function and $\psi_{j,k}(t)$ is the wavelet basis function (mother wavelet).

The discretization of the wavelet basis function is such that $s_0 = 2$ and $u_0 = 1$ is in the dyadic time-scale grid. Then, the selection of $\psi(t)$ representing the discrete wavelet transform is done in such a way that basis function set $\{\psi_{j,k}\}$ constitute an orthonormal basis of $L^2(\Re)$ such that

$$D_f(j,n) = \int_{-\infty}^{\infty} \psi_{j,n}^*(t) f(t) dt = \langle \psi_{j,n}(t) f(t) \rangle, \qquad (4.14)$$

This represents the wavelet basis for the evaluation of the function $f(t)$ using the summation of finite basis over index j and n with finite DWT coefficients.

The multi-resolution analysis (multi-scale analysis) (MRA) of the DWT is derived by a sequence of embedded subspaces given as: $V_2 \subset V_1 \subset V_0 \subset V_{-1} \subset V_{-2} \ldots \ldots \in L^2(\Re)$ as shown in Figure 4.1.

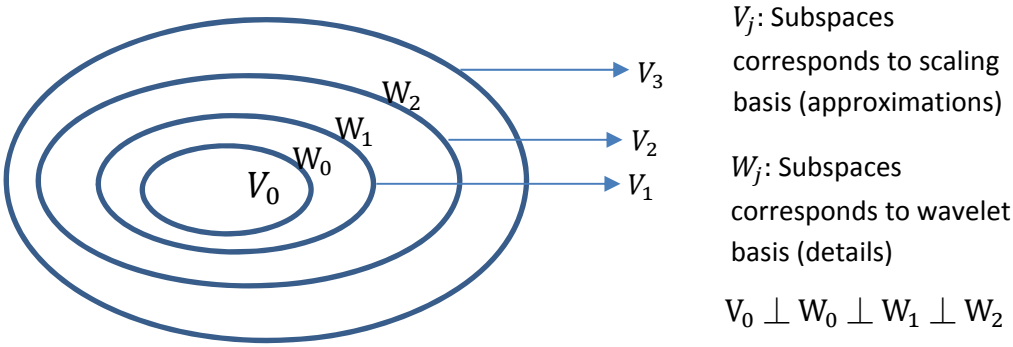

Figure 4.1: The nested vector spaces spanned by the scaling and wavelet basis functions.

These approximation spaces must satisfy the following conditions:

1. $V_j \subset V_{j+1,} \quad j \in \boldsymbol{Z}$
2. $V_{-\infty} = \{0\}$, and $V_{\infty} = L^2$,
3. $f(t) \in V_j \Leftrightarrow f(2t) \in V_{j+1}$
4. $V_2 = V_0 + W_1 + W_1$
5. $L^2 = \cdots + W_{-2} + W_{-1} + W_0 + W_1 + W_2 + \cdots = V_0 + W_0 + W_1 + W_2 + \cdots$
6. $W_{-\infty} + \cdots + W_{-2} + W_{-1} = V_0 \qquad (4.15)$

A scaling function $\varphi(t)$ (father wavelet) is introduced such that for each fixed j, the family of wavelets

$$\varphi_{j,n} = 2^{-j/2}\, \varphi\left(2^{-j/2}t - k\right), (j,n \in Z) \text{ and } \int \varphi(t)dt = 1 \qquad (4.16)$$

is an orthonormal basis for of the subspace V_j.

Therefore, if W_j is an orthonormal component of $V_j (W_j \perp V_j)$ in the subspace V_{j+1}, then there exist a function $\psi(t)$ (mother wavelet) such that for each fixed j, the family of wavelets can be given as:

$$\psi_{j,n} = 2^{-j/2}\,\psi\left(2^{-j/2}t - k\right), (j,n \in Z), \qquad (4.17)$$

Which is an orthonormal basis for the subspace W_j.

Then, given the nested subspace and the MRA conditions, the scaling function must satisfy the 2-scale dilation or refinement equation given as:

$$\varphi(t) = \sqrt{2}\ \sum_{n=-\infty}^{\infty} h_0[n]\ \varphi(2t-n), n \in Z \qquad (4.18)$$

Which satisfies that admissibility condition $\sum_n h_0[n] = \sqrt{2}$. Also, the wavelet function must satisfies similar condition which can be given as shown in equation 4.19.

$$\psi(t) = \sqrt{2}\ \sum_{n=-\infty}^{\infty} h_0[n]\ \varphi(2t-n), n \in Z, \qquad (4.19)$$

With conditions $\sum_n h_1[n] = 0$ and $h_1[n] = (-1)^n\ h_0[-n+1]$.

Where, $h_0[n]$ and $h_0[n]$ represents the coefficients of the lowpass and highpass filters, respectively. The MRA of any function $f(t)$ can be computed using both the scaling and wavelet function as follows:

$$f(t) = \sum_{j-J_0}^{J_1}\sum_{n=-\infty}^{\infty} C_f(j,n)\ \varphi_{J_1\,n}(t) + \sum_{j-J_0}^{J_1}\sum_{n=-\infty}^{\infty} D_f\ (j,n)\ \psi_{J,n}(t), \qquad (4.20)$$

Where, $C_f(j,k) = \langle \varphi_{j,k}(t), f(t)\rangle$ are the scaling function coefficients, J_0 is the arbitrary starting scale for coarsest resolution, and J_1 is an arbitrary finite upper limit for the highest resolution with $J_1 > J_0$.

Therefor, $C_f(j,k)$ and $D_f\ (j,k)$ represents the scaling coefficients (approximations) and the wavelet coefficients (details), respectively for the discrete wavelet transform (DWT) of the signal $f(t)$. The successive lower resolution of the signal are then recursively derived based on equations (4.21) and (4.22) with MRA concept as follows:

$$C_f\ (j+1,k) = \sum_n h_0[n-2k]\ C_f(j,n), \qquad (4.21)$$

$$D_f\ (j+1,k) = \sum_n h_1[n-2k]\ C_f(j,n), \qquad (4.22)$$

These equations are implemented as a tree-structured filterbank as shown in Figure 4.2.

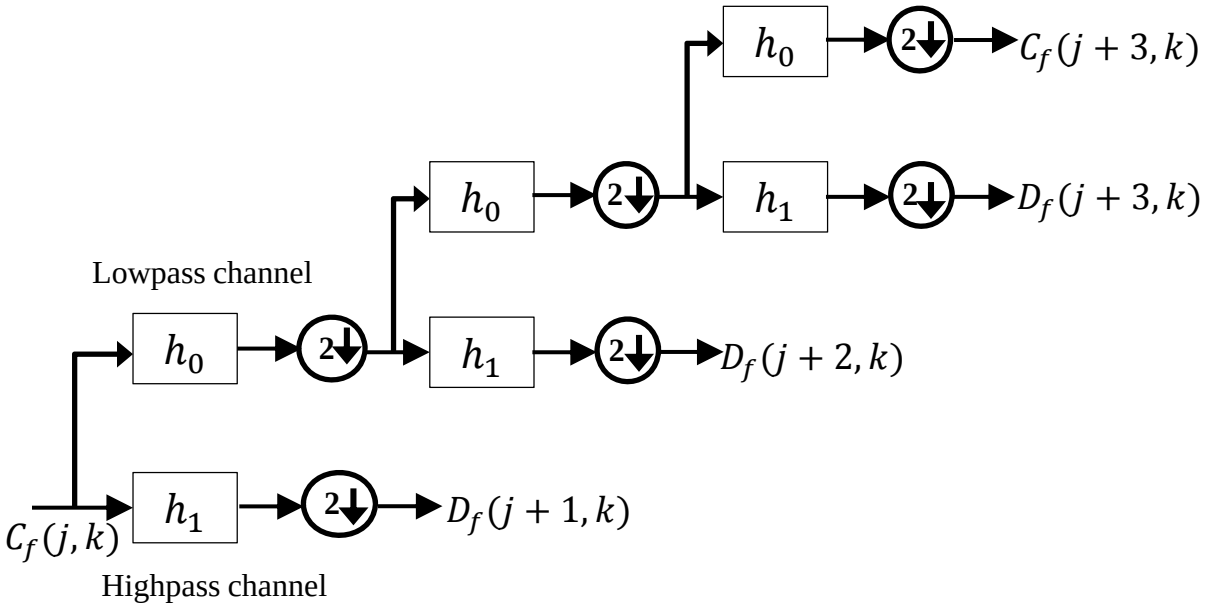

Figure 4.2: The three-level two-channel analysis filterbank structure for 1-D DWT

The Figure 4.2 shows the standard 1-D DWT tree structure for the analysis of signals. From the figure, we can see that the size of the approximate (scaling) coefficients and the detailed (wavelet) coefficients decrease by a factor of 2 at each successive decomposition level. Thus, the standard DWT is perfectly non-redundant version of $O(n)$ representation of a given signal in the multi-resolutional, multi-scale environment. Also, the DWT function satisfies the perfect reconstruction conditions. The reconstruction ability of the DWT is not discussed in this work as we are only interested in the analysis side of the signal or image rather than the synthesis. This forms the basis for the construction of PR-CWF which we will be discussing later in this chapter.

4.2.2.2 Extension to Two Dimensional Discrete Wavelet Transform (2-D DWT)

In section 4.2.2.1, we have discussed the simple implementation of the 1-D DWT filterbank structure. However, image analysis/processing requires the implementation of 2-D wavelet transforms. This can be achieved using separable dyadic 2-D DWT, which is only an extension of the 1-D DWT applied separately on the rows and then the columns of the image.

The implementation of the DWT analysis filterbank for a single level 2-D DWT is as shown in Figure 4.3.

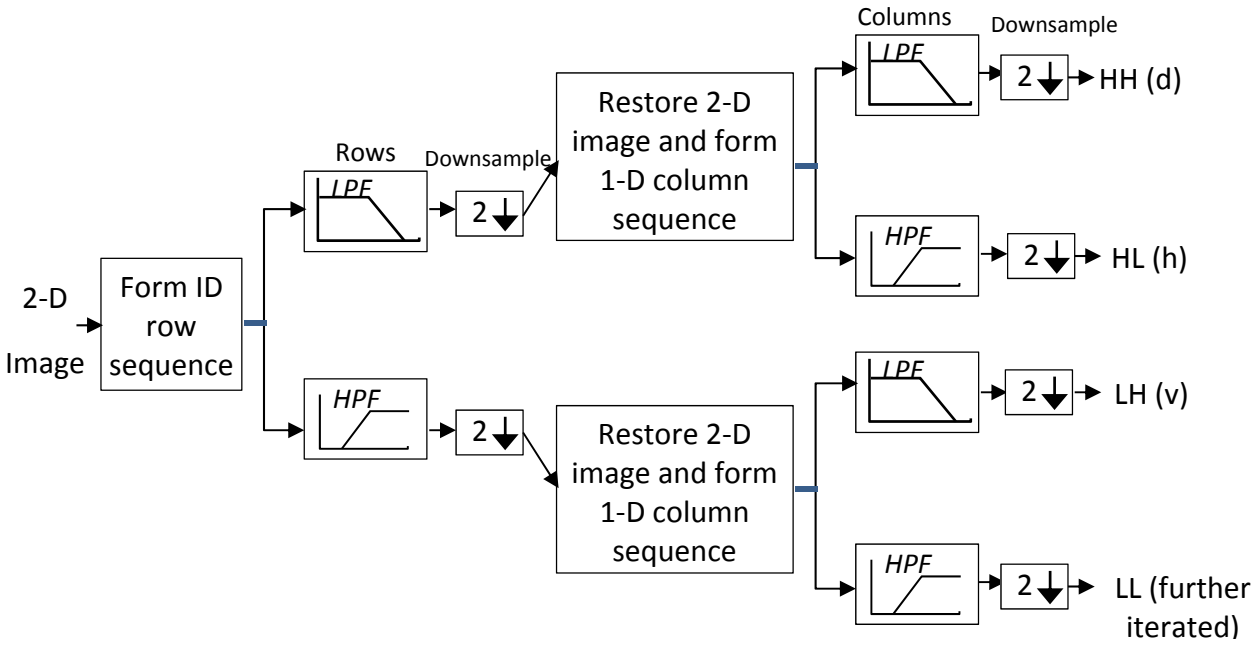

Figure 4.3: A single level analysis filterbank structure for 2-D DWT

The structure gives three detailed sub-images (HH, HL and LH) which corresponds to three different directional orientations (diagonal, horizontal and vertical), respectively. The lower resolution sub-image LL represents the approximation coefficients which can be further iterated to the second and higher levels of the wavelet decomposition. The further iteration of the LL channel give rise to the multilevel decomposition. The multilevel decomposition hierarchy of an image can be illustrated as shown in Figures 4.4. The corresponding coefficient in the higher levels are aliased ash shown in Figure 4.4 and there is a $1/4$ reduction in the size of the image coefficients at higher levels as well.

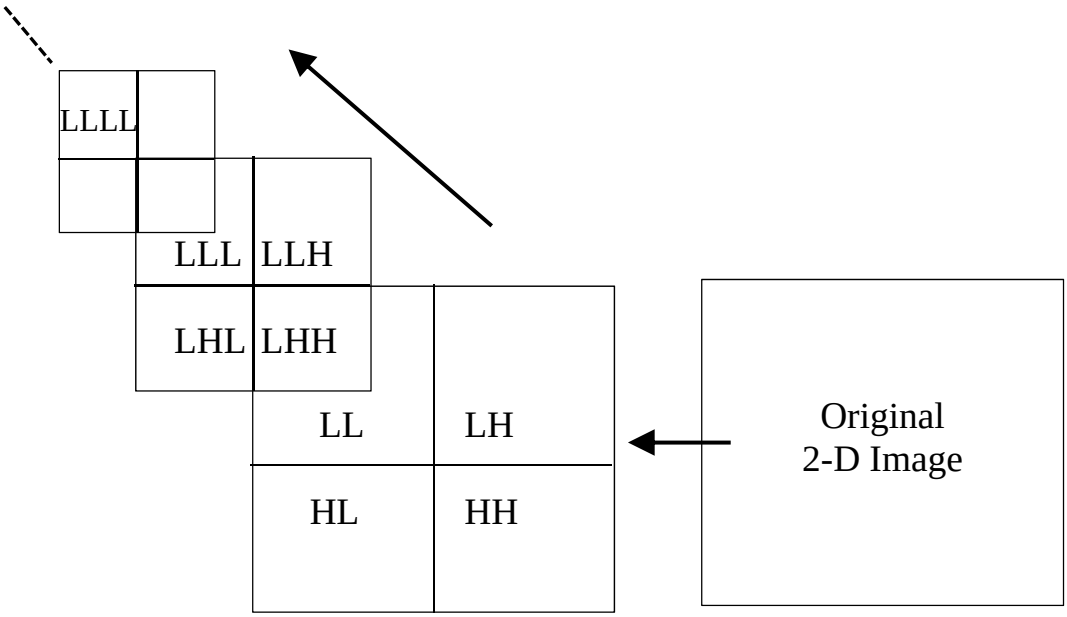

Figure 4.4: Multilevel decomposition hierarchy of an image with 2-D DWT.

The decomposition of the image using 2-D DWT breaks the parent image into four child images at each level. Each of the sub-images is $1/4$ the size of the parent image as mentioned earlier. The sub-images are placed according to the position of each sub-band in the 2-D partition of the frequency plane as shown in Figure 4.4. The synthesis filter bank structure follows exactly the same implementation of the filterbank in reverse order using synthesis filters $\widetilde{h_0}$ and $\widetilde{h_1}$. Synthesis is not discussed in this work because our implementation does not require image synthesis.

The separable wavelets are also described as tensor products of 1-D wavelets and scaling functions. Therefore, given a 1-D wavelet $\psi(x)$, associated with 1-D scaling function $\varphi(x)$, the three 2-D wavelets associated with the three sub-images are given as follows:

$$\psi^V(x,y) = \varphi(x)\,\psi(y) \longrightarrow \text{LH}, \quad (4.23)$$

$$\psi^H(x,y) = \psi(x)\,\varphi(y) \longrightarrow \text{HL}, \quad (4.24)$$

$$\psi^D(x,y) = \psi(x)\psi(y) \longrightarrow \text{HH}, \quad (4.25)$$

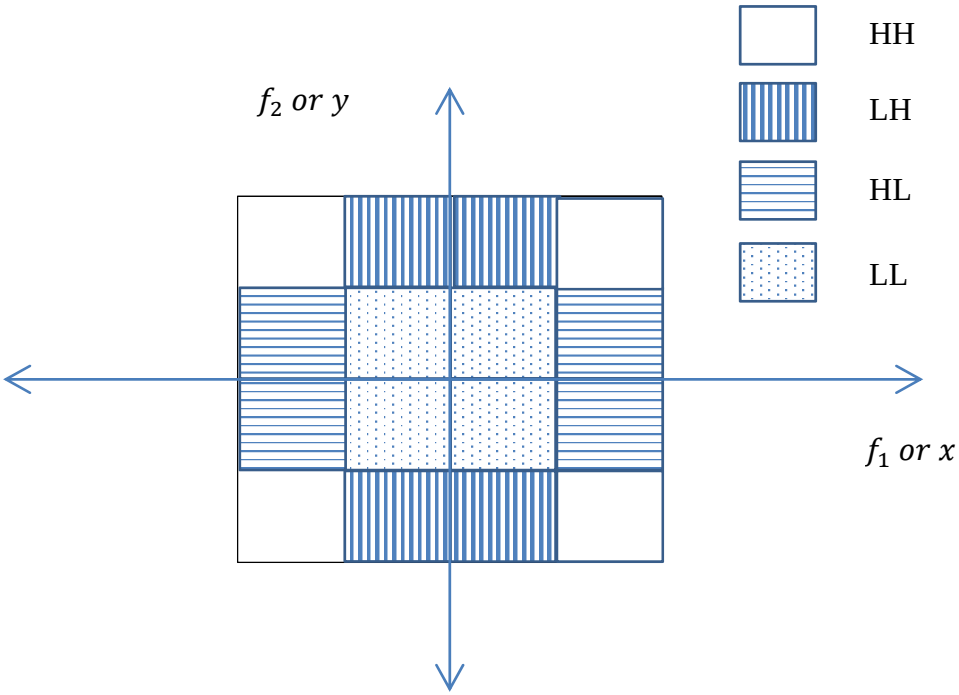

Figure 4.5: Frequency plane partitioning of the 2-D DWT

The arrangements of the wavelet coefficient according to the positional sub-bands are as shown Figure 4.5. There are also various extensions of non-separable 2-D wavelet transforms but we are only interested in the separable 2-D wavelet transform in this work. Figure 4.6, is a test iris image and its 2-D DWT decomposition carried out using the Matlab wavelet toolbox.

As can be seen from Figure 4.6, the 2-D DWT is only directionally oriented in three direction (horizontal, vertical and diagonal) which limits its ability to extract information about curves and bends in images. Also, the 2-D DWT lacks the ability to encode phase information which leads to lack of feature positional information in the analysis of images using DWT. These setbacks have lead researchers to look for more reliable means of analysing image information.

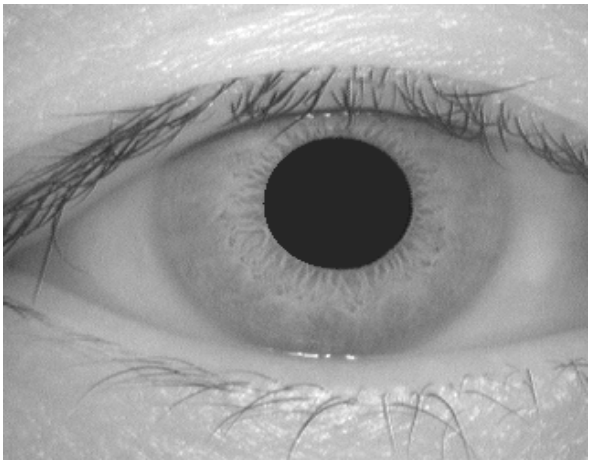

(a)

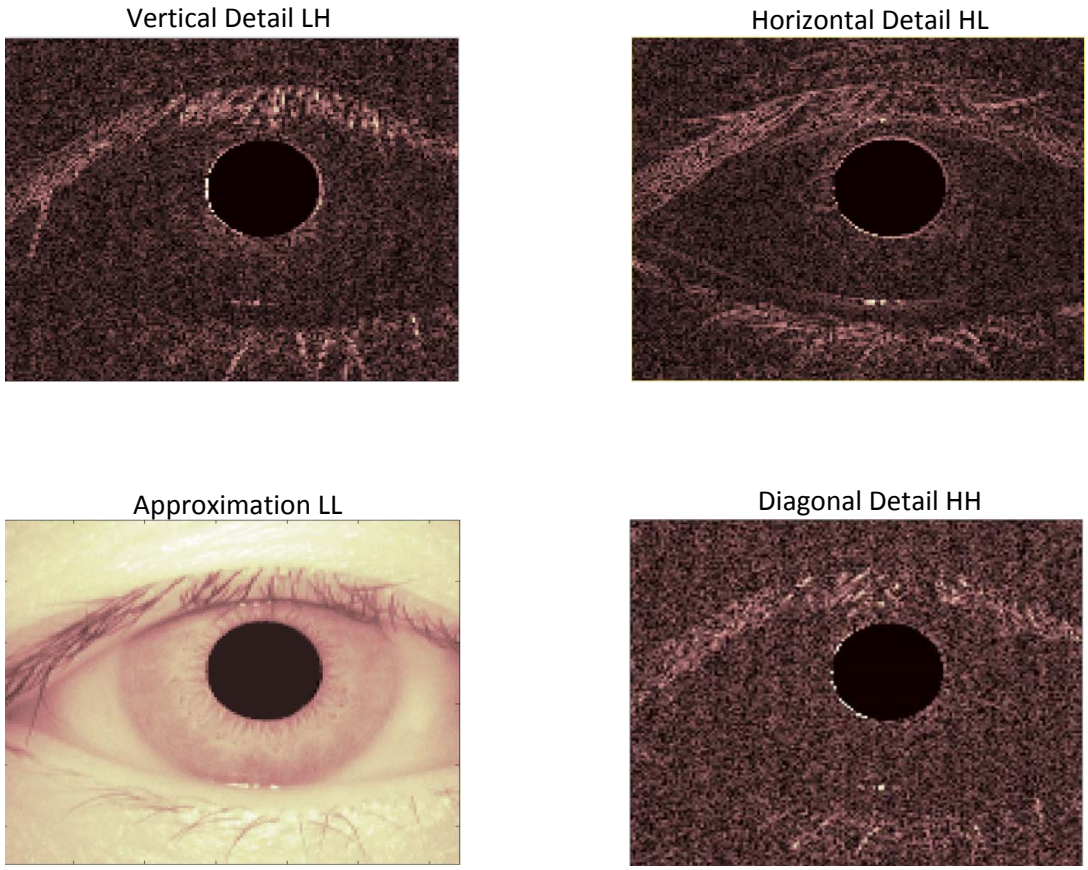

(b)

Figure 4.6: Single level decomposition of original iris image using Haar DWT, (a) Test iris image, (b) single level 2-D DWT decomposition of the same image.

4.2.2.3 The Two Dimensional Dual Tree CWF Design Structure

In our earlier discussion, it's been highlighted that the standard DWT and its extensions suffer from two or more major limitations, which is the main motivation behind the development of the complex-valued wavelet Transform (CWT). The absence of phase information in DWT limits its applicability to image processing. Also, the limited directional selectivity and the lack of shift invariance pose a great hindrance to its application for image texture analysis. The Complex Wavelet Transform (CWT) employs a complex-valued filterbank (analytic filter) for the decomposition of the real/complex signals into real and imaginary parts in the transform domain. The real and imaginary coefficients are then used to compute the amplitude and phase information, which is very necessary for accurately describing the energy localization in a given image sample. Edges and texture patterns in images manifest themselves as oscillating coefficients in wavelet domain. The amplitude of such coefficients describe the strength of the singularity while the phase indicates the location of the singularities. Therefore, to determine the correct value of the localized envelop and the phase of the oscillating function, 'analytic' or 'quadrature' representations of the image is needed. This type of representation can be obtained from the Hilbert transform of the image coefficients employed in complex wavelet filterbank CWF of CWT. Also, the CWT based on the Fourier sinusoid does not oscillate positive and negative in the transform domain which make it shift invariant.

The CWT is based on Fourier Transform unlike the DWT which is based on the real-valued oscillating wavelets. Therefore the CWT does not suffer from oscillations from positive to negative in magnitude as do DWT but is based on a smooth positive envelop in the Fourier domain. The magnitude of the Fourier transform is perfectly shift invariant, with a simple linear phase offset encoding the shift and the also, the Fourier coefficient is not aliased and does not require complex aliasing cancellations for signal reconstruction. These great attributes of CWT coupled with the its multiresolution property makes complex wavelet filterbank and attractive functional for the analysis of high textured image like the iris.

The complex valued sinusoid of the Fourier transform can be given as [114]:

$$e^{j\Omega t} = \cos(\Omega t) + jsin(\Omega t), \qquad (4.26)$$

Where, $j = \sqrt{-1}$. The oscillating sine and cosine components represent the real and imaginary parts, respectively and they form a Hilbert transform pair which means they are 90^o out of phase with each other. The cosine and sine component together form an analytic signal $e^{j\Omega t}$ which is supported on only one half of the frequency axis (Ω>0). The complex wavelet transform CWT was inspired by the Fourier representation of the signal whereby the signal is represented by the complex-valued scaling function and complex-valued wavelets which can be given as [114]:

$$\psi_c(t) = \psi_r(t) + j\psi_i(t), \qquad (4.27)$$

Where, $\psi_r(t)$ represents the real and even component while $\psi_i(t)$ represents the imaginary and odd component. Both $\psi_r(t)$ and $\psi_i(t)$ form a Hilbert transform pair which means that $\psi_c(t)$ is analytical and supported only on one half of the frequency axis. The complex scaling function is also similarly defined. See, [114] for more details. The complex wavelet coefficients of a signal can be obtained by projecting the signal on to the complex wavelet basis function $2^{j/2}\psi_c(2^j t - n)$ as follows:

$$d_c(j,n) = d_r(j,n) + jd_i(j,n) \qquad (4.28)$$

Where the magnitude can be given as:

$$d_c(t) = \sqrt{|d_r(j,n)|^2 + |d_i(j,n)|^2}, \qquad (4.29)$$

And the phase as:

$$\angle d_c(j,n) = \arctan\left(\frac{jd_i(j,n)}{d_r(j,n)}\right), \qquad (4.30)$$

Where, $|d_c(j,n)| > 0$.

Complex wavelet transform can be broadly classified into two namely: redundant and non-redundant complex wavelet transform. The details of the theories of redundant and non-redundant CWTs can be found in [114]. In this work, we focus on the redundant CWT with dual tree approach which is more relevant to our filter design. The redundant CWT with both $\psi_r(t)$ and $\psi_i(t)$ individually forming orthogonal and biorthogonal basis function results in a 2x redundant tight frame in 1-D with the power to overcome the shortcomings of the DWT. The dual-tree CWT based on two filter bank FB trees was introduced by Kingsbury [114], and is designed using two standard DWT filters. This is

an effective way of implementing an analytic wavelet transform. The dual CWT employs two real DWTs where the first DWT gives the real part of the transform while the second DWT gives the imaginary part. The analysis filter bank FB structure used to implement the dual-tree CWT is illustrated in Figure 4.7. The two real wavelets use two different set of filters, where each must satisfy the perfect reconstruction PR condition. Also, in addition to that, the filters are designed so that the complex wavelets $\psi(t) \coloneqq \psi_r(t) + \psi_i(t)$ is approximately analytic. Therefore, they are designed so that the $\psi_i(t)$ is approximately the Hilbert transform of $\psi_r(t)$, which can be denoted as $\psi_i(t) \approx \mathcal{H}\{\psi_i(t)\}$. In other to achieve this, two almost similar complex wavelet filterbanks are employed in a dual-tree structure to achieve the quadrature filter (Hilbert pair) effect. These redundant type of filters involves two conventional DWT filterbank trees working in parallel with respective filters of both trees in approximate quadrature. Therefore, the DT-CWT provides phase information and are shift invariant with improved directionality. These attributes is the major motivation for the application of complex wavelet transform for image analysis.

Figure 4.7, shows a 1-D DT-CWT spanned over three levels. The DT-CWT filterbanks structure shows close resemblance to the filterbank structure of standard DWT shown in Figure 4.2, with twice the complexity. It can be interpreted as two standard DWT trees operating in parallel to each other. One tree is called the real tree while the other is called the imaginary tree. For the purpose of clarity, the real tree might also be referred to as tree-a while the imaginary tree can be referred to as tree-b. As a result of the dual tree implementation, the dual-tree CWT exhibits less shift variance and more directional selectivity than the critically sampled DWT, with only a 2^d redundancy factor for d-dimensional signal, which is much less compared to $\log_2 N$x redundancy of a perfectly shift invariant DWT.

The Fourier based complex wavelet transform (CWT) structure based on a form of conjugate filter can be given as follows [114]:

$$\psi_x = h_x + j\mathrm{g}_x, \qquad (4.31)$$

Where, h_x is the set of filters $\{h_0, h_1\}$, and g_x is the set of filters $\{\mathrm{g}_0, \mathrm{g}_1\}$, both sets in 1-D ($x - direction$) only. Also, the filters h_0 and h_1 are the real-valued lowpass and highpass filters, respectively for tree-a. The same applies for g_0 and g_1 which are also the lowpass and highpass filters, respectively for tree-b as well. With $j = \sqrt{-1}$, The

oscillating cosine (real) and sine (imaginary) components form a Hilbert transform pair. Also, the filters $\{h_{ia,}\, h_{ja}\}$ form a pair of conjugate filter in the real tree and the complex tree filters $\{g_{ib}, g_{jb}\}$ is another pair of conjugate filter for the imaginary tree. All the filters are orthogonal and are also real-valued. Also, in order to satisfy the Hilbert transform pair and approximate analytic wavelet conditions, filter from both trees are made to be offset of each other by a half-sample delay after the first level.

In the implementation of the DT-CWT, the filters at first stage is required to be different from the filter at successive stages of the wavelet decomposition in other to achieve the Hilbert transform pair and meet the analytic condition. This is because to get uniform intervals between samples from the two trees below level 1, the filters in one tree must provide delays that half a sample different from those of the other trees. Therefore, the (10, 10)-tap filter and the db7 filters are chosen for tree a and tree b, respectively. These are fully decimated wavelet filters providing odd length in one side and even length in the other side of the tree.

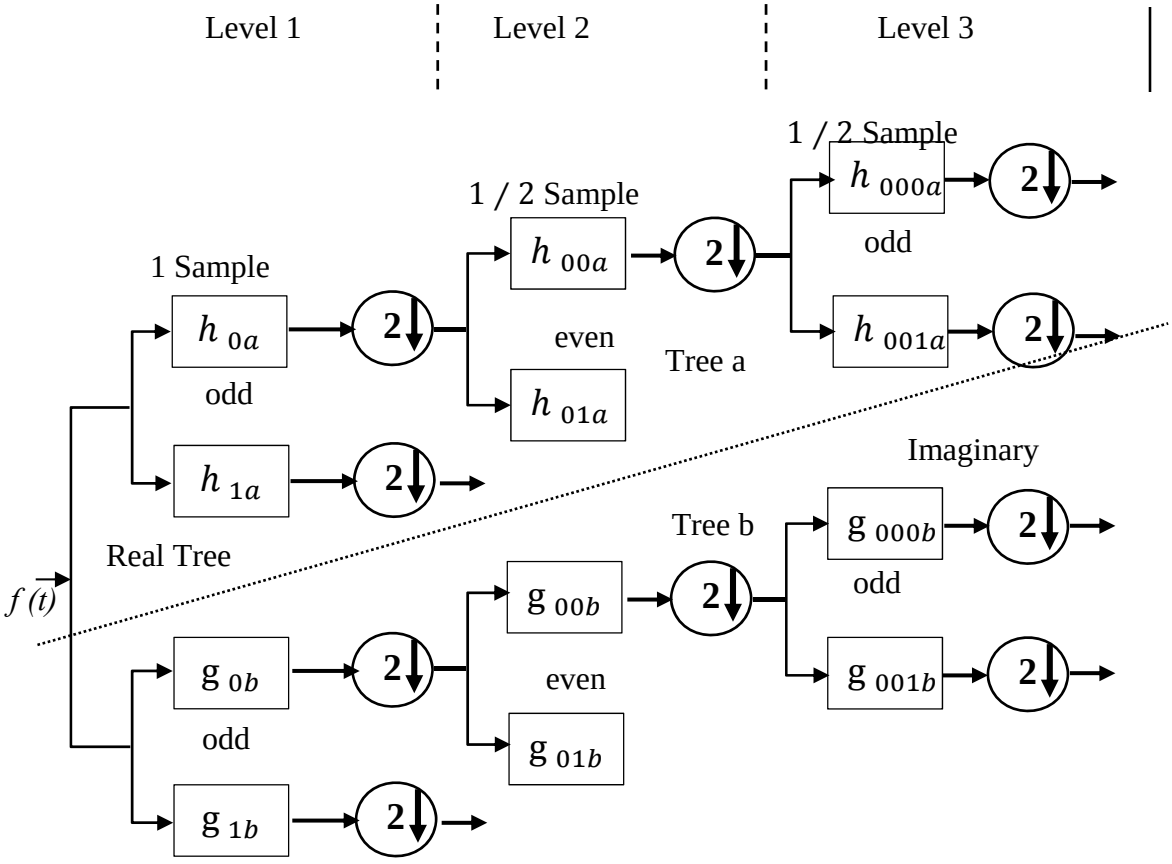

Figure 4.7: Structure of the Complex Wavelet Filter analysis using odd and odd-even filters.

The shift invariance can be achieved with the real wavelets by doubling the sample rate at each level of the tree. However, the samples must also be evenly spaced. The sampling rate can be doubled by eliminating the down sampling of DWT by 2 after the level 1 filters. This is equivalent to having two parallel fully-decimated trees a and b as shown in Figure 4.7, provided that the delays of g_{0b} and g_{1b} are one sample offset from h_{0b} and h_{1b}. Therefore, the lowpass filter after the first level and at first level 1 is given as follows:

$$h_{00}(n) = h_0(n - 0.5), \qquad (4.32)$$

$$h_0(n) = h_0(n - 1), \qquad (4.33)$$

Whereas the highpass filters area similarly given as follows:

$$g_{00}(n) = h_1(n - 0.5), \qquad (4.34)$$

$$g_0(n) = h_1(n - 1), \qquad (4.35)$$

To achieve the half-sample delay difference between level-1 and higher-levels the filter periods of 0 and $\frac{1}{2}$ were chosen. This is achieved by using with an asymmetric even-length filter $H(z)$ and its time reversed filter $H(z^{-1})$ [114] as mentioned earlier. The combination of the quadrature tree components of each coefficient is performed by a simple sum and difference operations. This yields a pair of complex coefficients which forms two separate sub-bands in adjacent quadrants of the 2-D spectrum. The lowpass filter for the imaginary tree is then derived from the half sample delayed condition of the real filters.

Kingsbury [114], in an earlier work have proposed the extension of the DT-CWT to 2-Ds, in order to achieve greater orientation selectivity and perfect shift invariance. The extension of complex wavelets to 2-D is achieved by applying two separable filters along the rows and columns of the image. The 2-D DT-CWF structure is an extension of conjugate filtering in 2-D. The filterbank structure of the 2-D dual-tree CWF is as shown in Figure 4.8. The 2-D separable DWT can now be expressed in terms of 1-D scaling functions (φ) and the wavelet function (ψ) as follows [81]:

$$\psi^0(x, y) = \varphi(x)\,\psi(y), \qquad (4.36)$$

$$\psi^{90}(x, y) = \psi(x)\,\varphi(y) \qquad (4.37)$$

$$\psi^{\pm 45}(x, y) = \psi(x)\psi(y), \quad (4.38)$$

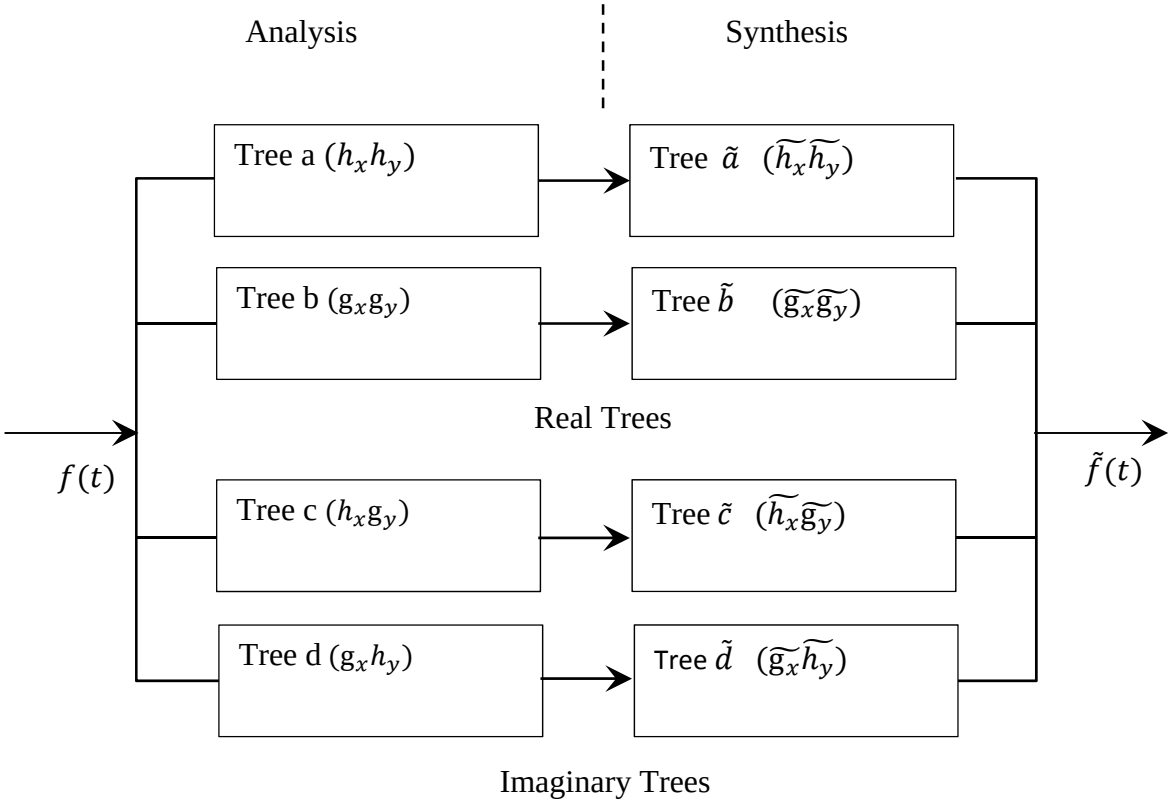

Figure 4.8: Filterbank structure of the 2-D DT-CWT

As shown in figure 4.8, the 2-D structure needs four trees for analysis and same for synthesis. The oriented non-separable 2D wavelets transform is derived by combining the sub-bands of two separable 2-D DWTs. The pairs of conjugate filters are applied to two dimensions x and y, which can be expressed as follows [81-82]:

$$(h_x + jg_x)\big(h_y + jg_y = (h_x h_y + g_x g_y\big) + j\big(h_x g_y + g_x h_y\big), \quad (4.39)$$

Then, the real part of the 2-D DT-CWT is obtained by combining Tree-a and Tree-b ($h_x h_y - g_x g_y$). Similarly, the imaginary part of the 2-D DWT tree of the CWT is obtained from Tree-c and Tree-d ($h_x h_y + g_x g_y$). The 2-D decomposition of the image is performed stage-by-stage in a standalone mode and a total of 6 sub-bands of detailed image coefficients are derived at each stage with three being for the real tree and the other three for the imaginary tree. Then, at each level, the resulting three sub-bands of the 2-D

DWT are oriented in the directions: horizontal(0^o), diagonal (45^o) and vertical(90^o). Therefore, the six sub-bands of the 2-D DT-CWT are therefore derieved as follows [81]:

$$\psi_{1,1}(x,y) = \varphi_h(x)\,\psi_h(y) \qquad \psi_{2,1}(x,y) = \varphi_g(x)\,\psi_g(y), \qquad (4.34)$$

$$\psi_{1,2}(x,y) = \psi_h(x)\varphi_h(y) \qquad \psi_{2,2}(x,y) = \psi_g(x)\,\varphi_g(y), \qquad (4.35)$$

$$\psi_{1,3}(x,y) = \psi_h(x)\,\psi_h(y) \qquad \psi_{2,3}(x,y) = \psi_g(x)\varphi_g(y), \qquad (4.36)$$

Where, φ is the scaling function while ψ, represents the wavelet function. $\psi_{1,i}$ represents the sub-bands of the real wavelet tree while $\psi_{2,i}$, represents the sub-bands of the imaginary tree. These can be combined to form the sub-bands of the 2-D CWT as follows:

$$\psi_i(x,y) = \frac{1}{\sqrt{2}}(\psi_{1,i}(x,y) - \psi_{2,i}(x,y)), \qquad (4.37)$$

$$\psi_{i+3}(x,y) = \frac{1}{\sqrt{2}}(\psi_{1,i}(x,y) + \psi_{2,i}(x,y)), \qquad (4.38)$$

The normalization by $1/\sqrt{2}$ is employed so that the sum and difference operation yields orthornormality. The six wavelet sub-bands of the 2D-CWT are strongly oriented at $\{+15^o, +45^o, +75^o, -15^o, -45^o, -75^o\}$ direction. Thus, the 2-D DT-CWT are only strongly oriented in six directions, it is also approximately analytic and also approximately shift invariant. Figure 4.9, shows the result of the iris sample decomposition using the 2-D DT-CWT. Notwithstanding the many advantages of the 2-D DT-CWT which we have emphasised before, it still have some shortcomings. The 2-D DT-CWT is not fully directionally selective compared to the Gabor wavelet transform. This can be improve using the proposed CWF. Also, the 2-D DT-CWT is only approximately shift invariant. These two properties are very important for high performance image representation. In other to achieve shift invariance and greater directionality, the principally rotated complex wavelet filters is designed.

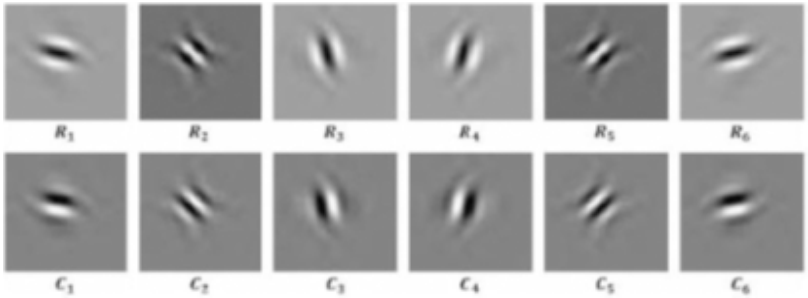

Figure 4.9: Sample showing the coefficients of the complex wavelet transform.

4.2.3 The Implementation of Proposed PR-CWF for Iris Features Extraction

In this section, the invariant iris feature is extracted using the rotated complex wavelet filterbank (R-CWF) proposed in this work. The normalized iris sample from Chapter 3, Section 3.5 is scale invariant which already accounts for the size inconsistencies normally caused by factors like pupil dilation and constriction. In order to compensate for eyelid/eyelash occlusions which is normally a problem with non-ideal iris images, the segmented iris region is divided into sectors and the upper and lower sectors are eliminated as shown in Figure 4.12. The rotation of the CWF is performed on the filters instead of the iris sample to achieve greater orientation selectivity and maintain shift invariance of the extracted iris features.

The normalized iris sample $N(i,j)$ such as shown in Figure 4.12c is first converted to binary image and the principal texture direction is computed using the procedure discussed in section 4.2.1. Once, the principal texture direction θ has been determined, the complex wavelet filters (CWF) discussed in section 4.2.2 is then rotated in the principal direction θ for the decomposition of the image and later in the opposite direction $-\theta$ for a repeat decomposition again. In [82], Kokare et al. implemented the rotation of the 2-D CWT filters by 45^o in order to extract the rich iris feature which he named the 2-D Rotated Complex Wavelet Filters (RCWF). This had the ability of achieving strong orientations in 12 directions which is higher than the standard 2-D DT-CWT. However, since greater textural information is always available in the direction of the principal texture, we have chosen to rotate the filter in the principal direction. The approach using a new set of filters retains the othorgonality property of the CWT because it able to satisfy the Hilbert transforms condition given as:

$$\frac{1}{2\pi}\int_{-\infty}^{\infty} H_i(\omega)\ \overline{H_j(\omega)}d\omega = 0, (i \neq j), \qquad (4.39)$$

Where $H_i(\omega)$ is the Fourier transform of the 2-D filter. In this work, we have adopted a new computationally more efficient method based on rotation of the filter sub-bands in the direction of the principal texture in order to more distinctive features. The oriented and approximate rotated complex wavelet filterbank can be obtained by using the various sub-bands of the CWT, without designing a new set of filters. This is because once the angle difference between the individual filters are maintain, the condition of

othorgonality is also maintained when the filters are rotated as a set as shown in Figure 4.13.

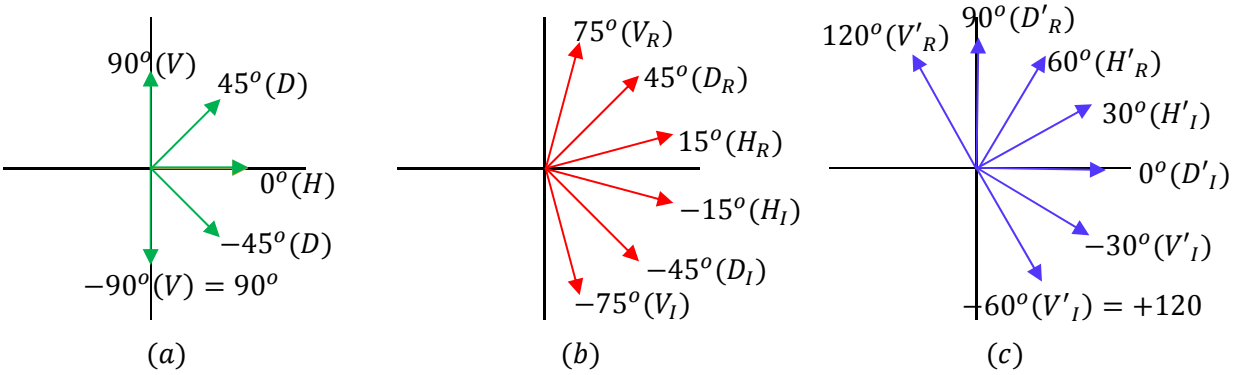

Figure 4.10: Orientations of the wavelet sub-bands: (a) orientations of DWT sub-bands, (b) orientations of CWT sub-bands and (c) the orientations of an example PR-CWF at angle an of $\theta = 45^o$.

The twelve sub-band components of the principally rotated complex wavelet filterbank (PR-CWF) are derived by approximation of the six sub-bands components of the CWT whereas, that six sub-band components of the CWT are derived from the three basic sub-band components of the two DWTs by simple approximations as discussed earlier in Section 4.5. For instance, the $\pm 15^o$ are the horizontal components of the real and imaginary trees of the CWT and these are also considered as the approximation of the horizontal component (0^o) of the basic DWT. Likewise, the vertical ($\pm 75^o$) and diagonal ($\pm 45^o$) components of the CWT are also the vertical (90^o) and diagonal (45^o) components of the DWT as shown in Figure 4.10. The same rules have been adopted to find the components of the (PR-CWF) from the components of CWT. Table 4.1 shows the mapping of the six components of the PR-CWF and the opposite of the PR-CWF.

Components of PR-CWF	**Components of the –PR-CWF**
Real horizontal component	Real vertical component (RV)
Real vertical component	Imaginary vertical component (IV)
Real diagonal component	Real Horizontal component (RH)
Imaginary horizontal component	Real diagonal component (RD)
Imaginary vertical component	Imaginary diagonal component (ID)
Imaginary diagonal component	Imaginary horizontal component (IH)

Table 4.1: Mapping of the sub-band components of PR-CWF and -PR-CWF.

Therefore, the six sub-bands of the PR-CWF in terms of the horizontal, vertical and diagonal components of the real and imaginary trees of the CWT are computed using Table 4.1 and Equation (40), which are given as:

$$
\begin{aligned}
Ist\ sub-band\ of\ PR-CWF &= 1/\sqrt{2}(RV-RD)\\
2st\ sub-band\ of\ PR-CWF &= 1/\sqrt{2}(RV+RD)\\
3st\ sub-band\ of\ PR-CWF &= 1/\sqrt{2}(IV-ID)\\
4st\ sub-band\ of\ PR-CWF &= 1/\sqrt{2}(IV+ID)\\
5st\ sub-band\ of\ PR-CWF &= 1/\sqrt{2}(RV-IH)\\
6st\ sub-band\ of\ PR-CWF &= 1/\sqrt{2}(RV+IH), \qquad (40)
\end{aligned}
$$

These sub-bands are approximately the rotated version of the sub-bands of CWT which are now strongly oriented in $\{+60^o, +90^o, +120^o(-60^o), -30^o, 0^o, -30^o\}$ as shown in the example rotation of Figure 4.10. Therefore, the combination of the features of the PR-CWF rotated in the principal direction θ and in the opposite direction of $-\theta$, forms the coefficients of feature vectors in 12 directions. Hence the method is computationally more efficient compared to Gabor filters normally used for the same kind of computation.

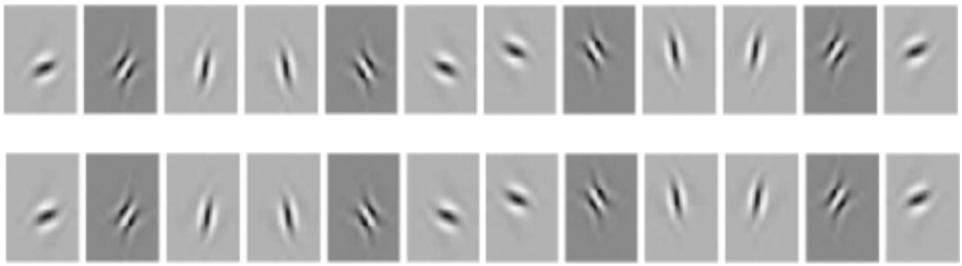

Figure 4.11: The coefficients of the iris sample decomposed using the proposed PR-CWF.

Hence, the decomposition of the image using PR-CWF produces 12 sub-samples image coefficients oriented in different directions instead of six achieved using 2-D DT-CWT. The decomposition is performed till level 3 and a total of 12 multiplied by 3 sub-images are produced.

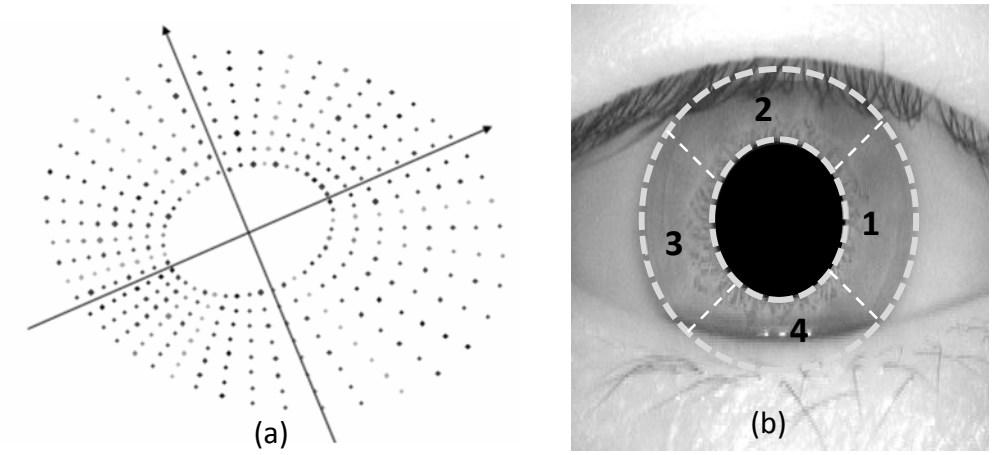

Figure 4.12: Sub-sampled iris normalization, (a) a description of the iris portion of the image, (b) iris image with mapped sectors

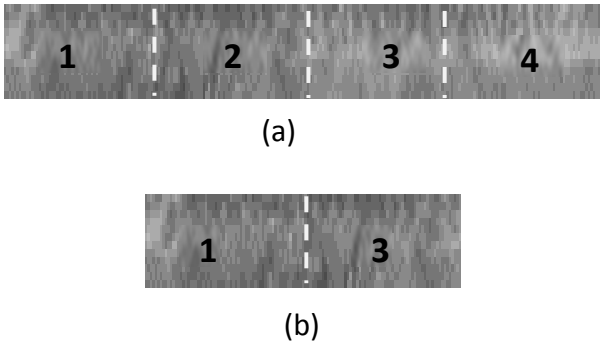

Figure 4.13: Normalized sub-sample of the iris image; (a) normalized iris image showing the sectors, (b) final normalized iris image with some sectors eliminated

The extracted features using the proposed method compensates for the limited orientation selectivity of the standard 2-D DT-CWT. Therefore, we are able to extract rotation and scale invariant features of the iris. The proposed method is also computationally more efficient and effective compared to other popular approach for iris feature extraction like Gabor wavelets and DWT.

4.3 Iris Feature Selection Using Modified PSO

The iris sample contains a huge number of features and a comparatively small number of samples per class, and this makes accurate and fast classification or recognition difficult [37]. Some researcher have made great efforts aimed at solving this problem. Chen et al. [40], proposed a method based on the selection of edge-type features for iris recognition, and AdaBoost algorithm was then used to select a filter bank from a pile of

filter candidates. In [41], the authors applied a feature correlation evaluation approach for iris image quality measure. This approach was able to discriminate the artificial patterns from the natural iris patterns and it could also be able to measure iris image quality for uncompressed images. In [42], the portions of the iris with the most distinguishable changing patterns were chosen and used to measure the feature information. Proenca and Alexandre [46], proposed a method to measure the quality of each feature in the extracted feature sequence and separate them into two sets: noisy features and noise-free features. The similarity between the two sets was then measured and used to discover the identity of a specific subject.

In this research effort, we propose apply a modified particle swam optimization (PSO) in order to select the most prominent iris features and based on this information, a matching computation is performed using adaptive SVMs [55]. The PSO is a population based stochastic optimization technique developed by Kennedy and Eberhart [55] and modelled after the social behaviour of bird flocks. It was developed as an improvement of the GA and Ant Colony Algorithms. In PSO, each particle represents a potential solution to the optimization problem. Initially, each particle is assigned a randomized velocity, and is allowed to determine the direction and distance of the movement within the problem space in order to find optimal solution. Each particle keeps track of the following information about the problem space: the current position of the particle x_i, the current velocity of the particle v_i, the best position of the particle. The best position yields the best fitness value for that particle. The fitness value of the position is called *pbest* while the fitness value of the entire particles is called *gbest*.

The PSO produces the particles of the initial population randomly and the evolutionary computation is used to find the optimal solution for the function. In each evolution, the particle would change the individual's search direction based on two search memories. The first memory search is the optimal individual's variable memory pbest and the other is the optimal variable memory of the entire population gbest. After the computation, the PSO would calculate the optimal solution according to the optimal variable memory.

Given an iris feature vector pool S, the position of a particle s is given as $S_i = (s_{i,1}, s_{i,2}, s_{i,3}, \dots\dots, s_{i,N})^T$, and the velocity $V_i = (v_{i,1}, v_{i,2}, v_{i,3}, \dots\dots, v_{i,N})^T$. The particle's flight experience is given as $P_i = (p_{i,1}, p_{i,2}, p_{i,3}, \dots\dots, p_{i,N})$ which is regarded as the *pbest* and the group experience is $G_i = (\mathrm{g}_{i,1}, \mathrm{g}_{i,2}, \mathrm{g}_{i,3}, \dots\dots, \mathrm{g}_{i,N})$ which is also regarded as the *gbest*. The particle is able to determine the next movement through their own experience

$pbest$ and the group experience of the entire population g$best$. For the $k+1th$ iteration, each particle of PSO changes position according to the following equations:

$$V_{i,j}^{k+1}(t,1) = \omega V_{i,j}^{k} + c1r1 * \left(P_{lbest} - s_{i,j}^{k}\right) + c2r2 * \left(P_{\mathrm{g}best} - s_{i,j}^{k}\right), \quad (4.41)$$

$$s_{i,j}^{k+1} = s_{i,j}^{k} + v_{i,j}^{k+1}, \quad (4.42)$$

Where $i = 1,2,\dots\dots,M$ and M is the number of particles; $V_{i,j}^{k}$ is the dth dimensional component of the kth iteration, the velocity vector of the particle s, and $s_{i,j}^{k}$ is the dth iteration dimensional component of the kth iteration of the position vector of particle s. $pbest$ is the dth dimensional component of the best position of an individual particle s, and g$best$ is the dth dimensional component of the best position of the group . $c1, c2$ are the positive acceleration constants, whereas $r1, r2$ are uniformly distributed random numbers between 0 and 1, and ω is the inertia weight between [0,1] which provides a balance between global and local search abilities of the algorithm.

4.4 Modified PSO for Optimized SVM Classification

Support vector machine (SVM) [55], is a new learning methodology proposed by Vapnik et al. [118], which finds optimal separating hyperplane in a high dimensional feature space. It uses a linear hyperplane to create a classifier with a maximum margin [119]. The algorithm aims to find support vectors and their corresponding co-efficients to construct an optimal separating surface by the use of kernel function in dimensional feature space [119]. SVM which is considered a good candidate for learning in image retrieval that has a strong theoretical foundation and has been used for object recognition, text classification etc. SVM was originally designed for binary classification but can be applied for multi-class problems.

Now, given a training data set $\{x_i, y_i\}$ representing vectors in a space $X \subseteq R_d$belonging to two separate classes with their labels $y_i \in \{-1,1\}$. The aim is to find a hyperplane $\omega x + b = 0$ which separates the data which is given as $\mathrm{g}(x) = \omega x + b$. Amon many possible hyperplanes, the optimal hyperplace (OSP) is the hyperplane which maximizes the margin (the distance between the hyperplane and the nearest data point of each class). After normalization of g(x), OSP can be computed as the minimization of $\|\omega\|$ which is given as follows:

$$\min \quad \emptyset(\omega) = \frac{1}{2}\|\omega\|^2, \qquad (4.43)$$

$$s.t. \qquad y_i(\omega \cdot s_i + b) - 1 \geq 0, \qquad i = 1,2, \ldots\ldots, N$$

Then, defining N langragians α_i, $i = 1, \ldots\ldots, N$. After solving the quadratic optimization problem, we get the best hyperplane, which $\omega = \sum_{i=1}^{N} \alpha_i \cdot y_i \cdot X_i x_i$ is the support vector, which refer to the training samples that lie closest to the hyperplane. The vectors lying on one side of the hyperplane are labelled as -1 and those laying on the other side of the hyperplane are labelled as +1. The classification function is given by

$$f(x) = sign(\sum_{i=1}^{N} \alpha_i \cdot y_i \cdot x_i + b), \qquad (4.44)$$

Now, for the iris image, the data cannot be linearly separated. Therefore, we use a kernel function to transform that data into a higher dimensional space. The classification foundation is then transformed to

$$f(x) = sign(\sum_{i=1}^{N} \alpha_i \,.\, y_i \,.\, K(x_i, x) + b), \quad (4.45)$$

The SVM is trained using the RBF kernel which can be given as

$$K(x_i, x) = \exp\left(\frac{(x_i - x)^2}{\sigma^2}\right), \qquad (4.46)$$

To train the data samples, the normalized iris image is decomposed into twelve bandpass oriented subbands at each scale using the dual tree PR-CWF. The decompositions was done recursively to level three using the low-low pass residual image. The decomposition gives a total of 12×3 subband images. The total of 36 subband images that was generated are then used as samples for the PSO feature selection process. The feature selection and classification are achieved in the following steps:

Step 1. The initialization of the PSO is set to $s = 1$, $F_1^{pbest} = F_2^{pbest} = \cdots = F_N^{pbest} = 0$. The number of particles N, the number of iteration G, and the four parameters $C_1, C_2, \gamma_{max}, \gamma_{min}$ are all given.

Step 2. The initial velocity $V_i = (v_{i,1}, v_{i,2}, v_{i,3}, \ldots\ldots, v_{i,N})^T$ and the initial position $P_i = (p_{i,1}, p_{i,2}, p_{i,3}, \ldots\ldots, p_{i,N})$ of N particles are created.

Step 3. The fitness value of each particle in the gth iteration is calculated using (). The fitness function which is expressed by the reciprocal of the computation time is given as

$$F(P_h^g) = fit(P_h^g), \quad h = 1,2, \ldots\ldots, N, \qquad (4.47$$

Step 4. The best feature F_h^{pbest} and the best position P_h^{pbest} for each particle were determined as follows:

$$F_h^{pbest} = \begin{cases} F_h^g, & if\ F_h^{pbest} \leq F_h^g \\ F_h^{pbest}, & otherwise, \end{cases} \quad h \in \{1,2,\ldots..,N\}, \qquad (4.48)$$

$$P_h^{pbest} = \begin{cases} P_h^g, & if\ F_h^{pbest} \leq F_h^g \\ P_h^{pbest}, & otherwise, \end{cases} \quad h \in \{1,2,\ldots..,N\}, \qquad (4.49)$$

Where, P_h^{pbest} is the individual optimal fitness value F_h^{pbest} form the starting to the current generation.

Step 5. The index q of the particle with the highest fitness function is designed by

4.5 Summary

In this chapter, a novel iris feature extraction and selection technique has been presented. This method is capable of reducing the dimensionality of the iris feature code and speeding up the matching/classification step. Also the rotation of the CWF in the direction of the principal textures extracts important iris information that is rotation and shift and scale invariant.

Chapter five

5. EXPERIMENTAL RESULTS AND ANALYSIS

In this chapter, we present the results, and the analysis of the accuracy, performance and time efficiency of the proposed iris segmentation and feature extraction schemes. We have conducted some experiments to evaluate the performance of the proposed schemes and summarized the results in this chapter. The robustness of the proposed approach is also evaluated on non-ideal images from different heterogeneous iris image datasets. We also compared the performance of the proposed approach with some other state-of-the-art iris recognition algorithms in order to evaluate its efficacy. Section 5.1 briefly set out an introduction to the evaluation methods.

5.1 Introduction

We conduct extensive experiments using four selected iris datasets namely: UBIRIS v1, UBIRIS v2, CASIA Iris V1 and CASIA Iris V4 in order to ascertain the efficacy of the proposed methods. These iris datasets contains mainly heterogeneous images with varying degrees of noise and other artefacts. The detail description of the datasets are given in section 5. 5. The chosen databases are made up of ideal and non-ideal iris images captured under less constrained imaging environments which is ideal for our testing purpose. Experiments are carried out in two stages. The first stage, evaluates the performances and accuracies of the proposed segmentation, feature extraction and selection algorithms. In the second stage, the performances of the proposed algorithms are compared with other state-of-the-art iris recognition algorithms. A comparative analysis of our method with the other state-of-the-art methods are carried out to show the effectiveness of the proposed schemes. Experiments are carried out on the selected iris datasets to evaluate the performance of the proposed algorithms in both verification (one-to-one) and identification (one-to-many) modes.

The verification mode is able to assess the performance of the algorithms in terms of *genuine acceptance rate (GAR), false acceptance rate (FAR) and equal error rate (EER).* Similarly, the performance estimation in the identification mode is a one-to-many search of the entire dataset for a given test sample. The identification mode adopts a *correct recognition rate (CRR)* measure in order to evaluate the performance of the algorithm.

In the first stage, we focused on the performance evaluation of the proposed approach based on segmentation accuracy. Thereafter, we evaluate the performance of the proposed approach for iris segmentation, feature extraction, optimum feature selection and iris recognition using SVM. The verification performance of the proposed method is demonstrated using the receiver operating curve (ROC) curve and equal error rate (EER). As mentioned earlier in chapter 1, the EER is the point where the FAR and the FRR are equal in value. In earnest, the lower the EER value, the better the accuracy of the iris recognition system [17].

In the second stage, experiments are carried out to provide a comparative analysis of our method with the other existing methods with respect to the recognition accuracy. The average time consumption pertaining to the different parts of the proposed iris recognition system are computed and comparisons are drawn with other existing methods in order to ascertain the efficiency of the proposed method.

5.2 Experimental Setup

This section gives detailed information on the experimental setup used for conducting each analysis of the research.

5.2.1 Iris Image Database

In order to ascertain the efficiency of the proposed iris recognition scheme based on GCBAC for iris segmentation, PR-CWF and PSO for feature extraction and selection and SVM for classification, tests were performed on two free publicly available iris datasets: UBIRIS v2.0 and CASIA-IrisV4. For simplicity, four sub-sets of the datasets namely: UBIRIS v2.0, CASIA-Iris-Interval, CASIA-Iris-Lamp, and CASIA-Iris-

Distance were selected. All of the four iris image datasets selected contain challenging iris images obtained under less constrained imaging conditions. This criteria meets the main objectives of our experimentation since images acquired under less constrained imaging conditions tends to contain high level of noise which makes it more challenging to recognise that others.

The UBIRIS v2.0 iris dataset which have been extensively used for many research evaluations was released by University of Beira, Portugal in 2010 [103]. It includes 11,102 non-ideal iris images from 522 irises captured from 261 subjects in two distinct sessions [105]. The development of this database was aimed at improving the UBIRIS v1.0 database by capturing real life iris images on-the move or at-a-distance, in visible wavelength with less subject co-operation. This database is normally classified as difficult for iris segmentation purpose [103]. The captured iris images in this database were classified into three categories: "light", "medium"' and "heavy" pigmented. The "light" pigmented category contains the blue and light green iris images with the highest luminance value average $\mu\gamma$ and standard deviation $\sigma\gamma$ values of 51.95 and 3.90, respectively. The "medium" contains the light and medium brown and dark green irises with $\mu\gamma = 37.70$ and $\sigma\gamma = 3.15$, while, the "heavy" pigmented iris images contains dark brown and almost black irises with $\mu\gamma = 29.46$ and $\sigma\gamma = 2.25$, respectively.

The image acquisition was implemented under both artificial and natural lightning sources. Images were captured within two weeks in two distinct imaging sessions with an interval of one week. The subjects were made up of about 90% of mainly Latin Caucasian, 8% Black Africans, and 2% percent Asian people. About 60% of the subjects were able to participate in the two imaging sessions. While, about 40% of the participants performed exclusively in one session, either during the first or second capture session. The images were captured at a distance of between 4 to 8 meters from the camera and a total of 15 images per eye and session were capture from a large majority of the individuals. This is one of the major distinguishing point between this database and other iris image databases. UBIRIS v2.0 images are captured using visible imaging and the images are 24-bit colour images in TIFF format with a resolution of 800×600 bits. There are 14 different noise factors identified in this database which include: iris obstruction, reflections, off-angle, partial image, poor focus, motion blur, rotated, improper lightning and out-of-focus iris images to mention but a few.

The CASIA-IrisV4 iris dataset [104] was recently released by the Institute of Automation, Chinese Academy of Sciences as an extension of CASIA-IrisV3 iris dataset. It contains a total of 54,601 iris images captured from more than 1,800 genuine subjects and about 1,000 virtual subjects. All the images are captured under near infrared illumination or synthesized to an 8-bits gray-level JPEG file format. The images were captured at a distance from the subject. Therefore, it contains many poor images with so many challenges like: heavy occlusion, poor contrast, pupil deformation, e.t.c. CASIA iris database is the largest iris image database in the public domain till today by our best judgement.

CASIA-IrisV4 contain six subsets, three of which are from CASIA-IrisV3 dataset which includes: CASIA-Iris-Interval, CASIA-Iris-Lamp, and CASIA-Iris-Twins. The remaining three new subsets include: CASIA-Iris-Distance, CASIA-Iris-Thousand, and CASIA-Iris-Syn, respectively. The CASIA-Iris-Interval images were captured with a self-developed closed-up iris camera. The camera is designed to use a circular NIR LED array, with suitable luminosity flux to capture iris images. The iris image captured using this design is very clear. Similarly, CASIA-Iris-Lamp images were captured using a handheld iris sensor designed by OKI. The infrared light is turned on/off close to the subject in order to introduce more intra-class variations during capture. The mechanism produces elastic deformation of iris texture due to pupil expansion and contraction under different illumination conditions which is one of the major challenges of iris segmentation. This database provides good sample iris images for studying non-uniform iris normalization and robust iris feature representation. CASIA-Iris-Twins in the same way contains iris images of 100 pairs of twins, collected using OKI IRISPASS-h camera.

CASIA-Iris-Distance contains iris images captured using a self-developed long range multi-modal biometric image acquisition and recognition system. A biometric sensor is used to identify subjects from a 3-meter distance by actively searching for iris or face pattern in the visual field via intelligent multi-camera imaging system. Also, CASIA-Iris-Thousand contains 20,000 iris images from 1,000 subjects, captured using IKEMB-100 camera produced by Irisking. Subject are meant to look into the camera's LCD and adjust their pose for fit into the bounding box for high quality iris capture. Finally, CASIA-Iris-Sync contains 10,000 synthesized iris images of 1,000 classes. The iris textures of these images are synthesized automatically from a subset of CASIA-IrisV1 dataset. These are artificial iris images developed by embedding iris ring regions into real iris images to make them look more realistic. The intra-class variations introduced into

the synthesized iris dataset include, blurring and rotation which raises a challenge for iris feature extraction and matching.

The two iris datasets used in this experiment were acquired at a distance ranging from 3 to 8m, which justifies one of the main objective of this research. Also, CASIA iris database was acquired from subjects of mainly Chinese and Asian origin while UBIRIS database images were acquired from a mixture of subjects where majority of about 90% are mainly of Latin Caucasian origin, 8% of whom are of black origin, and 2% are of Asian origin, respectively. Therefore this satisfies the versatility and diversity of subjects as well as the heterogeneity in the iris samples used in this experiments which is a major objective of this study.

5.2.2 Evaluation Framework of the Proposed Schemes

To validate the performance of the proposed segmentation algorithm, we perform experiments on the four selected datasets as well as on a combined dataset built from iris images from all the different versions of UBIRIS and CASIA iris datasets. In the first phase of the evaluation, each iris image in the considered test database is processed using the proposed segmentation, feature extraction and matching algorithm and based on the matching and classification results, evaluations are made. In order to detect the specular reflections in the original iris image, the iris image is first processed with the proposed multiscale adaptive edge-weighted high-pass fitter for reflection mapping. The mapped reflection points are then removed using the proposed modified exemplar based image inpainting. The boundaries of the iris are then localized using the proposed GCBAC. Normalization of the iris sample is achieved using Daugman's rubber sheet model [8], [11]. Distinctive iris features are then extracted and encoded using the proposed PR-CWF and PSO. Subsequently, classification using adaptive support vector machine (ASVM) is performed. Once, the iris images are encoded, identical template matching is performed to generate the genuine and impostor matching distributions.

In order to determine the accuracy of our iris recognition algorithm, various experiments were carried out on the dataset which include; manual observation, and automatic performance analysis methods. Performance evaluation is carried out after template matching is performed to generate the genuine and impostor matching distributions. Based on this distribution, Receivers Operating Characteristics (ROC)

curves are used to measure the performance of the algorithm. The ROC plot for each algorithm is given as the plot of the Genuine Accept Rate (GAR) against the False Acceptance Rate (FRR). Also, the Equal Error Rate (EER) is used to give the quantitative evaluation of the algorithm. EER is a point in the ROC curve where the FAR and FRR are equal, and the smaller the value of EER is, the better the algorithm.

For the computation of the verification rates namely FRR and FAR and GMR, the following formulas were used:

Let φ_g represent the set of all genuine comparison score,

and φ_i represent the set of all imposter comparison score.

$\varphi_g(t)$ is the set of all gunine socres $s > t$,

$\varphi_i(t)$ is the set of all imposter scores $s > t$

$$GMR(t) = \frac{\|\varphi_g(t)\|}{\|\varphi_g\|}, \qquad (5.1)$$

$$FAR(t) = \frac{\|\varphi_i(t)\|}{\|\varphi_i\|}, \qquad (5.2)$$

$$FRR(t) = 1 - GMR(t), \qquad (5.3)$$

Where t represents the threshold. False acceptance rate (FRR), is one of the most important indicators of the security level of biometric system, which is completely determined by the imposter distribution.

5.2.3 Implementation Details and Experimental Results

Our experiments were performed on images from the UBIRIS v2.0, and CASIA-Iris-Interval, CASIA-Iris-Lamp, CASIA-Iris-Distance and a combined iris dataset from all the different datasets. After pre-processing and feature extraction, the images was trained using the hybrid PSO based SVM models for efficient classification.

The pre-processing includes five steps from the iris segmentation to the representation of the iris sample using the binary iris code. The steps includes:

- Reflection detection and removal – detects and fills the reflected parts of the original iris image.
- Iris segmentation – effectively defined the boundaries of the iris portion of the image.
- Normalization – transforms the segmented iris sample from the radial co-ordinate system to the rectangular polar co-ordinate system in order to maintain size/translation invariance.
- Feature extraction – the analysis if the iris sample for iris representation.
- Feature selection- the representation of the iris sample by selection of best iris features.

Using the pre-processing steps, we avoid the undesirable effects of occlusions and non-uniform illumination as well as erroneous segmentations which might affect the recognition quality.

To evaluate the performance of the algorithms, several measures were deployed in our work. 10-fold cross-validation is the standard way of measuring the accuracy of a learning scheme on a particular dataset. The datasets are divided randomly into 10 parts where the class is represented with approximately the same properties as full dataset. During each run, we use different sets of images for training and testing in the classification algorithm in order to ascertain the performance of our proposed methods. For UBIRIS v2.0 dataset, a total of 5 images per subject out of the 15 images per subject per eye was chosen randomly for training while the rest of the images from the dataset were used for testing. Also, for CASIA-Iris-Interval, CASIA-Iris-Lamp, CASIA-Iris-Distance and the combined subsets, a total of three images per subject were chosen for training while the rest of the images in the dataset were used for testing purposes. These sets are non-overlapping which means no subject is used for training purpose was used for testing. Classifier performance is evaluated by calculating the ratio of the number of correctly classified instances to the total number of instances (Accuracy).

It is important to find the optimal parameter C and gamma for each particular parameter setup because different parameter setup are suitable for solving different problems. We employ algorithm PSO for fixing the parameters W, c1 and c2 with the values set as W=0.75, c1=c2=1.5 and number its particles with 30, whereas the iteration count is 100. As regards to topology vicinity, we chose a vicinity ‘gbest’ which ensures

that it converges faster that the model ‘lbest’. The selected iris feature code (irisCode) based on particle swam optimisation is feed directly into the ASVM for iris recognition.

All the experiments were run on a standard Pentium IV 3.40GHZ with 16.0GB memory running the Windows 7 Enterprise operating system. We compare the results obtained with the PSO-SVM model with other state of the algorithm for performance verification considered by using the approach of multiclass and one-vs-one. The results of the experiments are presented in subsequent sections.

5.3 Accuracy of the Reflection Detection and Removal Scheme

In this section, we evaluate the efficiency of the proposed reflection removal methodology on images of CASIA V4.0 iris image database. The whole of the images in CASIA V4.0 (interval and lamp) database were processed with the proposed reflection detection and removal algorithm based on edge-weighted high-pass filter and exemplar image inpainting method. Figure 5.1, shows the result of the reflection removal algorithm on some selected iris images from CASIA-Iris-V4-Lamp and CASIA-Iris-V4-Interval.

Evaluation using manual observation approach shows that more than 99 percent of reflections in the selected datasets were successfully detected and accurately filled. From the results shown in Figure 5.1, we can see that both the strong and weak reflections were accurately detected and filled and edges were preserved. Moreover, the detection algorithm made sure that only reflection points are detected and filled thereby preserving the iris structure for further processing.

Accurate reflection detection and removal paves way for effective pupil and limbic boundary segmentation. Also, it is very important that the method of filling the reflections in the iris image preserves the original structure of the image as much as possible so that further processing steps can be successfully carried out on the image.

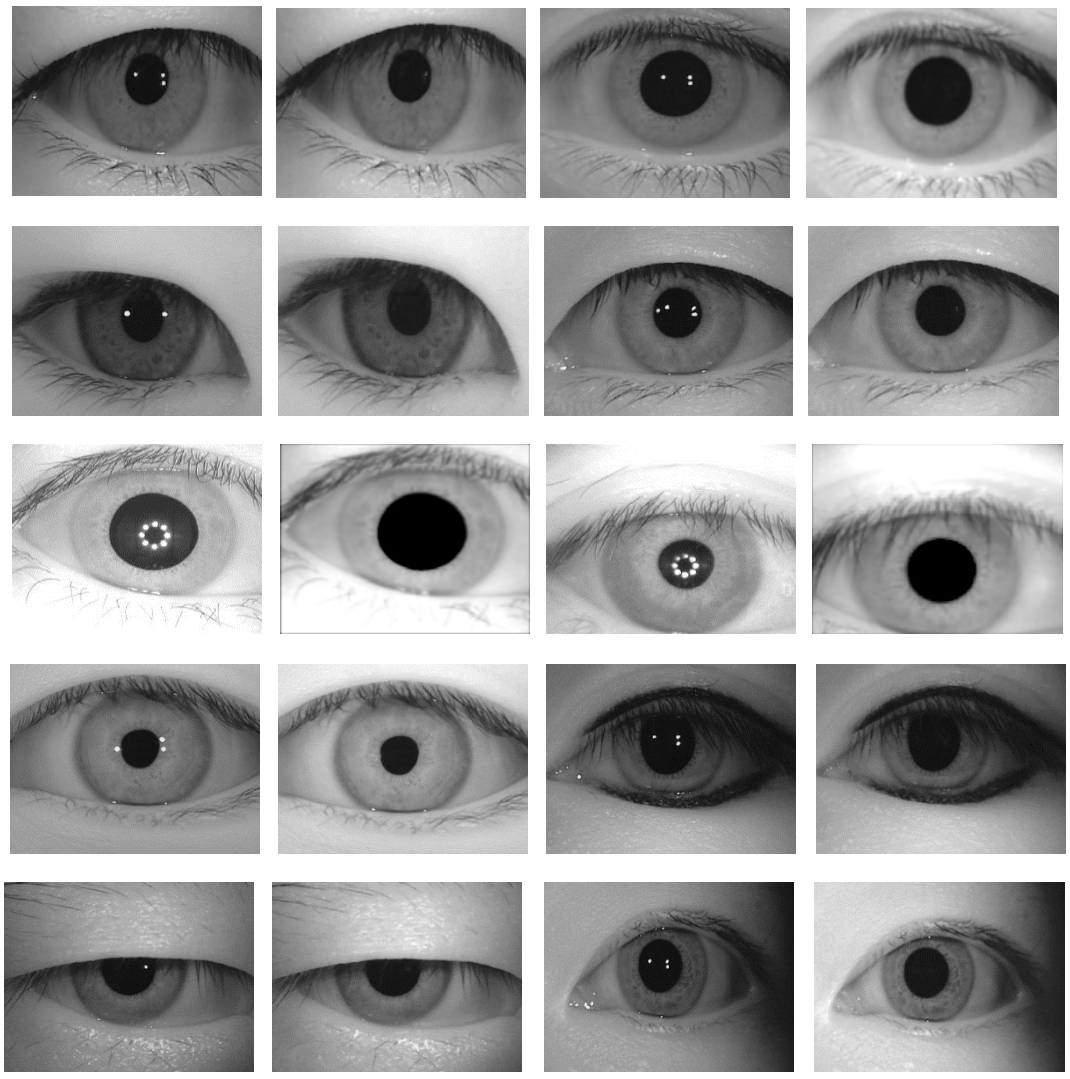

(a) (b)

Figure 5.1: Results of the reflection removal algorithm on challenging iris images from both CASIA and UBIRIS datasets using the proposed reflection detection and removal algorithm; images to the left of Columns (a) and (b) are the original iris images while the ones to the right of the columns (a) and (b) are the processed iris images

In this work, the level of alteration to the iris structure after reflection removal is computed and compared to other popular methods in order to demonstrate the efficacy of the proposed method in preserving the original structure of the image. To evaluate the level of preservation of the structure of the iris after inpainting, a method based on the calculation of Structural Similarity Index (SSIM) and the Mean Squared Error (MSE) of the original and the inpainted images is adopted. Figure 5.2, shows the SSIMs of the proposed method in comparison with other well-known popular reflection removal

methods and our proposed method recorded the lowest SSIM index while maintaining zero MSE.

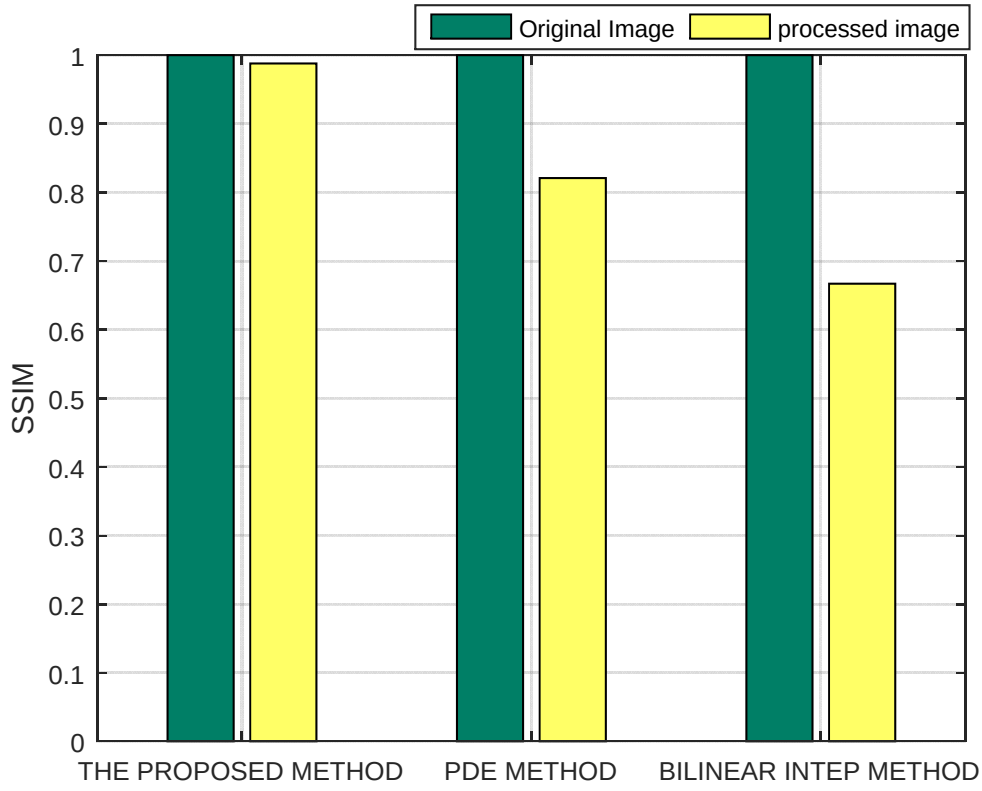

Figure 5.2: A bar plot showing the SSIM indexes of the original iris images before reflection removal against the equivalent processed iris images using the proposed reflection removal algorithm, the PDE method and the bilinear interpolation method on the combined iris image dataset, comparing the impact of each algorithm on the iris image structure.

This indicates that our method is better than the other methods in terms of accuracy and also in preserving the original structure of the image after removing reflection.

5.4 Evaluation of the Pupil/Iris Segmentation Scheme

To validate the performance of the proposed iris segmentation scheme, several experiments were carried out on the selected datasets. A number of different segmentation approaches were applied to segment the iris images. The iris images are segmented using active contour based on Shah and Ross method [53], Roy et al method [54], Daugman's

IDO method [17] and our proposed GCBAC method. Our proposed feature extraction and classification algorithms were applied for the iris recognition process in all the four different methods. In order to maintain the same standard in the evaluation scheme, the proposed reflection detection and removal method was applied to detect and remove reflection from the iris images before segmentation is carried out in some models where reflection detection and removal does not already exists. For instance, the Daugman's method does not include a reflection detection algorithm. Also, the proposed eyelash detection is applied where they do not already exist. These additional procedures increased the processing times for those approaches where they were applied but that also increased their performances as well. To provide numerical results and evaluate the performance of the proposed approach, the ROC curve framework is adopted. Also manual visual evaluation and comparison are used to evaluate the performance of the proposed approach. A sample of five test images each from the CASIA-Iris-V1.0 and CASIA-Iris-V4-Lamp representing ideal and non-ideal iris images, respectively have been selected to compare the efficacy of proposed segmentation scheme with other state-of-the-art active contour based segmentation algorithms on both ideal and non-ideal iris images. Figure 5.3, shows the segmentation results.

As shown in the first four images of Figure 5.3, all the approaches including the proposed approach achieved a satisfactory visual segmentation result for the first four images representing ideal iris images. However, for the last four non-ideal iris images, the proposed approach achieved a better visual segmentation result compared to the other approaches.

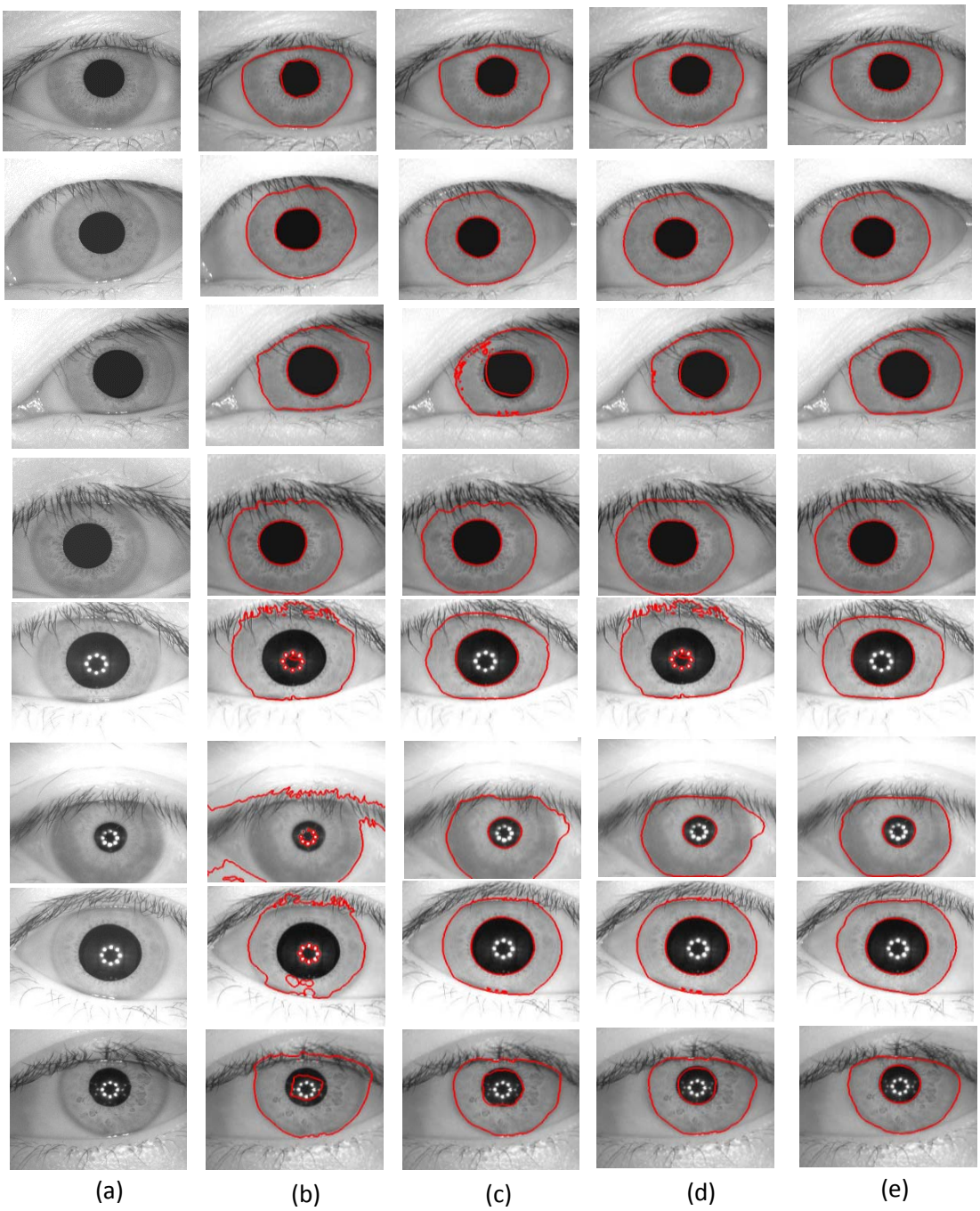

Figure 5.3: Visual comparison of the segmentation results of the proposed algorithm and other state-of-the-art algorithms on some selected images from CASIA iris dataset, (a) original iris image, (b)-(d) Results from [51-54], respectively, (e) Results for our segmentation approach.

Also, we show the results of the proposed algorithm on several challenging iris datasets. Figures 5.4-5.6 shows the segmentation results on CASIA-V4-Interval, CASIA-V4-Lamp and CASIA-V4-Twins, respectively.

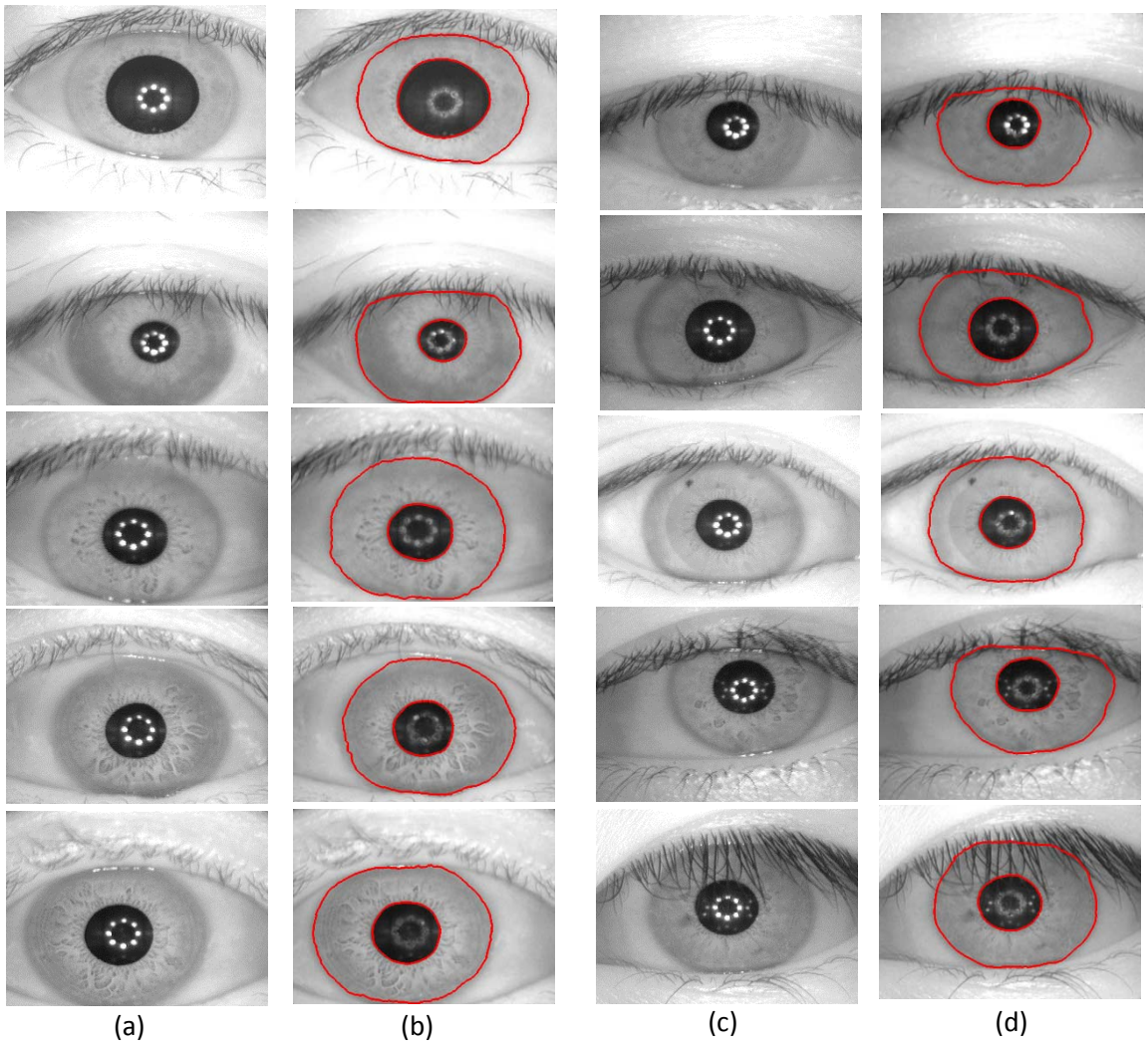

Figure 5.4: GCBAC segmentation results on non-ideal iris images from CASIA-Iris-V4-Interval dataset, columns (a) and (c) are the original iris image, columns (b) and (d) are the results of the segmentation process.

The visual results of the segmentation algorithms on CASIA Iris V4-Interval iris image subset is very impressing. The prevalent noise on this iris image subset is the presence of reflection and hue saturation. The impressive result on this subset shows that the proposed segmentation algorithm is able to overcome outliers which normally influence active contour based methods.

Similarly, Figure 5.5 displays the results of the proposed segmentation algorithms on the CASIA Iris V4-Lamp subset. The images of CASIA Iris V4-Lamp suffer from heavy occlusions and specular reflections as well. Also, as a result of the heavy occlusions, the boundaries of the iris are clearly non-circular in these images. However, the proposed segmentation algorithms still achieved good results. This goes a long way to show the power of active contour side of the algorithm in tracing irregular boundaries.

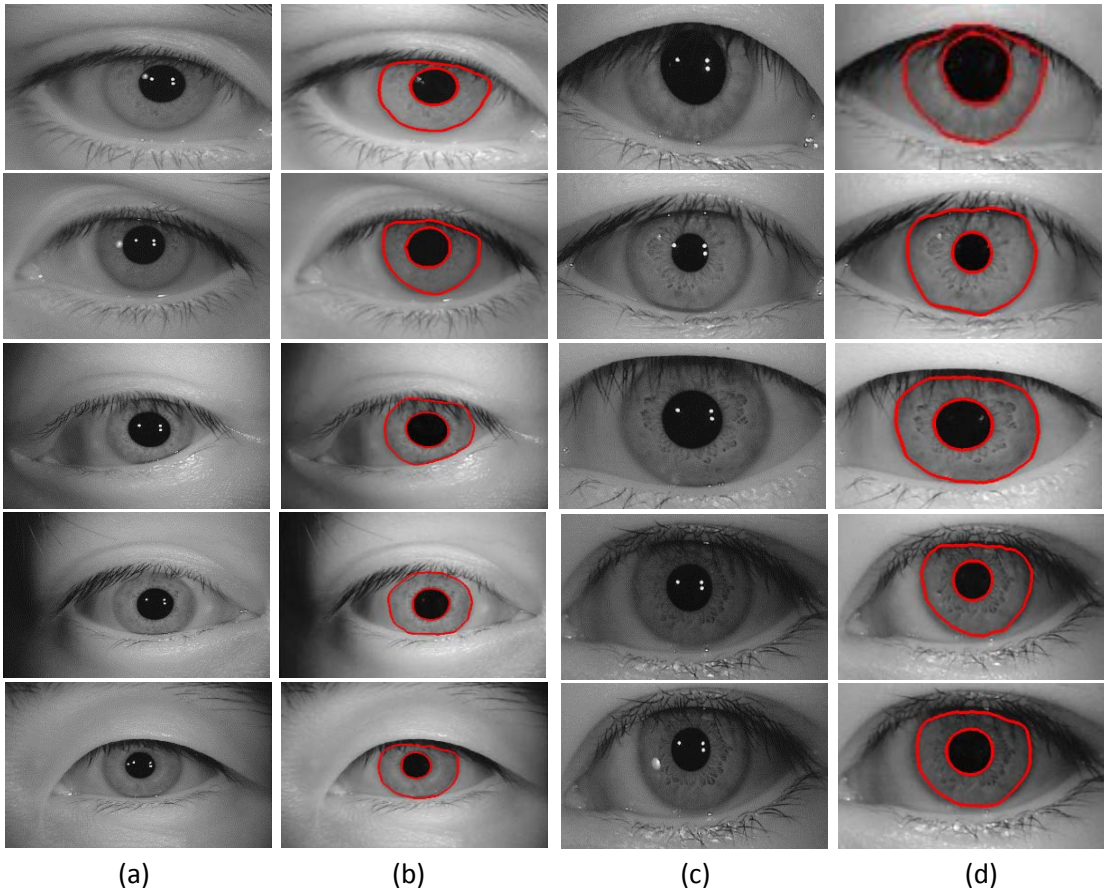

Figure 5.5: GCBAC segmentation results on non-ideal iris images from CASIA-Iris-V4-Lamp, columns (a) and (c) are the original iris image, columns (b) and (d) are the results of the segmentation process.

Also, as can be deduced from the displayed images, the images of this subset suffer from poor illumination. However, the segmentation algorithm is able to enhance the image and the accurate boundary of the iris are easier to detect from the enhanced image.

Lastly, the images shown in Figure 5.6 are taken from the CASIA Iris V4-Distance subset. They are heavily occluded and with poor illumination. They also suffer from specular reflections. Also, as with other subsets, the proposed segmentation algorithm was able to achieve good visual segmentation results on these images even with heavy occlusion and irregular shapes.

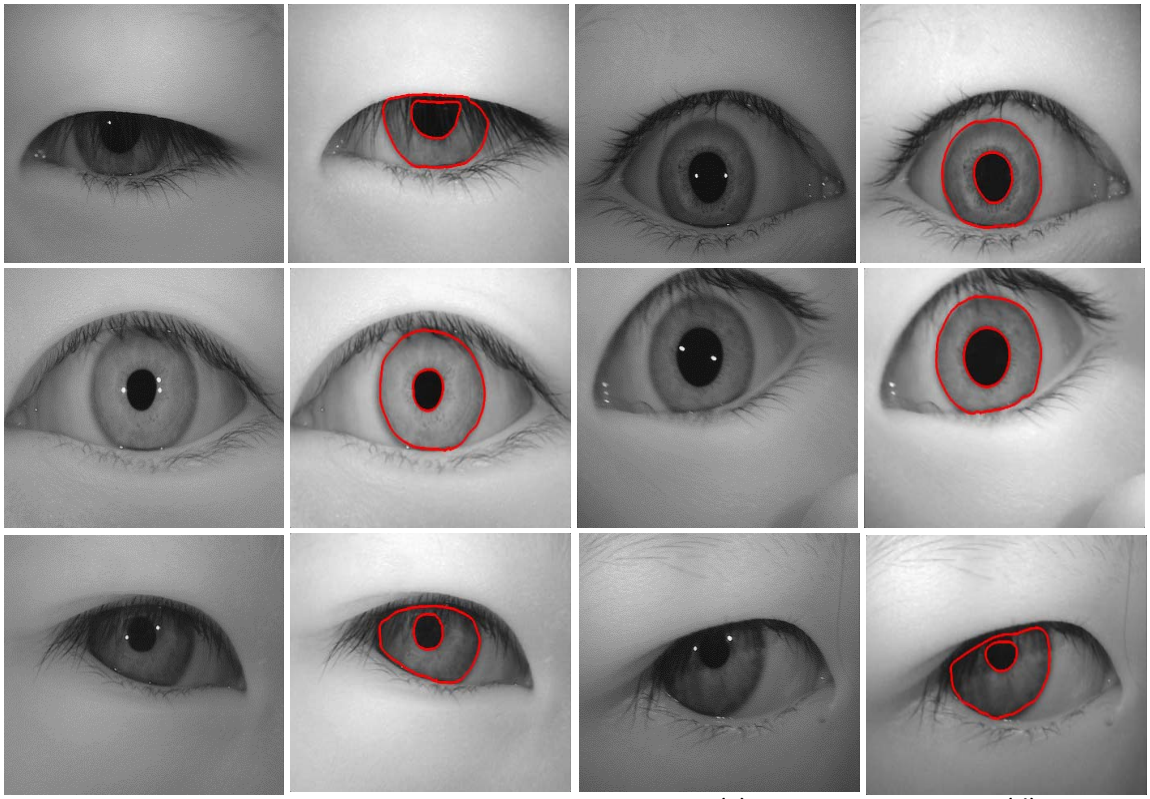

Figure 5.6: GCBAC segmentation results on challenging non-ideal iris images from CASIA-Iris-V4-Twin dataset, columns (a) and (c) are the original iris image, columns (b) and (d) are the results of the segmentation algorithm.

In the same vain, we experimentally analyse the performance of the proposed iris segmentation algorithm to ascertain the efficacy of the method. The experiments were carried out as discussed in Sections 5.2.2 and 5.2.3. Figures 5.7 – Figure 5.11 shows the ROC curves of the proposed GCBAC iris segmentation algorithm compared with other current state-of-the-art iris segmentation algorithms.

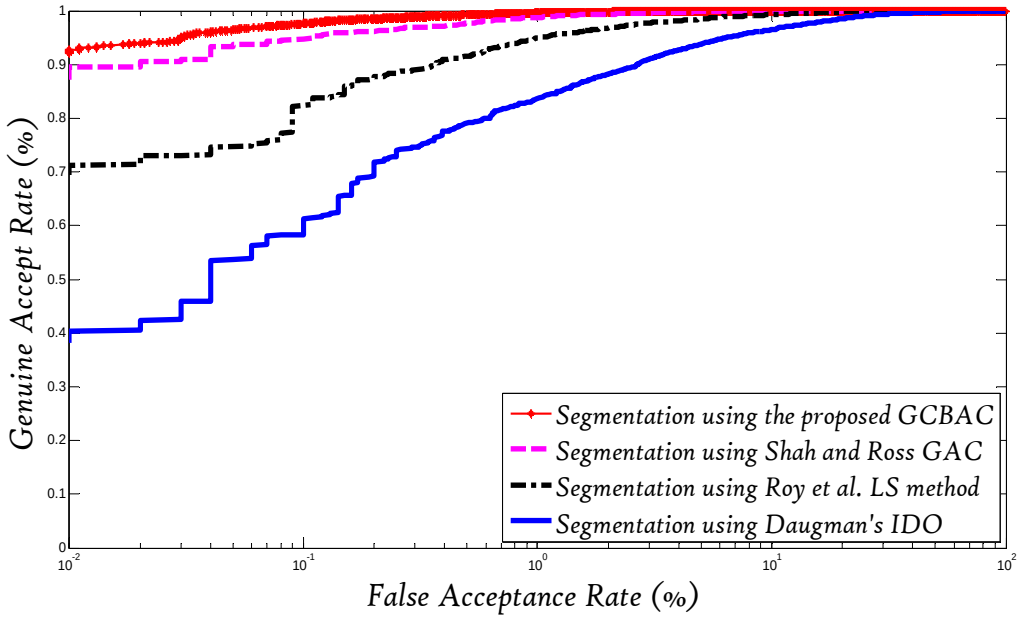

Figure 5.7: ROC curves showing the performance of the proposed GCBAC segmentation technique compared with other state-of-the-art segmentation algorithms [51-53], on CASIA Iris V4-Interval subset.

From Figure 5.7, we can see that the proposed GCBAC outperformed other state of the art iris segmentation algorithms on the CASIA Iris V4-Interval. The iris images of the CASIA Iris V4-Interval contains clear iris images with challenges like reflections, hue saturations, occlusions and other artefacts which is the reason why most of the other algorithms did not performed very well.

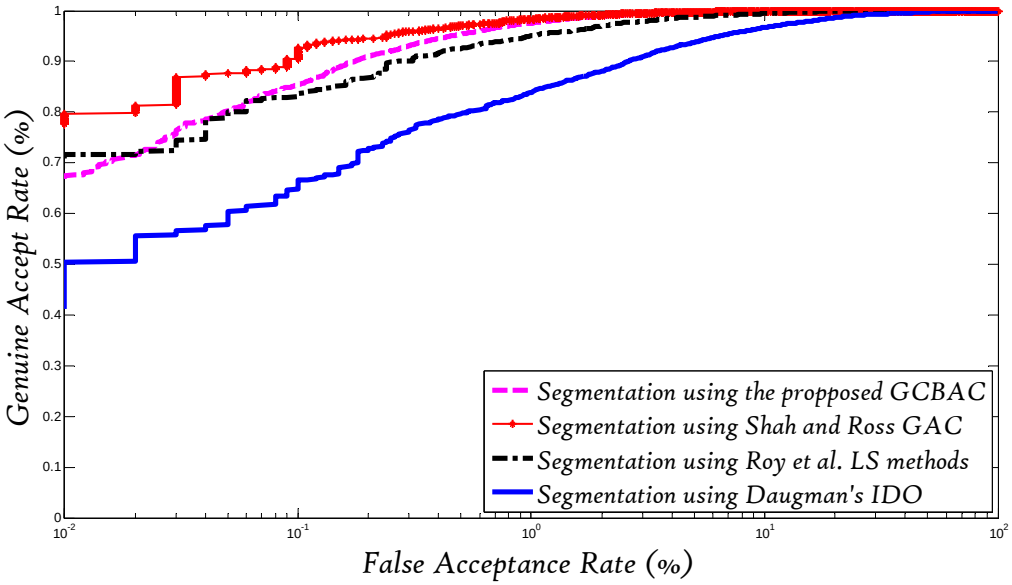

Figure 5.8: ROC curves showing the performance of the proposed GCBAC segmentation technique compared with other state-of-the-art iris segmentation algorithms [51-53], on CASIA Iris V4-Lamp subset.

The performance of the proposed GCBAC algorithm on the CASIA Iris V4-Lamp is as shown in Figure 5.8. The ROC curves shows that the proposed GCBAC again outperformed other current state-of-the-art segmentation algorithms on this data subset. As can be seen also, the integro-differential method performed better on this data subset compared to its performance CASIA Iris V4-Interval.

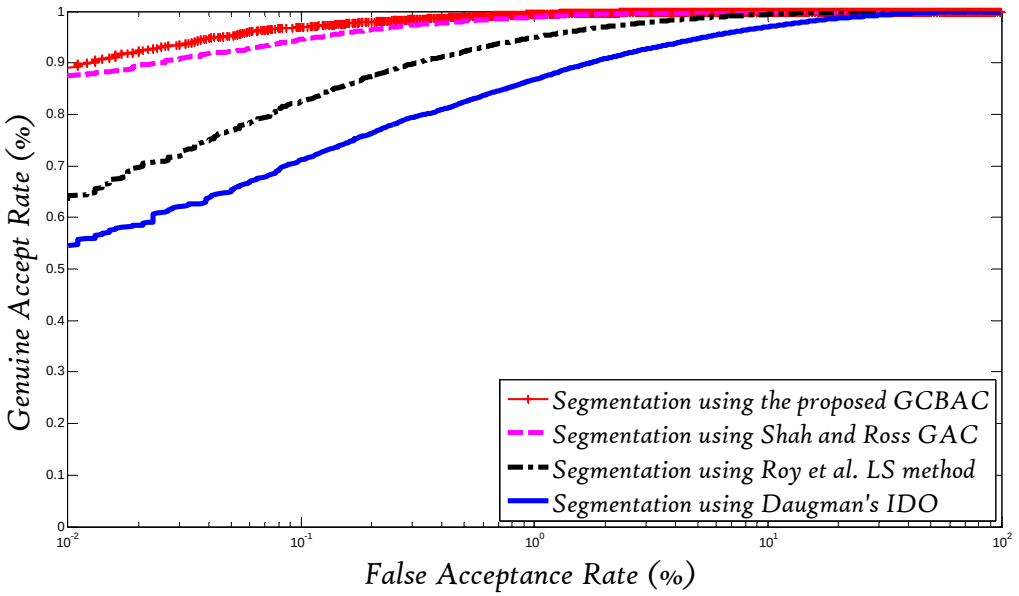

Figure 5.9: ROC curves showing the performance of the proposed GCBAC segmentation technique compared with other state-of-the-art segmentation algorithms [51-53], on CASIA Iris V4-Distance subset.

Also, the performance of the proposed GCBAC algorithm on the CASIA Iris V4-Distance is as shown in Figure 5.9. The ROC curves shows that the proposed GCBAC again outperformed other current state-of-the-art segmentation algorithms as usual on this data subset. This iris image data subset is very challenging but that notwithstanding, our proposed algorithm achieved an impressive performance of 99.97%.

Likewise, Figures 5.10 and 5.11 displays the ROC curves on UBIRIS V2.0 and the combined dataset from all the other iris image datasets. The experiments on these dataset are designed to ascertain the robustness of the proposed iris segmentation algorithm. The figures show robustness of the algorithm to handle the diverse challenges of different kinds of these iris image subsets. Also, the UBIRIS dataset is highly challenging as it contains iris images obtained from near real life condition under varying lightning illuminations.

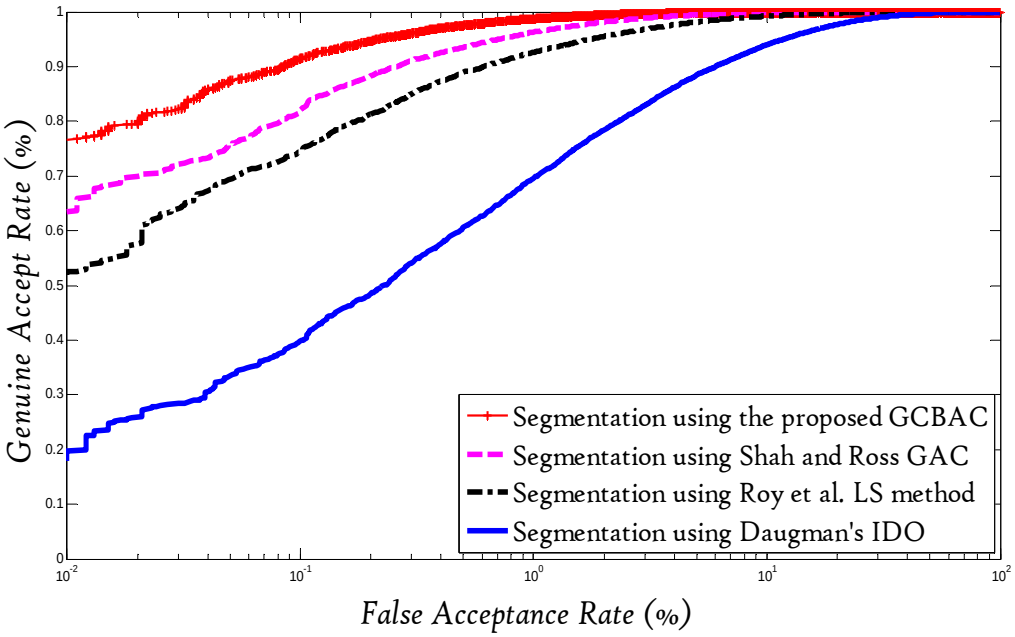

Figure 5.10: ROC curves showing the performance of the proposed GCBAC segmentation technique compared with other state-of-the-art segmentation algorithms [51-53], on UBIRIS V2.0 iris image dataset.

From Figure 5.10, it can be seen that the proposed GCBAC algorithm outperformed other state-of-the-art iris segmentation algorithms. However, the performance of the algorithm on this dataset is lower compared to the pervious datasets tested.

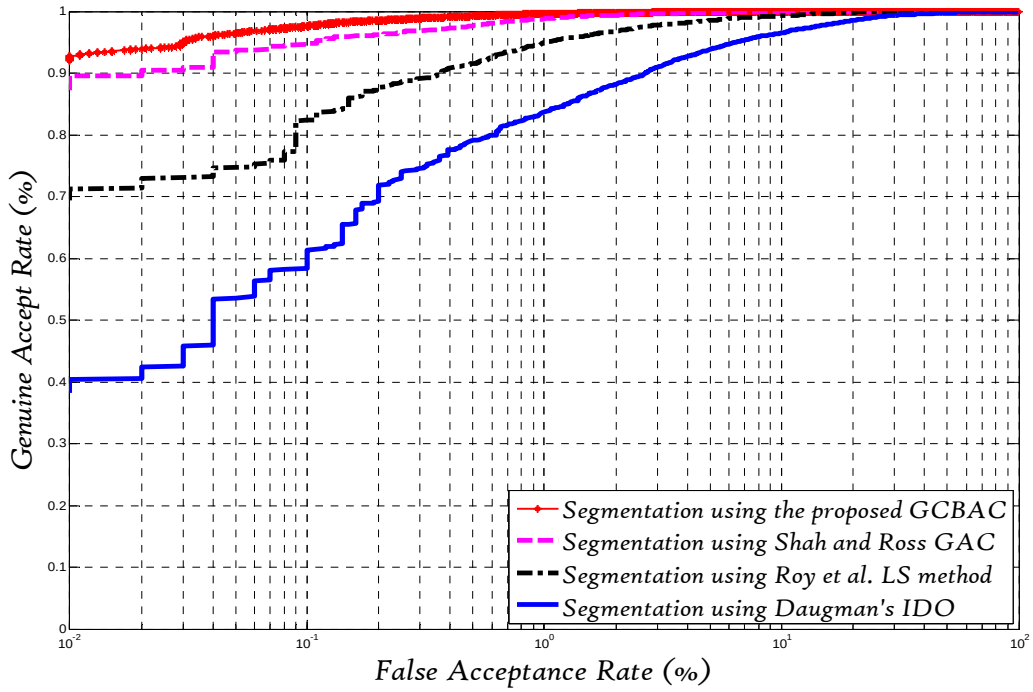

Figure 5.11: ROC curves showing the comparison of the proposed GCBAC segmentation technique with other state-of-the-art existing segmentation techniques [51-53], on the combined subset.

The proposed GCBAC algorithm showed impressive performance on the combined iris image dataset as can be seen from Figure 5.11. However, most other current state-of-the-art iris segmentation algorithms experience a decline in performance on this image subset due to the heterogeneous nature of the images in this subset. This illustrates the ability of our algorithm to deal with variety of images.

Figure 5.12: Samples of iris images from UBIRIS and CASIA datasets where the proposed segmentation schemes failed to detected the iris and pupil boundaries

Notwithstanding the impressive performance of the proposed iris segmentation algorithm based on GCBAC, there are still some images that remains challenging to the algorithm. Figure 5.8, depicts samples of highly occluded iris images where our segmentation algorithm failed to segment the iris boundaries. It can be seen that these iris images are heavily occluded and mostly impossible to segment.

To further demonstrate the time efficiency and accuracy of the segmentation algorithm, the proposed algorithm is compared with other active contour based methods on the combined dataset and their classification accuracy and speed are as shown in Table 5.1. The experiment was carried out by implementation of the proposed GCBAC method and other current methods based on geodesic active contour GAC [53], as well as the level set LS based active contour method [52], on a standard Pentium IV 3.40GHZ computer with 16.0GB memory running Windows 7 Enterprise operating system. The implementation was carried out by segmenting the iris images using the different methods while the proposed feature extraction and classification methods was used for all of the different approaches. The result of the experiment is as shown in Table 5.1 and as can be deduced from the table, our algorithm outperformed the other methods.

Algorithm	Classification accuracy (%)	Time (ms)
Shah&Ross [52]	98.12	13335.2
Roy et al. [53]	98.08	11467.5
Proposed GCBAC	99.58	7482.20

Table 5.1: Comparison of accuracy and speed of the proposed method and other active contour based methods on the combined dataset.

Algorithm	Equal Error Rate (EER) (%)				
	CASIA-V4 Interval	CASIA-V4 Twin	CASIA-V4 Lamp	CASIA-V4 Distance	UBIRIS V2.0
Daugman [17]	0.49	1.80	0.96	8.45	6.38
Shah&Ross [52]	0.44	1.28	0.77	1.91	1.20
Roy et al. [53]	0.40	0.93	0.70	1.80	1.14
Proposed GCBAC	**0.38**	**0.90**	**0.60**	**1.02**	**0.93**

Table 5.2: Comparison of the EER of the proposed method with other active contour based methods on the combined dataset.

Algorithm	Correct Recognition Rate (CRR) (%)				
	CASIA-V4 Interval	CASIA-V4 Twin	CASIA-V4 Lamp	CASIA-V4 Distance	UBIRIS V2.0
Daugman [17]	98.13	95.70	97.28	83.14	93.43
Shah and Ross [52]	95.79	95.54	95.45	78.33	92.56
Roy et. al. [53]	95.64	94.90	95.78	77.24	91.30
Proposed GCBAC scheme	**98.99**	**97.55**	**98.97**	**99.50**	**97.30**

Table 5.3: Comparison of the CRR of the proposed method with other active contour methods on the combined dataset.

5.5 Evaluation of the Feature Extraction and Selection Scheme

To validate the feature extraction method, the iris images in the combined dataset are first segmented using the proposed iris segmentation algorithm. The proposed feature extraction method based on principally rotated complex wavelet filters (PR-CWF) and the feature extraction method in [82] which is based on dual tree complex wavelet transform 2D DT-CWT was employed to extract the important iris information. While, the modified adaptive SVM classification was used for the classification of the iris samples. Performance evaluations of the two methods was achieved using the methods discussed in Sections 5.22 and 5.2.3. Figure 5.13, shows the comparison of the proposed feature extraction method using PR-CWF and the feature extraction using DT-CWT.

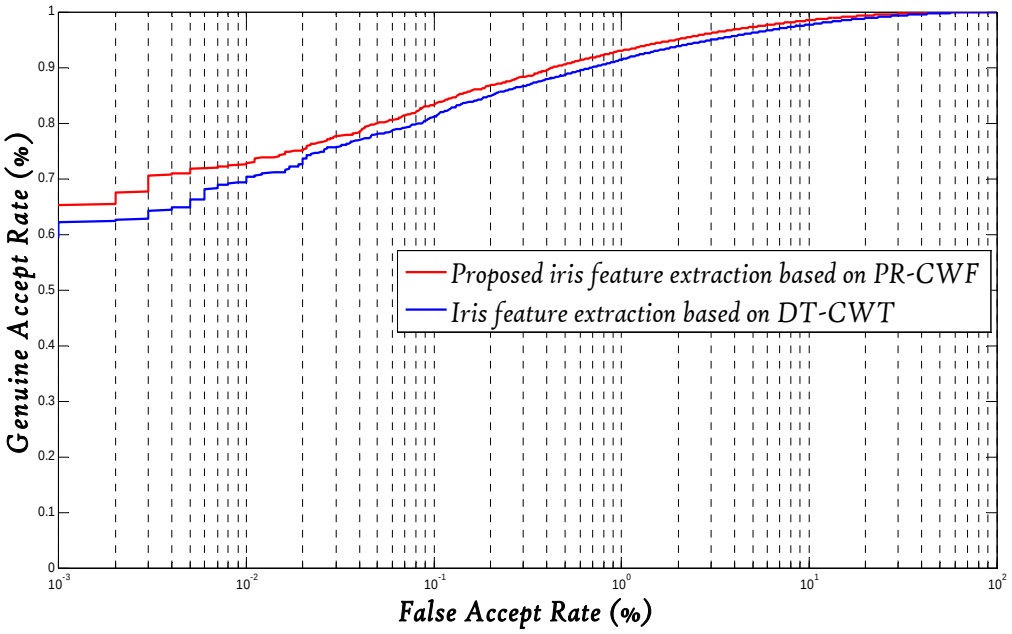

Figure 5.13: ROC curves showing the comparison of the proposed feature extraction based on PR-CWF and DT-CWT

Also, Table 5.4, shows the comparison of the proposed feature extraction algorithm with other popular feature extraction algorithms in [44-43]. The table compares the length of the feature vector, the accuracy and time efficiency of the algorithms. It is evident from the table that our algorithm yields a better accuracy and time efficiency than other methods.

Algorithm	Length of feature vector	Accuracy (%)	Time (ms)
Daugman [17]	2048 bits	84.12	246
Ma et al. [31]	384 elements	88.70	186
Narote et al. [77]	1088 elements	90.88	87.1
Bodade [78]	72 elements	92.87	90.3
PR-CWF	**110 elements**	**98.57**	**46**

Table 5.4: Comparison of the feature vector lengths, accuracies and speed of the proposed PR-CWF scheme with other feature extraction techniques.

Algorithm	**Time (ms)**
Iris Segmentation	7250
Unwrapping	95
Feature Extraction	46
Matching	91.20
Average Execution Time	**7482.20**

Table 5.5: Average time consumption of the different parts of the proposed iris recognition algorithm.

5.6 Evaluation of the Computation Complexity of the Algorithms

In this section we introduce a complexity analysis to determine the amount of resources (such as time or storage) necessary to execute the algorithm. Most algorithms are designed to accept inputs of arbitrary size. Therefore, the efficiency or running time of the algorithm will be stated as a function relating the input size to the number of steps (time complexity) or storage (space complexity). The analysis of algorithm is a very important part of the computation complexity theory, which provides theoretical estimates for the resources needed by any algorithm, as a complexity function for any arbitrary large input.

The Big*O* notation have been employed in this work to this end. Time complexity of the algorithm is of crucial importance if the algorithm is designed to run in

environments where tasks are given a small amount of time to perform tasks. To determine the computation complexity of the proposed GCBAC segmentation algorithm, we need to examine the computation complexity of each step in the algorithm. The function *RefRemove* needs time $O(MN)$, since there are $\frac{MN}{L^2}$ holes in the image. The segmentation of the inner and outer boundaries of each iris requires $O(K^2)$ time while the time for feature calculation is given as $O(1)$. The functions *InitGraph* and *InitSeed* need $O\left(\frac{MN}{L^2}\right)$ time, because there are $\frac{MN}{L^2}$ vertices and $\frac{2(M-1)(N-1)}{L^2}$ edges in graph G_0 and $\frac{MN}{L^2}$ sets in label l_0 initially. After the first iteration, the number of nodes in level i is at most, half of the nodes in level $l-1$. Therefore, there are at most $(log\frac{MN}{L^2})$ iterations. So, the total time needed in one iteration is $O(\frac{MN}{L^2})$, except for the subroutines *CreateGraph*. The subroutine *CreateGraph* needs $O(|V_{level-1}| + |E_{level-1}|)$ time. Therefore, the total time needed for a single iteration is $O(\frac{MN}{K^2})$ and the computation complexity of the whole algorithm can be is given as:

$$O\left(MN + \frac{MN}{L^2}\log\left(\frac{MN}{L^2}\right)\right), \quad (5.4)$$

Therefore, considering the model's time complexity in Equation (5.4), we can conclude that the model is highly efficient in finding the optimal boundaries of the iris.

5.6 Summary

In this chapter, we tested our proposed approaches with different heterogeneous iris image datasets. Our proposed approaches have also been compared with other existing state-of-the-art iris recognition algorithms. As evident from Table 5.5, our approach with 98.57% accuracy value outperforms existing state-of-the-art approaches for extracting the most significant iris features in non-ideal iris images. Also, our segmentation approach with accuracy values of 98.99%, 97.55%, 98.97%, 99.50% and 97.30 on CASIA-V4-Interval, CASIA-V4-Twin, CASIA-V4-Lamp, CASIA-V4-Distance and UBIRIS V2.0, respectively, outperformed other state-of-the-art segmentation algorithms [51-53]. For the best active contour based approach [52] compared with our proposed approach the improvement is 1.46% on the combined dataset. Similarly, for the best traditional and

most popular iris segmentation algorithms [17], the improvement is an average of 5.19% on the four CASIA V4 (Interval, Twins, Lamp and Distance) iris datasets. In addition, the extraction of iris features is of great importance at the classification level. As illustrated in Table 5.1, there is approximately twice a reduction in the average computational time by using the proposed segmentation algorithm compared to other state-of-the-art segmentation algorithms. This reduction in computational time is caused by two main reasons: 1) the initialization of the active contour close to the boundaries of the iris, 2) the hybrid method of graph cut energy and active contour which eliminates the complexity of the LS function. This demonstrates that our approach while running on a slower platform is computationally more efficient than other approaches while still maintaining higher accuracy than the other approaches. This major advantage would be applicable to a number of iris based recognition systems that require real time identification of individual identity such as online transactions and embedded systems.

Chapter 6

6. CONCLUSION AND FUTURE WORK

This chapter discusses the key contributions of our research work in Section 6.1, and suggests the ways of conducting future research in section 6.2.

6.1 Conclusion

Iris recognition has been a highly interesting research topic over the last decade due to the increased security requirements for the sophisticated personal identification systems based on biometrics. The rich unique and stable textural details of the iris patterns makes iris a biometric modality for identifying an individual accurately and reliably. Most current iris recognition algorithms exhibits high recognition accuracies in relatively cooperative environments. However, the processing and recognition of degraded iris image still remains a challenging issue. In this thesis, we have focused on the processing of non-ideal iris images using GCBAC, PR-CWF, PSO, and ASVMs. In order to verify the claimed performances, the proposed methods were evaluated on several challenging iris datasets, namely: CASIA Version 4 Interval, CASIA Version 4 Twins, CASIA Version 4 Distance, UBIRIS Version 2.0 and a heterogeneous combined dataset. Furthermore, to show the effectiveness of the proposed algorithms, comparisons are made with several state-of-the-art iris recognition methods.

The accurate segmentation of the iris plays an important role in iris recognition because the accuracy of the subsequent phases depends on the correct segmentation of the iris region. While most of the current iris recognition schemes based on active contour are based on the evolution of a curve from the boundary of the pupil to the boundary of the iris. This proposed scheme adopted an efficient 2-level hierarchical approach which first roughly approximates the boundaries of the iris and then refines the approximated boundary using the proposed GCBAC. This approach eliminates errors from one level from getting into the subsequent levels and the repetition of the process makes the process complimentary. Also, while current methods are based on the LS algorithm or regional

energy, which is slow to convergence and is attracted to local minima like the reflection boundaries, the pupillary boundaries and other outlayers in the image caused by noise, The proposed iris segmentation algorithm is based on GCBAC algorithm which brings together region-based and boundary-based methods and appropriates different probability spaces into a common information-sharing framework and accurately overcome outlayers and detect the accurate boundary at efficient time. The accurate localization of the iris regions from the degraded eye images has been achieved at almost half the speed of most current iris segmentation algorithms. The proposed localization scheme based on GCBAC avoids over-segmentation and performs well in blurred images of the iris/sclera boundary. The image enhancement algorithm is able to increase the quality of the iris image and reduce the effects of noise while leaving the original image's structure largely unaltered. This keeps the image in good form for further processing. Finally, the proposed algorithm localizes the iris regions accurately from degraded iris images that have been affected by different nonideal factors.

Also, the importance of extracting important iris features from the segmented iris sample cannot be overemphasised. Extracting redundant iris features impacts greatly on the classification accuracy and speed. The proposed principally rotated complex wavelet features (PR-CWF) and particle swam optimization (PSO), is able to extract the most important iris features and selected the most prominent features from the feature vector for the representation of the iris. While most of the current iris recognition algorithms utilize the complete iris information for iris recognition, we have chosen to use the right and left sectors of the iris image which is less susceptible to occlusions from the eyelids and eyelashes for iris recognition and this leads to higher recognition accuracy and reduced false rejection. The combined PR-CWF and PSO based feature selection method reduces the dimensionality of the extracted iris feature sequence without losing the matching accuracy. The employed ASVM performs well even in poorly balanced sample space and control different classification errors. We also provide experimental validations which exhibits an encouraging performance with respect to the accuracy of other relative non-ideal iris recognition algorithms.

6.2 Future Research

In this thesis, the proposed iris recognition approaches performs reasonably well in degraded iris images. However, there are numerous issues that should be addressed and resolved in order to improve the performance even the more. Future research could be conducted along the following directions to build a robust iris (biometrics) recognition system.

1. In this thesis, the GCBAC model uses the combination of the strengths of the gradient local and region-based methods for finding the iris boundaries. However, a simple region based method can still be used by fussing multiple regions in order to determine the optimum boundaries of the iris. An improved iris segmentation scheme can possibly be developed by integrating the RAC model with the VLS based boundary finding method while using game theory as a fusion scheme. Also, shape prior along with the region and boundary data can be applied to attempt to further improve the segmentation performance. Moreover, reversing the order of the segmentation process can significantly improve the algorithm. Processing the eyelashes first and eliminating the eyelid/eyelash before applying the segmentation algorithm can greatly enhance the segmentation accuracy and act as a way of accessing the quality of the original iris image before initializing the processing of the image.
2. Since the quality of the images affect the overall matching accuracy and In order to eliminate time wasted in highly degraded iris images, an iris image quality assessment scheme needs to be employed to eliminate closed eyes and other iris image that cannot pass for recognition. Most current iris image quality assessment methods deal exclusively with the iris images captured in a Near Infra-Red (NIR) setup, an enhanced method can be deployed to assess the quality of iris images captured by using the Visible Wavelength (VW) light imagery. In general, the VW imaging setup is able to acquire iris data at significantly larger distances and on moving subjects.
3. In this thesis, we only used the global or local features for iris recognition. However, the recognition performance can possibly be improved by fussing both the local and global features while using PSO and SVMs as fusion strategies.
4. In this thesis, we have dealt with iris images that have been captured in both NIR and VW imagery setup. However, a more sophisticated iris segmentation scheme

can be develop for the VW iris images only. In this way, the whitish sclera can be utilized for segmentation instead of the iris information.

5. In real-world application, the unimodal biometric system like the iris recognition system is often faced with significant limitations due to noisy sensor data, restricted degree of freedom, intra-class variability, unacceptable error rates, and a lot of other factors. Multimodal biometric systems seeks to alleviate some of these problems by providing multiple pieces of evidence for the same identity. Multimodal biometric systems can significantly improve the recognition performance in addition to improving greater population coverage, better anti-spoofing measures, increasing the degree of freedom, and reduces the failure to enrol rate. An effective fusion scheme that can combine information presented by the multiple domain experts, based on score level fusion method can be able to address some of the limitations of the existing unimodal authentication systems. In more specific terms, the combination of the iris and the keystroke dynamics representing physical and behavioural biometrics of an individual can be utilized for accurate and reliable identification purpose especially for monitoring and surveillance purposes.
6. As can be seen, the most computation intensive part of the algorithm involves the segmentation of the iris. Since we have implemented the system in Matlab, which is an interpreted language, an improvement in speed can be achieved if the most time consuming part of the system is implemented in C++ programming language environment.
7. The iris liveness detection is a major issue in the area of iris recognition otherwise, a high resolution photograph can be presented to an iris recognition system which might result to a false match. Fake iris detection is another important factor which should be given careful attention. The contact lenses vastly used nowadays is capable of changing the colour of an individual’s iris. This may lead to problems with the iris recognition system since a fake iris pattern is printed on the surface of the lens. The system may lead to false rejection of an enrolled user. Contrary, the system may falsely accept a subject, if the iris patterns of that subject has been enrolled in the database. Therefore, further research is required to overcome these challenges.

Chapter 7

7. REFERENCES

[1] A. Bertillon, “La Couleur de l’iris,” Revue Scientifique, vol. 36, no. 3, pp. 65–73, 1885.

[2] J.H. Doggart, “*Ocular signs in slit-lamp microscopy*,” Kimpton (1949), page 27

[3] F. Adler, “Physiology of the eye: clinical application,” The C.V. Mosby Company, 4th edition, 1965.

[4] L. Flom and A. Safir, “Iris recognition system,” U.S. Patent 4,641,349, 1987.

[5] R. Johnston, “Can iris patterns be used to identify people?,” *Los Alamos National Laboratory, Chemical and Laser Sciences Division Annual Report LA-12331-PR*, pp. 81-86, 1992.

[6] R. Bracewell, “Two-dimensional imaging,” Prentice-Hall, 1995.

[7] A. K. Jain, A. Ross, and S. Prabhakar, “An introduction to biometric recognition,” *IEEE Trans. Circuits and Systems for Video Technology*, vol. 14, no. 1, pp. 4 – 20, 2004.

[8] J. Daugman, “High confidence visual recognition of persons by a test of statistical independence,” *IEEE Transactions on Pattern Analysis and Machine Intelligence*, vol. 15, no. 11, pp. 1148–1161, November 1993.

[9] J. Daugman, “Biometric personal identification system based on iris analysis,” U.S. Patent No. 5,291,560, 1994.

[10] J. Daugman, “The importance of being random: Statistical principles of iris recognition,” *Pattern Recognition*, vol. 36, no. 2, pp. 279–291, 2003.

[11] John Daugman, “How iris recognition works,” *IEEE Transactions on Circuits and Systems for Video Technology*, vol. 14, no. 1, pp. 21–30, 2004.

[12] R. P. Wildes, J. C. Asmuth, S. C. Hsu, R. J. Kolczynski, J. R. Matey and S. E. McBride, “Automated, noninvasive iris recognition system and method,” U.S. Patent No. 5,572,596, 1996.

[13] W. Boles and B. Boashash, “A human identification technique using images of the iris and wavelet transform,” *IEEE Transactions on Signal Processing*, vol. 46, no. 4, pp. 1185–1188, 1998.

[14] J. Daugman, “Iris Recognition: The coloured part of the eye contains delicate patterns that vary randomly from person to person, offering a powerful means of identification,” *American Scientist*, vol. 89, no. 4, pp. 326-333, 2001.

[15] J. Daugman, “Statistical richness of visual phase information: update on recognizing persons by iris patterns,” *International Journal of Computer Vision*, vol. 45, no. 1, pp. 25–38, 2001.

[16] K.W. Bowyer, K. P. Hollingsworth, and P. J. Flynn, “A survey of iris biometrics research 2008–2010,” *In The Proceedings of Workshop on Multimodal User Authentication*, pp. 48–55, Dec 2003.

[17] K.W. Bowyer, K. P. Hollingsworth and P. J. Flynn, “Image understanding for iris biometrics: a survey,” *Computer Vision and Image Understanding*, vol. 110, pp 281–307, Oct. 2008.

[18] K.W. Bowyer, K. P. Hollingsworth and P. J. Flynn, “A survey of iris biometric research 2008-2010,” *Handbook on Iris Recognition Advances in Computer Vision and Pattern Recognition*, Chapter 2, Springer-Verlag, London, 2013.

[19] L. Masek, “Recognition of human iris patterns for biometric identification,” *B.S. Dissertation , The School of Computer Science and Software Engineering*, The University of Western Australia, Crawley WA, Perth, Australia, 2003.

[20] C. Tisse L. Martin L. Torres and M. Robert, “Person identification technique using human iris recognition*” Proc. Vision Interface*, pp. 294-299, 2002.

[21] L.W. Liam, A. Chekima, L.C. Fan, and J.A. Dargham, “Iris recognition using self-organizing neural network”, *Student Conference on Research and Development Proceedings*, pp. 169- 172, 2002.

[22] X. Liu, K. W. Bowyer and P. J. Flynn, “Experimental evaluation of iris recognition,” *In The Proceedings of Face Recognition Grand Challenge Workshop*, 2005.

[23] X.M. Liu, K.W. Bowyer, and P.J. Flynn, “Experiments with an improved iris segmentation algorithm,” *Proc. Fourth IEEE Workshop Automatic Identification Advanced Technologies*, 2005.

[24] E. Trucco and M. Razeto, “Robust iris location in close-up images of the eye,” *Pattern Analysis & Applications*, vol. 8, no. 3, pp. 247-255, 2005.

[25] P. Huang, C. Chiang and J. Liang, “Iris recognition using fourier-wavelet features,” *In The Proceedings of International Conference on Audio-and-Video-Based Biometric Person Authentication*, pp. 14–22, 2005.

[26] L .Ma, T. Tan, Y. Wang and D. Zhang, “Efficient iris recognition by characterizing key local variations,” *IEEE Trans. Image Processing*, vol. 13, pp. 739 – 750, 2004.

[27] X. Feng, C. Fang, X. Ding and Y. Wu, “Iris localisation with dual coarse-to-fine strategy,” *18th International Conference on Pattern Recognition*, pp. 553-556, 2006.

[28] W. Zhang, B. Li, X. Ye, and Z. Zhuang, “A robust algorithm for iris localisation based on radial symmetry,” *Conference on Computational Intelligence and Security Workshops*, pp. 324-327, 2007.

[29] M. A. Luengo-Oroz, E. Faure, and J. Angulo, “Robust iris segmentation on uncalibrated noisy images using mathematical morphology,” *Image and Vis. Comput.*, vol. 28, no. 2, pp. 278-284, Feb. 2010.

[30] D. S. Jeong, J. W. Hwang, B. J. Kang, K. R. Park, C. S. Won, D. K. Park, and J. Kim, “A new iris segmentation method for non-ideal iris images,” *Image and Vis. Comput.*, vol. 28, no. 2, pp. 254-260, Feb. 2010.

[31] Y. Zhou and A. Kumar, “Personal identification from iris images using localized radon transform,” *Proc. in IEEE Int. Conf. on Pattern Recog.*, pp. 2840-2843, Istanbul, Turkey, Aug. 2010.

[32] T. Camus and R. Wildes, “Reliable and fast eye finding in close-up images,” *In The Proceedings of International Conference on Pattern Recognition*, pp. 389–394, 2002.

[33] W.K. Kong and D. Zhang, “Accurate iris segmentation based on novel reflection and eyelash detection model,” Proc. *Int’l Symp. Intelligent Multimedia, Video and Speech Processing*, pp. 263-266, 2001.

[34] W. Kong and D. Zhang, “Detecting eyelash and reflection for accurate iris segmentation,” *International Journal of Pattern Recognition and Artificial Intelligence*, vol. 17, no. 6, pp. 1025–1034, 2003.

[35] A. Radman, K. Jumari, and N. Zainal, “Fast and reliable iris segmentation algorithm,” *IET Image Processing*, vol. 7, iss. 1, pp. 42 – 49, 2013.

[36] J. Huang, Y. Wang, T. Tan and J Cui, “A new iris segmentation method for recognition,” *In proc. 17th Int. Conf. Pattern Recognition (ICPR), Cambridge, U.K.*, vol. 3, pp. 23 – 26, Aug. 2004.

[37] Z. Zhou, Y. Du, and C. Belcher, “Transforming traditional iris recognition systems to work on non-ideal situations,” *IEEE Trans. Industrial Electronics*, vol. 56, no. 8, pp. 3203-3213, Aug. 2009.

[38] Z. Sun, Y Wang, T. Tan and J. Cui, “Improving iris recognition accuracy via cascaded classifiers,” *IEEE Trans. On Systems, Man, and Cybernetics part C, Application and Reviews*, vol. 35, no. 3, pp. 435 – 441, 2005.

[39] S. A. C. Schuckers, N. A. Schmid, A. Abhyankar, V. Dorairaj, C. K. Boyce, and L. A. Hornak, “On techniques for angle compensation in non-ideal iris recognition,” *IEEE Transactions on Systems, Man, and Cybernetics - Part B*, vol. 37, no. 5 pp. 1176–1190, Oct 2007.

[40] C. Chou, S. Shin, W. Chen, V. W. Cheng and D. Chen, “Non-orthogonal view iris recognition system,” *IEEE Trans. on Circuits and Sys. For Video Tech*., vol. 20, no. 3, March 2010.

[41] J. Zuo, and N. A. Schmid, “On the methodology for robust segmentation of non-ideal iris images,” *IEEE Trans. on Systems, Man, and Cybernetics-Part B*, vol. 40, no. 3, June 2010.

[42] C. Tan, and A. Kumar, “A unified framework for automated iris segmentation using distantly acquired face images,” *IEEE Trans. Image Processing*, 2012.

[43] Z. He, T. Tan, Z. Sun, and X. Qiu, “Robust eyelid, eyelash and shadow localization for iris recognition,” *Proc. Int’l Conf. Image Processing*, 2008.

[44] Z. He, T. Tan, Z. Sun and X. Qui, “Towards accurate and fast iris segmentation for iris biometrics,” *IEEE Trans. On Pattern Analysis and Machine Intelligence (PAMI)*, vol. 31, no. 9, pp. 1617-1632, 2009.

[45] Z. He, T. Tan and Z. Sun, “Iris localization via pulling and pushing,” *International Conference on Pattern Recognition*, pp. 366 - 369, 2006.

[46] H. Proenca and L.A. Alexandre, “Iris segmentation methodology for non-cooperative recognition,” *IEEE Proc. Vision, Image and Signal Processing*, vol. 153, pp. 199-205, 2006.

[47] H. Proenca and L. A. Alexandre, “Toward noncooperative iris recognition: a classification approach using multiple signatures,” *IEEE Trans. Pattern Anal. Machine Intell.*, vol. 29, no. 4, pp. 607–612, Apr. 2007.

[48] H. Proença, “Iris recognition: on the segmentation of degraded images acquired in the visible wavelength,” *IEEE Trans. on Pattern Anal. Machine Intell.*, vol. 32, no. 8, pp. 1502-1516, Aug. 2010.

[49] W. J. Ryan, D. L. Woodard, A. T. Duchowski, and S. T. Birchfield, “Adaptive starburst for elliptic iris segmentation,” *IEEE Second Int. Conf. on Biometric: Theory, Applications and Systems*, 2008.

[50] S. J. Pundlik, D. L. Woodard, and S. T. Birchfield, “Non-ideal iris segmentation using graph cuts,” *Computer Vision and Pattern Recognition Workshops, IEEE Computer Society Conference on (CVPR2008)*, pp. 1–6, June 2008.

[51] J. Daugman, “New methods in iris recognition,” *IEEE Transactions on Systems, Man and Cybernetics - B*, vol. 37, no. 5, pp. 1167–1175, Oct 2007.

[52] S. Shah and A. Ross, “Iris Segmentation using geodesic active contours,” *IEEE Transaction on Information Forensics and Security*, vol. 4, iss. 4, pp. 824-836, Dec. 2009.

[53] K. Roy and P. Bhattacharya, “Nonideal iris recognition using level set approach and coalitional game theory,” *Proc. in Int. Conf. on Comp. Vis. Syst., Springer Lecture Notes in Computer Science*, vol. 5815, pp. 394-402, Oct. 2009.

[54] M. Vatsa, R. Singh, and A. Noor, “Improving iris recognition performance using segmentation quality enhancement match score fusion, and indexing,” *IEEE Transactions on Systems, Man, and Cybernetics, Part B: Cybernetics*, vol. 38, iss. 4, pp. 1021-1035, Aug 2005.

[55] K. Roy, P. Bhattacharya, and C. Y. Suen, "Unideal iris segmentation using region-based active contour model," *Proc. in Int. Conf. on Image Anal. And Recog., Springer Lecture Notes in Computer Science*, vol. 6112, pp. 256-265, Jun. 2010.

[56] K. Roy, P. Bhattacharya, and C. Y. Suen, “Towards nonideal iris recognition based on level set method, genetic algorithms and adaptive asymmetrical SVMs,” *Eng. Appl. Artif. Intelligence*, vol. 24, no. 3, pp. 458 – 475, April 2011.

[57] S. Rakshit and D. M. Monro, “Pupil shape description using fourier series,” *Proc. IEEE Workshop Signal Processing Applications for Public Security and Forensics*, pp. 1 – 4, 2007.

[58] C.-C. Tsai, H.-Y, Lin, J. Taur, and C.-W. Tao, “Iris recognition using probabilistic fuzzy matching on local features,” *IEEE Trans., Syst., Man, Cybernetics B, Cybernetics*, vol. 42, no. 1, pp. 150 – 162, Feb. 2012.

[59] J. Daugman, “Demodulation by complex-valued wavelets for stochastic pattern recognition,” *International Journal of Wavelets, Multiresolution and Information Processing*, vol. 1, no. 1, pp. 1–17, 2003.

[60] L. Ma, T. Tan, Y. W, and D. Zhang, “Personal identification based on iris texture analysis,” *IEEE Transactions on Pattern Analysis and Machine Intelligence*, vol. 25, no. 12, pp. 1519–1533, 2003.

[61] L. Ma, Y. Wang, and T. Tan, “Iris recognition based on multichannel Gabor filtering,” *Asian Conf. on Computer Vision*, pp. 1-5, 2002.

[62] L. Ma, Y. Wang, and T. Tan, “Iris recognition based on circular symmetric filters,” *Int. Conf. on Pattern Recognition*, vol. 2, pp. 414-417, 2002.

[63] G. Feng, and Y. Wu, “An iris recognition algorithm based on DCT and GLCM,” *Proc. of Optical and Digital Image Processing*, vol. 7000, 2008.

[64] P. E. Merloti and R. Swiniarski, “Experiments on human iris recognition using error backpropagation artificial neural network,” http://www.merlotti.com/EngHome/Computing/iris rec nn.pdf, San Diego State University, 2004.

[65] E. Rydgren, T. Ea, F. Amiel, F. Rossant, and A. Amara, “Iris features extraction using wavelet packets,” *In The Proceedings of The International Conference on Image Processing*, vol. 2, pp. 861–864, 2004.

[66] V. Dorairaj, N. Schmid, and G. Fahmy, “Performance evaluation of non-ideal iris based recognition system implementing global ICA encoding,” *In The Proceedings of IEEE International Conference on Image Processing*, vol. 3, pp. 285–288, 2005.

[67] D. Cai, Q. Tan, Y. Yan, G. Jin, and Q. He, “Using optical wavelet packet transform to improve the performance of an optoelectronic iris recognition system,” SPIE Proc. on Information, Optics and Photonics Technology, vol. 5642, pp. 497-501, 2005.

[68] C. Fancourt, L. Bogoni, K. Hanna, Y. Guo, R. Wildes, N. Takahashi, and U. Jain, “Iris recognition at a distance,” *In The Proceedings of International Conference on Audio- and Video-Based Biometric Person Authentication*, pp. 1–13, 2005.

[69] E. Krichen, L. Allano, S. Garcia-Salicetti and B. Dorizzi, “Specific texture analysis for iris recognition,” *In The Proceedings of International Conference on Audio- and Video-Based Biometric Person Authentication*, pp. 23–30, 2005.

[70] C. Sanchez-Avila and R. Sanchez-Reillo, “Two different approaches for iris recognition using gabor filters and multiscale zero-crossing representation,” *Pattern Recognition*, vol. 38, no. 2, pp. 231–240, 2005.

[71] Craig Belcher and Yingzi Du, “Region-based sift approach to iris recognition,” *Optics and Lasers in Engineering*, vol. 47, pp.139–147, 2009.

[72] B. J. Kang and K. R. Park, "A study on iris image restoration," *In The Proceedings of International Conference on Audio-and-Video-Based Biometric Person Authentication*, pp. 31–40, 2005.

[73] N. Schmid, M. Ketkar, H. Singh, and B. Cukic, "Performance analysis of iris-based identification system at the matching score level," *IEEE Transactions on Information Forensics and Security*, vol. 1, no. 2, pp. 154–168, 2006.

[74] Z. Sun, T. Tan, and Y. Wang, "Robust encoding of local ordinal measures: A general framework of iris recognition," *In Proceedings of BioAW Workshop*, pp. 270–282 2004.

[75] M. Vatsa, R. Singh and A. Noore, "Reducing the false rejection rate of iris recognition using textural and topological features," *International Journal of Signal processing*, vol. 2, no. 2, pp. 66 – 72, 2005.

[76] C.M. Patil and S. Patilkulkarani, "A comparative study of feature extraction approaches for an efficient iris recognition system," *In: Information Processing and Management*, pp. 411–416 2010.

[77] H. B. kekre, S. D. Thepade, and J. J. N. Agrawal, "Iris recognition using textural features extracted from Haarlet pyramid," *International Journal of Computer Application*, vol. 11, no. 12, pp. 1 – 5, 2010.

[78] P. Zhang, D. Li, and Q. Wang, "A novel iris recognition method based on feature fusion," *In Proceedings of International Conference on Machine Learning and Cybernetics*, pp. 3661 – 3665, 2004.

[79] V. N. Boddeti and B. V. K. V. Kumar, "Extended-depth-of-field iris recognition using unrestored wavefront-coded imagery," *IEEE Trans. Syst. Man and Cyber. A*, vol. 40, no. 3, pp. 495-508, May 2010.

[80] E. Krichen, S. Garcia-Salicetti, and B. Dorizzi, "A new phase-correlation-based iris matching for degraded images," *IEEE Trans. Syst. Man and Cyber. B,* vol. 39, no. 4, pp. 924-934, Aug. 2009.

[81] R. M Bodade and S. N. Talbar, "Shift invariant iris feature extraction using rotated complex wavelet and complex wavelet for iris recognition system," *Int. Conf. on Advances in Pattern Recognition*, pp. 449-452, 2009.

[82] A. S. Narote, S. P. Narote, L. M. Waghmare, and M. B. Kokare, “Robust iris feature extraction using dual tree complex wavelet transform,” *IEEE Int. Conf. on Signal Proc. and Comm.*, pp. 975-978, 2007.

[83] X. He and P. Shi, “Extraction of complex wavelet features for iris recognition,” *Int. Conf. on Pattern Recognition*, pp. 1 – 4, 2008.

[84] J. Daugman, “United Arab Emirates deployment of iris recognition, http://www.cl.cam.ac.uk/jgd1000/deployments.html, accessed Jan 2014.

[85] G. Rafiee, S. S. Dlay and W. L. Woo, “Region-of- interest extraction in low depth of field images using ensemble clustering and difference of Gaussian approaches,” *Pattern Recognition*, vol. 46, iss. 10, pp. 2685 – 2699, Oct., 2013.

[86] T. F. Chan, B. Y. Sandberg and L. A. Vese, “Active contour without edges for vector-valued images,” *Journal of Visual Comm. And Image Representation II*, pp. 130-141, 2000.

[87] T.F. Chan and L.A. Vese, "Active contours without edges," *IEEE Transactions on Image Processing*, vol.10, no.2, pp. 266-277, Feb. 2001.

[88] M. Kass, A. Witkin and D. Terzopoulos, “Snakes active contour models,” *International Journal of Computer Vision*, vol. 1, no. 4, pp. 321–331, 1987.

[89] S. Osher and N. Paragios, “Geometric level set methods in imaging, vision, and graphics*,” Springer-Verlag, New York*, 2003.

[90] A. Abhyankar and S. Schuckers, "Active shape models for effective iris segmentation," *Proc. in SPIE Conf. Biometric Tech. Human Identification III*, vol. 6202, Apr. 2006.

[91] C. Xu and J. Prince, “Gradient vector flow: a new external force for snakes*,” In The Proceedings of IEEE Conference on Computer Vision and Pattern Recognition*, pp. 66–71, 1997.

[92] C. Xu and J. Prince, “Snakes, shapes, and gradient vector flow,” *IEEE Transactions on Image Processing*, vol. 7, no. 3, pp. 359–369, 1998.

[93] O. Michailovich, Y. Rathi, and A. Tannenbaum, “Image segmentation using active contour driven by Bhattacharyya gradient flow,” *IEEE Trans. Image Processing*, vol. 16, no. 11, pp. 2787-2801, 2007.

[94] T. N. A. Nguyen, J. Cai, J. Zhang and J. Zheng, “Robust interactive image segmentation using convex active contours,” *IEEE Trans. Image Proc.,* vol. 21, no. 8, pp. 3734-3743, 2012.

[95] Y. Boykov and M. P. Jolly, “Interactive graph cuts for optimal boundary & region segmentation of objects in N-D images,” *Proceedings of International Conference on Computer Vision*, vol. 1, pp. 105-112, 2001.

[96] Y. Boykov and V. Kolmogorov, “Computing geodesics and minimal surfaces via graph cuts,” *in ICCV*, 2003.

[97] Y. Boykov and V. Kolmogorov, “An experimental comparison of mincut/max-flow algorithms for energy minimization in vision,” *IEEE Trans. on PAMI*, vol. 26, no. 9, pp. 1124-1137, 2004.

[98] V. Kolmogorov and R. Zabih, “What energy functions can be minimized via graph cuts?,” *IEEE Transactions on Pattern Analysis and Machine Intelligence*, vol. 26, no. 2, 2004.

[99] V. Kolmogorov and Y. Boykov, “What metrics can be approximated by geo-cuts, or global optimization of length/area and flux,” *in ICCV ’05*, 2005.

[100] Y. Boykov, V. Kolmogorov, D. Cremers, and A. Delong, “An integral solution to surface evolution PDEs via geo-cuts.,” *in ECCV (3)*, pp. 409–422, 2006.

[101] Y. Boykov and G. Funka-Lea, “Graph cuts and efficient N-D image segmentation,” *International Journal of Computer Vision*, vol.70, no.2, pp. 109-131, 2006.

[102] L. R. Ford, and D. R. Fulkerson, “Maximal flow through a network,” *Canadian Journal of Mathematics*, vol. 8, pp. 399-404, 1956.

[103] H. Proenca, S. Filipe, R. Santos, J. Oliveira and L. A. Alexandre, “The UBIRIS.v2: A database of visible wavelength iris images captured on-the-move

and at-a-distance," *IEEE Transactions on Pattern Analysis and Machine Intelligence*, vol. 32, pp. 1 – 7, 2010.

[104] CASIA Iris Image Database V4.0, http://www.cbsr.ia.ac.cn/iris-database.htm, accessed Oct. 2014.

[105] UBIRIR Iris Image Database V2.0, http://iris.di.ubi.pt/, accessed Oct. 2014.

[106] Iridian system. http://www.iridiantech.com/, accessed Nov. 2014.

[107] A. Criminisi, P. Perez, and K. Toyama, "Region filling and object removal by exemplar-based inpainting," *IEEE Tras. on Image Processing*, vol. 13, no. 9, Sept. 2004.

[108] M. Hasegawa, T. Kako, S. Hirobayashi, T. Misawa, T. Yoshizawa and Y. Inazumi, "Image inpainting on the basis of spectral structure from 2-D nonharmonic analysis," *IEEE Trans. on Image Processing*, vol. 22, no. 8, Aug. 2013.

[109] D. Li, D. Winfield, and D. J. Parkhurst, "Starburst: A hybrid algorithm for video-based eye tracking combining feature-based and model-based approaches," *IEEE Computer Society Conference on Computer Vision and Pattern Recognition (CVPRW'05) – Workshops, 2005.*

[110] S. G. Mallat, "A theory for multiresolution signal decomposition: the wavelet representation," *Pattern Analysis and Machine Intelligence, IEEE Transactions on,* vol. 11, pp. 674-693, 1989.

[111] I. Daubechies, "The wavelet transform, time-frequency localization and signal analysis", *Information Theory, IEEE Transaction on*, vol. 36, pp. 961-1005, 1990.

[112] I. Daubechies, "Ten lectures on wavelets," *Capital City Press*, 1992.1005, 1990.

[113] I. Daubechies, "Ten lectures on wavelets CBMS-NSF*," Regional Conference Series in Applied Mathematics, SIAM,* vol. 61, 1992.

[114] N. G. Kingsbury, "Complex wavelets for shift invariant analysis and filtering of signals," *Journal of Applied and Computational Harmonic Analysis*, vol. 10, no. 3, pp. 234-253, 2001.

[115] I. W. Selesnick, “Hilbert transform pairs of wavelet bases,” *IEEE Signal Processing Letters*, vol. 8, no. 6, pp. 170-173, June 2001.

[116] H. Wyatt, “A minimum wear-and-tear meshwork for the iris,” *Vision Research*, vol. 40, pp. 2167–2176, 2000.

[117] R. D. Nowak, and R. G. Baraniuk, “Adaptive weighted highpass filtering using multiscale analysis,” *IEEE Trans. Image Processing*, vol. 7, no. 7, pp. 1068-1074, July 1998.

[118] V. Vapnik, “Estimation of dependences based on empirical data [in Russian]. Nauka, Moscow, 1979. (English translation: Springer Verlag, New York, 1982), *Springer Verlag*, 1982.

[119] V. Vapnik. The Nature of Statistical Learning Theory. Springer-Verlag, New York, 1995.

[120] V. Vapnik. Statistical Learning Theory. John Wiley and Sons, Inc., New York, 1998.

[121] P. Yao, J. Li, X. Ye, Z Zhuang and B. Li, “Iris recognition algorithm using modified Log-Gabor filters,” Int. Conf. on Pattern Recognition (ICPR), vol. 4, pp. 461 – 464, 2006.

[122] D. V. De Ville and M. Unser, “Complex Wavelet Bases, Steerability, and the Marr-Like Pyramid”, IEEE Transactions on Image Processing, 17(11):2063–2080, 2008.